12-2016

Interplanetary mission design with applications to guidance and optimal control of aero-assisted trajectories

Peter J. Edelman
Purdue University

Recommended Citation

Edelman, Peter J., "Interplanetary mission design with applications to guidance and optimal control of aero-assisted trajectories" (2016). *Open Access Dissertations*. 982.
https://docs.lib.purdue.edu/open_access_dissertations/982

Graduate School Form
30 Updated 12/26/2015

PURDUE UNIVERSITY
GRADUATE SCHOOL
Thesis/Dissertation Acceptance

This is to certify that the thesis/dissertation prepared

By Peter J. Edelman

Entitled
INTERPLANETARY MISSION DESIGN WITH APPLICATIONS TO GUIDANCE AND OPTIMAL CONTROL OF AERO-ASSISTED TRAJECTORIES

For the degree of Doctor of Philosophy ▾

Is approved by the final examining committee:

James M. Longuski
Chair

Michael J. Grant

William A. Crossley

Kathleen C. Howell

To the best of my knowledge and as understood by the student in the Thesis/Dissertation Agreement, Publication Delay, and Certification Disclaimer (Graduate School Form 32), this thesis/dissertation adheres to the provisions of Purdue University's "Policy of Integrity in Research" and the use of copyright material.

Approved by Major Professor(s): James M. Longuski

Approved by: Weinong Wayne Chen 12/6/2016
Head of the Departmental Graduate Program Date

INTERPLANETARY MISSION DESIGN WITH APPLICATIONS TO GUIDANCE AND OPTIMAL CONTROL OF AERO-ASSISTED TRAJECTORIES

A Dissertation

Submitted to the Faculty

of

Purdue University

by

Peter J. Edelman

In Partial Fulfillment of the

Requirements for the Degree

of

Doctor of Philosophy

December 2016

Purdue University

West Lafayette, Indiana

A person who never made a mistake never tried anything new.

–Albert Einstein

Science is a way of thinking much more than it is a body of knowledge.

–Carl Sagan

Man strives to provide himself with food clothing and housing for the sake of the body. He must also provide himself with something to keep the mind healthy and happy. It is the mind that conditions even the body. The mind is the instrument, the flywheel, and the thickest comrade of man. Through it, one can ruin oneself or save oneself. Regulated and controlled, channeled properly it can liberate; wayward and let loose, it can entangle and bind fast.

–Sri Sathya Sai Baba

ACKNOWLEDGEMENTS

You do not truly realize how much you do not know until you go for a master or doctoral degree. That being said, this was not easy and would not have made it without the helpful instruction and guidance of many people. First, I thank my friend and advisor, Professor James Longuski for cultivating the potential I did not know I possessed in the field of astrodynamics, his helpful guidance in times of frustration, and entertaining discussions about Star Trek, movies, and The Simpsons. I am grateful to Professor Howell, who helped me understand problems in a more visual manner and whose education in nonlinear systems theory was instrumental to the success of my research. I am grateful to Professor Crossley for introducing me to the usefulness and practicality of direct optimization methods. I am also grateful to Professor Grant for his robust guidance in my guidance research.

Additionally, I would like to acknowledge Dave Skinner for repairing many issues that arose with software from past years. To my colleagues, past and present, you have made the research group feel like a second family, and I appreciate all the laughs and helpful suggestions to my research.

Finally, I would like to thank my parents and grandmother for their unrelenting love and support.

TABLE OF CONTENTS

LIST OF TABLES

LIST OF FIGURES

ABSTRACT

Edelman, Peter J. Ph.D., Purdue University, December 2016. Interplanetary Mission Design with Applications to Guidance and Optimal Control of Aero-Assisted Trajectories. Major Professor: James M. Longuski.

A method for finding optimal aerogravity-assist tours of the solar system is developed using indirect methods. Two cost functionals are used in the optimization; finding the minimum required maximum lift-to-drag ratio, with and without a convective heating-rate path constraint, and the path which provides the minimum total stagnation point convective heat load. It is found that using present or near-future thermal protection system materials will suffice for certain aerogravity-assist trajectories at Mars. Minimum heat load optimal trajectories are found for aerocapture maneuvers at Uranus and Neptune. With a large radius, and short rotational periods, atmospheric rotation must be taken into account to accurately model the system dynamics.

Investigation of the 2018 Inspiration Mars free-return opportunity is conducted. A broad search over 100 years of Mars free-return trajectories is catalogued, and a Pareto front analysis is employed to find the overall best trajectories in the timespan. The geometry is explored further with the use of a time-free ephemeris to see where minimal energy transfer arcs between Earth and Mars occur, and see if the 2018 opportunity is one such transfer. It turned out that both the 2017 and 2064 candidates found from the 100-year search were the closest to minimum energy, highlighting the rarity of the Inspiration Mars opportunity, and gives a motivating push to fly this mission.

CHAPTER 1. INTRODUCTION

Aero-assisted maneuvers come in four forms: aero-assisted orbital transfer (AOT), aerobraking, aerogravity assist (AGA), and aerocapture. The current work addresses the latter two. An aerogravity-assist maneuver is an augmented form of gravity-assist where a spacecraft uses generated lift to increase the amount of turning around a celestial body. More turning affects the heliocentric delta-V, leading to considerable propellant mass savings. A method for finding interplanetary tours with optimal aerogravity-assist trajectories is formulated. One type of optimal trajectory yields the lowest maximum lift-to-drag ratio (L/D) needed to complete the maneuver. Another optimal trajectory has constraints imposed on the maximum allowable stagnation point convective heating rate the spacecraft undergoes in the form of a state-variable inequality constraint. A third type of optimal trajectory finds the path that produces the minimum heat load the spacecraft accrues for the flythrough. All trajectory optimization is done using a classical indirect optimal control approach. Additionally a guidance scheme is developed to robustly guide the spacecraft during an aerogravity-assist maneuver, subject to dispersions in atmospheric density and initial conditions.

Aerocapture is a maneuver where a vehicle arriving at a celestial body at hyperbolic speeds enters the body's atmosphere and uses the aerodynamic drag to reduce its orbital energy. The vehicle remains in the atmosphere until it is captured in the body's gravity-well, where it exits the atmosphere with a desired orbit period. Recent interest at NASA’s JPL and AMES in the Ice Giants (Uranus and Neptune) has prompted studies regarding the usefulness of aerocapture to get into orbit. These large bodies rotate at high speeds requiring the rotating atmosphere to be modeled in the dynamics of the vehicle during the flythrough. Using optimal control theory, the minimum heat load aerocapture trajectory with rotating atmospheric effects is found.

Inspiration Mars was a human fly-by mission of Mars proposed to launch in early 2018, perform a free-return around Mars and arrive back at earth 500 days later. Research was conducted to see why the 2018 opportunity was so desirable, and to see if any back-up trajectories were available. Large sweeps of Earth-Mars-Earth free-return trajectories were catalogued using a patched-conic approach and evaluated in terms of Earth launch and Earth arrival energies. The Earth-Mars heliocentric geometry was analyzed using a time-free ephemeris model and the most desirable relative positions of the two planets were found. A back-up trajectory was found with a flyby of Venus having a launch date in 2021.

CHAPTER 2. OPTIMAL CONTROL METHODS AND NUMERICAL SOLVERS

Optimal control theory applied to trajectory optimization decomposes into two categories: direct and indirect optimization. Direct optimization has the trajectory states and control parameterized into distinct points (or nodes) and a desired cost functional is minimized (or maximized) using nonlinear programming (NLP) algorithms, gradient-based methods, or genetic algorithms. This method is often referred to as direct transcription [1]. The state equations are integrated either implicitly using a collocation scheme or a pseudo-spectral method, or explicitly using a shooting technique. The advantage of direct methods allows for easier implementation of constraints, particularly inequality constraints on the states, path, or control variables, and usually allows for a wider radius of convergence when poor initial estimates are used. The disadvantage of direct optimization is the often large computational effort required to solve a problem, particularly if it spans a large length of time. Indirect trajectory optimization is a functional optimization method that employs the calculus of variations to minimize (or maximize) the cost functional. Dynamic, path, state, control, and (sometimes) terminal constraints are adjoined to the cost functional using Lagrange multipliers, and necessary conditions are derived which guarantees a local extrema if they are satisfied. These necessary conditions convert the optimization problem into a boundary-value problem (BVP). A BVP can be solved by implicit integration using collocation or pseudo-spectral methods, or explicitly using shooting techniques. The advantage of indirect methods is low computational cost and robust setup, but the disadvantage is the often small radius of convergence, and lack of physical meaning of the costate variables. In the current work, only indirect optimization is used, however detailed descriptions of the theory and implementation of direct optimization to trajectories can be found in [2]. All techniques presented in this chapter are used in different sections of the current work.

2.1 Indirect Optimization

In many problems, the calculus of variations approach to optimal control problems provides a robust setup to the minimization of a certain cost functional. Where it becomes more difficult is when more than one inequality constraint on the states or controls is present, or when there is no idea of what initial guess to use, as the radius of convergence is often small. When there is more than one inequality constraint, the prediction of ‘switching times,’ or times when the solution will come into contact or leave the boundaries of the inequalities becomes increasingly difficult. The switching structure of getting on and off the boundaries must be assumed a-priori, thus when there are multiple inequality constraints with multiple boundary contacts, it can be numerically cumbersome, especially when the numerical solver has the switching times cross each other. A summary of the necessary conditions for a local extrema with state-variable inequality constraints (SVICs), and an unknown final time is presented in the current work. For detailed proofs, see [3–5]

2.1.1 Euler-Lagrange Theorem

The Problem of Bolza [3] is setup the following way:

$$Min\ J = g\left(t_f, \boldsymbol{x}_f\right) + \int_{t_0}^{t_f} L\left(t, \boldsymbol{x}, \boldsymbol{u}\right) dt \tag{2.1}$$

subject to:

$$\dot{\boldsymbol{x}} - \boldsymbol{f}\left(t, \boldsymbol{x}, \boldsymbol{u}\right) = \boldsymbol{0} \tag{2.2}$$

$$\boldsymbol{x}\left(t_0\right) = \boldsymbol{x}_0 \tag{2.3}$$

$$\boldsymbol{x}\left(t_f\right) = \boldsymbol{x}_f \tag{2.4}$$

$$\boldsymbol{\Psi}\left(t_0, \boldsymbol{x}_0, t_f, \boldsymbol{x}_f\right) = \boldsymbol{0} \tag{2.5}$$

$$\boldsymbol{S}\left(t, \boldsymbol{x}\right) \leq \boldsymbol{0} \tag{2.6}$$

where equation (2.1) contains the terminal cost *g*, and the path cost represented by the integral term. Equation (2.2) is an *n*-vector of process equations, equations (2.3) and (2.4) are the initial and final boundary conditions respectively, equation (2.5) is a *p*-vector of terminal constraints, and equation (2.6) represents an s-vector of SVICs.

First the SVICs are treated by looking at the time interval on [t_{enter}, t_{exit}] where the constraints are active (equal to zero, or on the boundary):

$$S_i\left[t, x\left(t\right)\right] = 0 \quad \forall \quad t \in \left[t_{enter}, t_{exit}\right] \subset \left[t_0, t_f\right] \qquad i = 1, \ldots, \mathrm{s} \tag{2.7}$$

For simplicity and without loss of generality let $i = s = 1$. Next, successive total time derivatives of the SVICs are taken until the first control variable appears. Mathematically this is represented as:

$$S\left(t, \boldsymbol{x}\right) = 0, \quad S^{(1)}\left(t, \boldsymbol{x}\right) = \frac{\partial S}{\partial \boldsymbol{x}} \frac{\partial \boldsymbol{x}}{\partial t} + \frac{\partial S}{\partial t} = 0, \ldots, S^{(q-1)}\left(t, \boldsymbol{x}\right) = 0 \tag{2.8}$$

$$S^{(q)}\left(t,\boldsymbol{x},\boldsymbol{u}\right)=0,\quad \frac{\partial\left[S^{(q)}\left(t,\boldsymbol{x},\boldsymbol{u}\right)\right]}{\partial\boldsymbol{u}}\neq 0 \tag{2.9}$$

where $S^{(j)}$ represents the j-th total time derivative, and q is the order of the SVIC. In many dynamical systems, the order is rarely greater than 2 [6]. It has been proven that if $q = 1$, only boundary arcs occur (no touch points), if $q = 2$, boundary arcs *and* touch points may occur, and if $q > 2$, then the SVIC only touches the border at single points t_{touch}, and does not remain active over an interval [7]. Figure 2.1 gives a graphical representation of a switching structure including a constrained subarc and a touch point on the boundary.

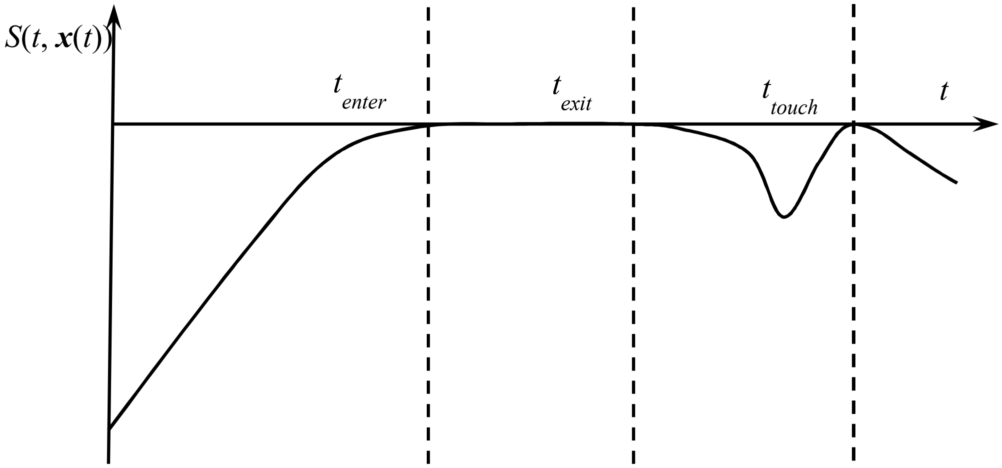

Figure 2.1 Illustration of a SVIC switching curve along a constrained subarc on [t_{entry}, t_{exit}], and at a touch point t_{touch}.

With the order of the SVIC found, equations (2.2), (2.5), and the first of (2.9) are adjoined to equation (2.1) with vectors of Lagrange multipliers with the same lengths to get a single scalar equation:

$$J=g\left(t_f,\boldsymbol{x}_f\right)+\int_{t_0}^{t_f}\left\{L\left(t,\boldsymbol{x},\boldsymbol{u}\right)+\boldsymbol{\lambda}^T\left[\dot{\boldsymbol{x}}-\boldsymbol{f}\left(t,\boldsymbol{x},\boldsymbol{u}\right)\right]+\boldsymbol{\mu}S^{(q)}\left(t,\boldsymbol{x},\boldsymbol{u}\right)\right\}dt+\boldsymbol{\nu}^T\Psi \tag{2.10}$$

where $\boldsymbol{\lambda}$ and $\boldsymbol{\mu}$ vary with time, and $\boldsymbol{\nu}$ is constant. Let the Hamiltonian, H, be defined as:

$$H\left(t,\boldsymbol{x},\boldsymbol{u},\lambda,\mu\right)=L\left(t,\boldsymbol{x},\boldsymbol{u}\right)+\lambda^{T}\boldsymbol{f}\left(t,\boldsymbol{x},\boldsymbol{u}\right)+\mu S^{(q)}\left(t,\boldsymbol{x},\boldsymbol{u}\right) \tag{2.11}$$

Then the cost functional can be written:

$$J=g\left(t_f,\boldsymbol{x}_f\right)+\int_{t_0}^{t_f}\left\{H\left(t,\boldsymbol{x},\boldsymbol{u},\lambda,\mu\right)-\boldsymbol{\lambda}^{T}\dot{\boldsymbol{x}}\right\}dt+\boldsymbol{\nu}^{T}\boldsymbol{\Psi} \tag{2.12}$$

By taking the variation of equation (2.12), it is shown that the necessary conditions for a local extrema with unknown final time are [3]:

$$\frac{\partial H}{\partial \boldsymbol{x}}+\dot{\boldsymbol{\lambda}}^{T}=\boldsymbol{0} \tag{2.13}$$

$$\frac{\partial H}{\partial \boldsymbol{u}}=\boldsymbol{0} \tag{2.14}$$

$$\boldsymbol{\lambda}_0^{T}+\boldsymbol{\nu}^{T}\frac{\partial \boldsymbol{\Psi}}{\partial \boldsymbol{x}_0}=\boldsymbol{0} \tag{2.15}$$

$$H_f+\frac{\partial g}{\partial t_f}+\boldsymbol{\nu}^{T}\frac{\partial \boldsymbol{\Psi}}{\partial t_f}=0 \tag{2.16}$$

$$-\boldsymbol{\lambda}_f^{T}+\frac{\partial g}{\partial \boldsymbol{x}_f}+\boldsymbol{\nu}^{T}\frac{\partial \boldsymbol{\Psi}}{\partial \boldsymbol{x}_f}=\boldsymbol{0} \tag{2.17}$$

$$\mu\begin{cases}=0, & \text{if } S<0\\ \geq 0, & \text{if } S=0\end{cases} \tag{2.18}$$

$$\Lambda\left(t_e,\boldsymbol{x}(t_e)\right)=\left\{S\left(t_e,\boldsymbol{x}(t_e)\right),\quad S^{(1)}\left(t_e,\boldsymbol{x}(t_e)\right),\quad \ldots,\quad S^{(q-1)}\left(t_e,\boldsymbol{x}(t_e)\right)\right\}^{T}=\boldsymbol{0} \tag{2.19}$$

$$\begin{gathered}\boldsymbol{\lambda}^{T}\left(t_e^{+}\right)-\boldsymbol{\lambda}^{T}\left(t_e^{-}\right)+\boldsymbol{\pi}^{T}\frac{\partial \Lambda}{\partial \boldsymbol{x}_e}=\boldsymbol{0}\\ H\left(t_e^{+}\right)-H\left(t_e^{-}\right)-\boldsymbol{\pi}^{T}\frac{\partial \Lambda}{\partial t_e}=0\end{gathered} \tag{2.20}$$

Equations (2.13) – (2.17) are the necessary conditions for local extrema, even if SVICs are not present. The extra boundary conditions on the costates and Hamiltonian essential for a well-posed BVP come from what is called the transversality conditions in equations (2.15), (2.16), and (2.17). Until a SVIC becomes active, the corresponding Lagrange multiplier μ is zero, and then becomes positive or equal to zero after activation, as shown in equation (2.18). Equations (2.19) and (2.20) are additional interior boundary conditions that must be satisfied, where t_e is one of the switching times, and can be specified at either t_{entry} or t_{exit} if along a constrained subarc, or t_{touch} at a touch point. An additional vector of Lagrange multipliers $\boldsymbol{\pi}^T$ (of length q) is required to satisfy the jump conditions in equation (2.20). The jump conditions necessitate that the costates associated with the SVIC may be discontinuous at t_e, but are continuous along the other endpoint of the constrained subarc [6]. For example, if t_e was chosen to be at t_{entry}, then the costates may be discontinuous at t_{entry}, but continuous at t_{exit}. The control law switches along the boundary subarc from equation (2.14) to satisfy:

$$S^{(q)}(t,\boldsymbol{x},\boldsymbol{u}) = 0 \tag{2.21}$$

and the associated Lagrange multiplier becomes:

$$\mu = -\left[S^{(q)}(t,\boldsymbol{x},\boldsymbol{u})\right]^{-1}\frac{\partial H}{\partial \boldsymbol{u}} \tag{2.22}$$

When state-variable inequality constraints are introduced to a problem using indirect methods the complexity of the necessary conditions greatly increases. For one SVIC, an additional $a \cdot q$ Lagrange multipliers, and $2 \cdot a$ boundary interaction times (corresponding to t_{entry}, t_{exit}, or t_{touch}) with an associated $a \cdot (q+2)$ interior boundary conditions are necessary, where a is the number of constrained subarcs. Once a second

SVIC is introduced, even more variables and boundary conditions are introduced with additional difficulty of predicting the switching structure between constrained subarcs among the two SVICs. Thus for optimal control problems involving more than one SVIC, the indirect method is usually not ideal, and direct methods become more robust in solving for feasible local extrema.

2.1.1.1 Adjoined versus Unadjoined Methods

Section 2.1.1 outlined the necessary conditions for local extrema of the cost function in equation (2.1) by adjoining the terminal constraint vector $\boldsymbol{\Psi}$ in equation (2.5) with a vector of Lagrange multipliers $\boldsymbol{\nu}^T$ to J. This method, referred to as the "adjoined method," has become the standard form of the necessary conditions from leading authors in the field of optimal control including Bryson and Ho [3]. A second way to treat the terminal constraints is to set the total differential of $\boldsymbol{\Psi}$ equal to zero:

$$d\boldsymbol{\Psi} = \mathbf{0} \tag{2.23}$$

and substitute the relationships between the individual differentials from $d\boldsymbol{\Psi}$ back into the transversality condition:

$$\left[H - \boldsymbol{\lambda}^T d\boldsymbol{x} \right] \Big|_{t_0}^{t_f} + dg = 0 \tag{2.24}$$

Derivations of this method are found in Citron [4] and Longuski et al. [5].

The main difference between the adjoined and unadjoined methods comes in the ease of implementation. Adjoining the terminal constraint vector to the cost functional will increase the dimensionality of the optimal control problem by p, where p is the length of $\boldsymbol{\Psi}$. Sometimes it's more advantageous to avoid the extra dimensions by using the unadjoined method, particularly if the terminal constraints are simple (e.g. involve only one or two state variables). However, when the terms become more complicated, it may be better to use the adjoined method to avoid large expressions in the transversality conditions. Large expressions can lead to numerical complications such as singularity, or near-singularity which can cause the numerical solver to become unstable.

2.2 Root-Solvers

One of the numerical cruxes the current research uses is root-solving techniques. Root-solvers attempt to find the arguments of an equation or systems of equations when they equal zero. They are useful in corrections for solving BVPs and finding unknown system parameters for linear and nonlinear static or dynamic systems. Root-solving is an iterative process, and a common problem with some linear and most nonlinear systems is that a poor initial estimate can end up in non-convergence of the algorithm. Depending on the algorithm, it may require one derivative of the system of equations, such as Newton's or Broyden's method (a quasi-Newtonian method), two or more derivatives, such as Halley's Method, or no derivatives, such as the secant method. One method may be better suited for a particular system than another, so there is no "best" algorithm. The two root-solvers used in this work are Newton's method and Broyden's method and are discussed below.

2.2.1 Newton's Method

Newton's method is based on a Taylor series expansion of a system of equations, and requires one derivative of the system to work. Consider an n-vector $\boldsymbol{X}$ of independent free variables:

$$\boldsymbol{X} = \left\{ X_1 \quad X_2 \quad \dots \quad X_n \right\}^T \tag{2.25}$$

Subject to a system of m equations that must satisfy:

$$\boldsymbol{F}(\boldsymbol{X})=\begin{Bmatrix} F_1(\boldsymbol{X}) \\ F_2(\boldsymbol{X}) \\ \vdots \\ F_m(\boldsymbol{X}) \end{Bmatrix}=\boldsymbol{0} \tag{2.26}$$

Taking a first-order Taylor series expansion about the solution $\boldsymbol{X}$ gives:

$$\boldsymbol{F}(\boldsymbol{X}+\Delta\boldsymbol{X})\approx\boldsymbol{F}(\boldsymbol{X})+\frac{d\boldsymbol{F}}{d\boldsymbol{X}}\cdot\Delta\boldsymbol{X}=\boldsymbol{0} \tag{2.27}$$

where $\Delta\boldsymbol{X}$ is a small perturbation from $\boldsymbol{X}$ and the m by n Jacobian matrix is defined by:

$$\frac{d\boldsymbol{F}}{d\boldsymbol{X}}=D\boldsymbol{F}(\boldsymbol{X})=\begin{bmatrix} \frac{dF_1}{dX_1} & \frac{dF_1}{dX_2} & \cdots & \frac{dF_1}{dX_n} \\ \frac{dF_2}{dX_1} & \frac{dF_2}{dX_2} & \cdots & \frac{dF_2}{dX_n} \\ \vdots & \vdots & \ddots & \vdots \\ \frac{dF_m}{dX_1} & \frac{dF_m}{dX_2} & \cdots & \frac{dF_m}{dX_n} \end{bmatrix} \tag{2.28}$$

Solving for $\Delta\boldsymbol{X}$, equation (2.27) predicts the required update to $\boldsymbol{X}$ to satisfy equation (2.26) in a linear sense. If there are any nonlinear terms involving $\boldsymbol{X}$ in $\boldsymbol{F}$, then the solution process will require iterations since the solver is linear. For the i-th iteration, a new update to $\boldsymbol{X}_i$ for iteration i+1 is given by:

$$\boldsymbol{X}_{i+1}=\boldsymbol{X}_i+\Delta\boldsymbol{X}_i \tag{2.29}$$

The process is repeated until a tolerance criteria on $\boldsymbol{F}$ is met. The tolerance criteria used in the current work is the l^2 norm of $\boldsymbol{F}$ is below a tolerance ε on the order of 10^{-12}. A tolerance this small can be used since all problems are scaled to be around a value of one.

If a solution to equation (2.26) exists, and provided a close enough initial estimate of $\boldsymbol{X}$, Newton's method will converge to a solution. However there are three cases of the system to consider. The first case is when $m = n$, and there are the same number of free variables as there are equations in the system. This is the most direct solution, as the update comes from the inversion of the square Jacobian Matrix:

$$\Delta \boldsymbol{X}_i = -k\left[D\boldsymbol{F}\left(\boldsymbol{X}_i\right)\right]^{-1} \boldsymbol{F}\left(\boldsymbol{X}_i\right) \tag{2.30}$$

where k is an attenuation parameter with admissive values in the set (0, 1]. For sensitive or highly nonlinear systems it is sometimes advantageous to scale the update in $\Delta \boldsymbol{X}_i$ to prevent instability in convergence, as the update is only a linearized correction. The update in equation (2.30) is unique and when $k = 1$, the solution converges quadratically for nonlinear systems.

The second case to consider is when $m < n$, and the number of free variables exceeds the number of equations in the system. If a solution exists, there are usually infinitely many combinations satisfying equation (2.26). A popular option to address this kind of system is to use the right Moore-Penrose pseudoinverse, also known as the least squares solution [8]. If $D\boldsymbol{F}(\boldsymbol{X}_i)$ has linearly independent rows, then the multiplication of $D\boldsymbol{F}(\boldsymbol{X}_i) \cdot D\boldsymbol{F}(\boldsymbol{X}_i)^T$ is square, and invertible. The right pseudoinverse update gives the "best fit" solution and is given by:

$$\Delta \boldsymbol{X}_i = -kD\boldsymbol{F}\left(\boldsymbol{X}_i\right)^T \left[D\boldsymbol{F}\left(\boldsymbol{X}_i\right) \cdot D\boldsymbol{F}\left(\boldsymbol{X}_i\right)^T\right]^{-1} \boldsymbol{F}\left(\boldsymbol{X}_i\right) \tag{2.31}$$

Given a sufficient initial estimate of $\boldsymbol{X}$, the update of equation (2.27) using equation (2.31) converges quadratically when $k = 1$.

The final case is when $m > n$, or the number of system equations exceeds the number of free variables. This is known as an overdetermined (or overconstrained) system, and has solutions only if the system of equations is not independent.

2.2.2 Broyden's Method

Another root-solver that employs knowledge of one derivative of the system is Broyden's method. This is a quasi-Newtonian method where instead of directly computing the Jacobian matrix in equation (2.28) at every iteration, an approximate value is used and is updated via an iterative process. The advantage of addressing the Jacobian in this way is that computational effort is decreased. If a Jacobian is non-sparse or has many nonzero entries, the computational cost of the Jacobian can be high. With Broyden's method, only one sample of the Jacobian is required, and it is updated with:

$$D\boldsymbol{F}\left(\boldsymbol{X}_i\right)=D\boldsymbol{F}\left(\boldsymbol{X}_{i-1}\right)+\frac{\boldsymbol{F}\left(\boldsymbol{X}_i\right)-\boldsymbol{F}\left(\boldsymbol{X}_{i-1}\right)-D\boldsymbol{F}\left(\boldsymbol{X}_{i-1}\right)\Delta\boldsymbol{X}_i}{\left\|\Delta\boldsymbol{X}_i\right\|^2}\cdot\Delta\boldsymbol{X}_i^T \tag{2.32}$$

With the Jacobian updated, either equation (2.30) or (2.31) is used to get the next update of $\boldsymbol{X}$.

2.3 Collocation

The two types of numerical integration methods are explicit and implicit integration. Explicit integration is a method where the numerical approximation of the state of a system of differential equations at a later time depends only on the knowledge of the state at the current and/or previous times. If x_i is the state at the current time t_i, then at later time $t_i + \Delta t_i = t_i + h_i$, the next state x_{i+1} can be mathematically represented by:

$$x_{i+1}=F\left(t_i,h_i,x_i,f\left(t_i,x_i\right)\right) \tag{2.33}$$

where f are the derivatives of the state variables and F is a numerical integrator function such as the Euler method, the Runge-Kutta method or the Prince-Dormand method. Depending on what system is being integrated, one numerical integration method may be better suited than another. Each method has its own respective local truncation errors, total accumulated errors, and integration stabilities associated with them.

Implicit integration methods require knowledge of the state at the current time in order to compute the state *at the current time*. A mathematical representation of this is:

$$x_{i+1} = F\left(t_i, h_i, x_i, x_{i+1}, f\left(t_i, x_i\right), f\left(t_{i+1}, x_{i+1}\right)\right) \tag{2.34}$$

where x_{i+1} appears on both sides of the equation. Unless x_{i+1} can be isolated to one side, the solution to equation (2.34) generally requires at least a root-solving technique where the equations

$$F\left(t_i, h_i, x_i, x_{i+1}, f\left(t_i, x_i\right), f\left(t_{i+1}, x_{i+1}\right)\right) - x_{i+1} = 0, \qquad i = 1, \ldots, N \tag{2.35}$$

are solved simultaneously. In equation (2.35), N is the discrete number of points (often called nodes) in the integration scheme, thus there are $n \cdot (N - 1)$ equations (usually nonlinear) to solve simultaneously, where n is the number of states.

Collocation is an implicit integration technique where the independent variable is discretized into nodes (also called collocation points) and the state equations (and control variables, if a direct optimization method is employed) are approximated by candidate functions, usually polynomials at the collocation points. In the current work, a Runge-Kutta method based on Lobatto quadrature formulas is used, namely the Lobatto IIIA family [9].

2.3.1 Mesh Construction

Collocation distributes errors and sensitivities over all the nodes. In the current work, both 3rd and 7th order polynomials are used in a collocation scheme. In this way, the differential equations are transcribed into a finite set of equality constraints of the form of equation (2.35), and solved using a root-solving technique.

The piece-wise polynomial representation can be constructed by first defining a mesh of N discrete time points, creating $N - 1$ discrete segments between each point:

$$t_1 < t_2 < \cdots < t_N \tag{2.36}$$

with a step-size $h_i = t_{i+1} - t_i$ that should be chosen small enough to satisfy an error tolerance for numerical integration. The smaller the step-size, the more accurate the solution, however the dimensionality of the problem increases by n for each additional segment. Next the time segments are normalized typically to be between [-1, 1] or [0, 1]. The collocation scheme presented here is a Lobatto method [9] and uses a normalization of [0, 1]. Thus the time segments are normalized via:

$$\tau = \frac{t - t_i}{h_i}, \qquad t \in [t_i, t_{i+1}] \tag{2.37}$$

The state in the ith segment is approximated by a pth degree Hermite interpolating polynomial of the form:

$$\boldsymbol{x}(\tau) = \boldsymbol{a}_0 + \boldsymbol{a}_1\tau + \boldsymbol{a}_2\tau^2 + \cdots + \boldsymbol{a}_p\tau^p, \qquad \tau \in [0, 1] \tag{2.38}$$

where the coefficients $\boldsymbol{a}_0$, …, $\boldsymbol{a}_p$ of each polynomial (one polynomial for each segment) are determined by using the values of the states and the dynamical system vector field $\dot{\boldsymbol{x}} = \boldsymbol{f}(t, \boldsymbol{x}, \boldsymbol{u})$ at distinct points along $\tau \in [0, 1]$. Choosing the location of the points in [0, 1] is nontrivial and the number of points (called nodes) depends upon the degree of the polynomial.

One selection process for the location of the nodes is to use the roots of a shifted Legendre polynomial taking on the form:

$$\frac{d^{p-2}}{dt^{p-2}}\left[t^{p-1}\left(1-t\right)^{p-1}\right]=0 \tag{2.39}$$

The node coefficients that come out of equation (2.39) are monotonically increasing such that $c_1 = 0 < c_2 < \ldots < c_p = 1$. The shifted Legendre polynomial roots are symmetric, so their nodes satisfy:

$$c_{p+1-j} = 1 - c_j \qquad j = 1, \ldots, p \tag{2.40}$$

Node locations of polynomials of orders 2 through 5 are given in Table 2.1.

The node locations at the endpoints of the segment, denoted $\boldsymbol{x}_i$ and $\boldsymbol{x}_{i+1}$ are the solution to the quadrature of the implicit integration method. States at the points in between, denoted $\boldsymbol{x}_2, \ldots, \boldsymbol{x}_{p\text{-}1}$ (i.e. $\boldsymbol{x}_1 = \boldsymbol{x}_i$ and $\boldsymbol{x}_p = \boldsymbol{x}_{i+1}$) are subdivided into two categories called variable nodes and defect points. The variable nodes and defect points represent the polynomial approximation of the state in $\tau = \left(0, 1\right)$. An important distinction is that while the variable nodes and endpoints of the segment are free variables and serve the same purpose in the implicit integration scheme, the endpoints are the actual quadrature solutions to the differential equations while the variable nodes are only an

Table 2.1 Location of nodes along each segment for various orders of polynomials

Polynomial Order	Location				
2	0				1
3	0		½		1
4	0	$\frac{1}{2}-\frac{\sqrt{5}}{10}$		$\frac{1}{2}+\frac{\sqrt{5}}{10}$	1
5	0	$\frac{1}{2}-\frac{\sqrt{21}}{14}$	½	$\frac{1}{2}+\frac{\sqrt{21}}{14}$	1

approximation. However for convenience in how the collocation scheme is set up, the endpoints will also be called variable nodes, as they all are design variables in the method. The defect points are then transcribed into equality constraints in terms of the coefficients in equation (2.38), the dynamics in $\boldsymbol{f}\left(t, \boldsymbol{x}, \boldsymbol{u}\right)$, and the free variables of the variable nodes.

It turns out that odd ordered polynomials produce the same number of defect points as the preceding even ordered ones, leading to greater accuracy for the same computational cost [10]. Thus the construction of polynomial coefficients in equation (2.38) will be outlined for odd-ordered polynomials. This means that in each segment there are $(p + 1)/2$ variable nodes and $(p - 1)/2$ defect points, and the variable nodes and defect points are placed at odd and even j respectively for $j = 1, \ldots, p$. The defect points are transcribed into equality constraints that match the dynamics of the vector field via:

$$\Delta_{i,jM} = \dot{\boldsymbol{x}}_{jM} - h_i \boldsymbol{f}\left(\tau_{jM}, \boldsymbol{x}_{jM}, \boldsymbol{u}_{jM}\right) = \boldsymbol{0} \qquad j = 2, 4, \ldots, p-1 \tag{2.41}$$

where a subscript M has been placed next to j to enforce that the defect points are in

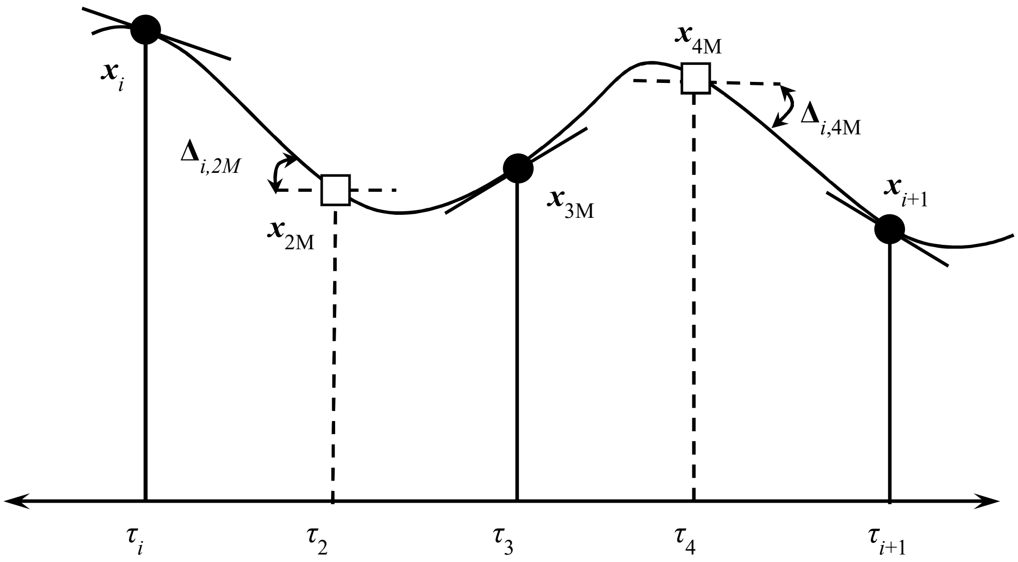

Figure 2.2 Collocation scheme using a fifth degree polynomial.

between the endpoints at i and i+1 (a mnemonic "*M*" for, "*in the Middle of…*"). An example diagram for a fifth order collocation polynomial with variable nodes and defect points is illustrated in Figure 2.2. The process for constructing the states at the defect points as well as the corresponding defect constraint is now outlined.

2.3.2 Higher Odd Order Polynomial Collocation

For arbitrary high orders of odd value p, the polynomial and its first derivative with respect to normalized time in equation (2.38) can be represented in matrix form as:

$$\begin{bmatrix} 1 & \tau_1 & \tau_1^2 & \cdots & \tau_1^{p-1} & \tau_1^p \\ 1 & \tau_{3M} & \tau_{3M}^2 & \cdots & \tau_{3M}^{p-1} & \tau_{3M}^p \\ \vdots & \vdots & \vdots & \ddots & \vdots & \vdots \\ 1 & \tau_p & \tau_p^2 & \cdots & \tau_p^{p-1} & \tau_p^p \\ 0 & 1 & 2\tau_1 & \cdots & (p-1)\tau_1^{p-2} & p\tau_1^{p-1} \\ \vdots & \vdots & \vdots & \ddots & \vdots & \vdots \\ 0 & 1 & 2\tau_p & \cdots & (p-1)\tau_p^{p-2} & p\tau_p^{p-1} \end{bmatrix} \begin{bmatrix} a_0 \\ a_1 \\ \vdots \\ a_p \end{bmatrix} = \begin{bmatrix} \boldsymbol{x}_i \\ \boldsymbol{x}_{3M} \\ \vdots \\ \boldsymbol{x}_{i+1} \\ h_i f_i \\ \vdots \\ h_i f_{i+1} \end{bmatrix} \tag{2.42}$$

or similarly, $\mathbf{Ta} = \mathbf{b}$. All the times and states τ_j and $\boldsymbol{x}_j$ are odd and represent the variable nodes. Solving for the polynomial coefficients in equation (2.42) we get $\mathbf{a} = \mathbf{T}^{-1}\mathbf{b}$. The values of the states at the defect points are found via:

$$\begin{bmatrix} \boldsymbol{x}_{2M} \\ \boldsymbol{x}_{4M} \\ \vdots \\ \boldsymbol{x}_{(p-1)M} \end{bmatrix} = \begin{bmatrix} 1 & \tau_{2M} & \tau_{2M}^2 & \cdots & \tau_{2M}^p \\ 1 & \tau_{4M} & \tau_{4M}^2 & \cdots & \tau_{4M}^p \\ \vdots & \vdots & \vdots & \ddots & \vdots \\ 1 & \tau_{(p-1)M} & \tau_{(p-1)M}^2 & \cdots & \tau_{(p-1)M}^p \end{bmatrix} \mathbf{T}^{-1}\mathbf{b} = \Upsilon \mathbf{b} \tag{2.43}$$

The defect constraints in equation (2.41) are constructed by taking the normalized time-derivative of equation (2.43) to yield:

$$\begin{bmatrix} \dot{\boldsymbol{x}}_{2M} \\ \dot{\boldsymbol{x}}_{4M} \\ \vdots \\ \dot{\boldsymbol{x}}_{(p-1)M} \end{bmatrix} = \begin{bmatrix} 0 & 1 & 2\tau_{2M} & \cdots & p\tau_{2M}^{p-1} \\ 0 & 1 & 2\tau_{4M} & \cdots & p\tau_{4M}^{p-1} \\ \vdots & \vdots & \vdots & \ddots & \vdots \\ 0 & 1 & 2\tau_{(p-1)M} & \cdots & p\tau_{(p-1)M}^{p-1} \end{bmatrix} \mathbf{T}^{-1}\mathbf{b} = \frac{d\Upsilon}{d\tau}\mathbf{b} \tag{2.44}$$

With the interpolated states and derivatives at the defect points found, equations (2.41) and (2.44) are related via:

$$\Delta_{i,jM} = \frac{d\Upsilon}{d\tau}\mathbf{b}_i - h_i \boldsymbol{f}\left(\tau_{jM}, \boldsymbol{x}_{jM}, \boldsymbol{u}_{jM}\right) = \mathbf{0} \qquad j = 2, 4, \ldots, p-1 \tag{2.45}$$

for every segment $i = 1, \ldots, N-1$. The collocation defects are solved using a root-solving method simultaneously and the integrated solution is represented by the endpoints of each segment, $\boldsymbol{x}_i$ for $i = 1, \ldots, N$.

2.3.3 Collocation Applied to Solving Optimal Control Problems

Applying the collocation method described above to problems in optimal control can be used for both direct and indirect methods. In direct methods, the defect constraints in equation (2.45) are applied as equality constraints for a nonlinear programming (NLP) package to solve. Collocation can easily adapt to add multiple path and control inequality constraints by specifying the bounding values at each variable node in the NLP scheme. Since a control law is not specified in a direct optimization approach, the control variables at the endpoints of each segment are included as design variables. The control values at each of the variable nodes and defect points between the endpoints are usually handled via linear interpolation.

With indirect methods, the optimization problem is transformed into a BVP with the collocation defects included in the constraint vector in equation (2.26) along with the initial conditions, final boundary conditions, terminal constraints and transversality conditions of equations (2.3), (2.4), (2.5), and (2.24) respectively. The Jacobian matrix has a regular structure so it is straightforward to implement in a numerical algorithm. An example Jacobian structure for a 3rd order polynomial is:

$$DF\left(\boldsymbol{X}\right)=\begin{bmatrix} \dfrac{\partial \boldsymbol{\Delta}_{1,2M}}{\partial \boldsymbol{x}_1} & \dfrac{\partial \boldsymbol{\Delta}_{1,2M}}{\partial \boldsymbol{x}_2} & 0 & 0 & \cdots & 0 & \dfrac{\partial \boldsymbol{\Delta}_{1,2M}}{\partial t_f} \\ 0 & \dfrac{\partial \boldsymbol{\Delta}_{2,2M}}{\partial \boldsymbol{x}_2} & \dfrac{\partial \boldsymbol{\Delta}_{2,2M}}{\partial \boldsymbol{x}_3} & 0 & \cdots & 0 & \dfrac{\partial \boldsymbol{\Delta}_{2,2M}}{\partial t_f} \\ 0 & 0 & \dfrac{\partial \boldsymbol{\Delta}_{3,2M}}{\partial \boldsymbol{x}_3} & \ddots & 0 & 0 & \vdots \\ \vdots & \vdots & \vdots & 0 & \dfrac{\partial \boldsymbol{\Delta}_{N-2,2M}}{\partial \boldsymbol{x}_{N-1}} & 0 & \dfrac{\partial \boldsymbol{\Delta}_{N-2,2M}}{\partial t_f} \\ 0 & 0 & \cdots & 0 & \dfrac{\partial \boldsymbol{\Delta}_{N-1,2M}}{\partial \boldsymbol{x}_{N-1}} & \dfrac{\partial \boldsymbol{\Delta}_{N-1,2M}}{\partial \boldsymbol{x}_N} & \dfrac{\partial \boldsymbol{\Delta}_{N-1,2M}}{\partial t_f} \\ \dfrac{\partial \boldsymbol{BC}_0}{\partial \boldsymbol{x}_1} & 0 & \cdots & 0 & 0 & 0 & \dfrac{\partial \boldsymbol{BC}_0}{\partial t_f} \\ 0 & 0 & \cdots & 0 & 0 & \dfrac{\partial \boldsymbol{BC}_f}{\partial \boldsymbol{x}_N} & \dfrac{\partial \boldsymbol{BC}_f}{\partial t_f} \end{bmatrix} \tag{2.46}$$

For a third order polynomial, there are two variable nodes and one defect point between each node, thus for each defect constraint $\boldsymbol{\Delta}_{i,j}$, the subscript j equals 2 for $i = 1, \ldots, N - 1$. The terms $\boldsymbol{BC}_0$, $\boldsymbol{BC}_f$, and t_f correspond to the initial and final boundary conditions vectors, and unknown final time. If there are state-variable inequality constraints, then there will be the tangency and jump conditions from equations (2.19) and (2.20) included in the Jacobian. With the indirect method, a well-defined BVP will produce the same number of design variables as constraints, so from an initial estimate of the design variables, the update for all associated BVPs uses equation (2.30).

The derivatives of the defect constraints are straightforwardly computed analytically allowing for faster computational time in evaluating the Jacobian. The analytical derivative for the defects can be expressed as:

$$\begin{aligned} &\frac{\partial \Delta_{i,jM}}{\partial \boldsymbol{x}_k} = \frac{d\Upsilon}{d\tau}\frac{\partial \mathbf{b}_i}{\partial \boldsymbol{x}_k} - h_i \frac{\partial \boldsymbol{f}\left(\tau_{jM}, \boldsymbol{x}_{jM}\right)}{\partial \boldsymbol{x}_{jM}} \Upsilon \frac{\partial \mathbf{b}_i}{\partial \boldsymbol{x}_k} \qquad j = 2,4,\ldots,p-1, \\ &k = i,(j+1)M,\ldots,(p-2)M, i+1 \qquad i = 1,\ldots,N \end{aligned} \tag{2.47}$$

An example evaluation of equation (2.47) for a fifth-order polynomial (p = 5, j = 2, 4, k = 1, 3M, 2) for i = 1 is:

$$\begin{aligned}
\frac{\partial \Delta_{1,2M}}{\partial \boldsymbol{x}_1} &= \tfrac{-90-16\sqrt{21}}{49}\mathbf{I} + \tfrac{-9-\sqrt{21}}{98}\frac{\partial \boldsymbol{f}}{\partial \boldsymbol{x}_1} - h_1 \frac{\partial \boldsymbol{f}}{\partial \boldsymbol{x}_{2M}}\left(\tfrac{231+39\sqrt{21}}{686}\mathbf{I} + \tfrac{21+3\sqrt{21}}{686} h_1 \frac{\partial \boldsymbol{f}}{\partial \boldsymbol{x}_1}\right) \\
\frac{\partial \Delta_{1,2M}}{\partial \boldsymbol{x}_{3M}} &= \tfrac{32}{7}\sqrt{\tfrac{7}{3}}\mathbf{I} - \tfrac{32}{49}\frac{\partial \boldsymbol{f}}{\partial \boldsymbol{x}_{3M}} - h_1 \frac{\partial \boldsymbol{f}}{\partial \boldsymbol{x}_{2M}}\left(\tfrac{16}{49}\mathbf{I} - \tfrac{8}{49}\sqrt{\tfrac{7}{3}} h_1 \frac{\partial \boldsymbol{f}}{\partial \boldsymbol{x}_{3M}}\right) \\
\frac{\partial \Delta_{1,2M}}{\partial \boldsymbol{x}_2} &= \tfrac{90-16\sqrt{21}}{49}\mathbf{I} + \tfrac{\sqrt{21}-9}{98} h_1 \frac{\partial \boldsymbol{f}}{\partial \boldsymbol{x}_2} - h_1 \frac{\partial \boldsymbol{f}}{\partial \boldsymbol{x}_{2M}}\left(\tfrac{231-39\sqrt{21}}{686}\mathbf{I} + \tfrac{-21+3\sqrt{21}}{686} h_1 \frac{\partial \boldsymbol{f}}{\partial \boldsymbol{x}_2}\right) \\
\frac{\partial \Delta_{1,4M}}{\partial \boldsymbol{x}_1} &= \tfrac{-90+16\sqrt{21}}{49}\mathbf{I} + \tfrac{-9+\sqrt{21}}{98}\frac{\partial \boldsymbol{f}}{\partial \boldsymbol{x}_1} - h_1 \frac{\partial \boldsymbol{f}}{\partial \boldsymbol{x}_{4M}}\left(\tfrac{231-39\sqrt{21}}{686}\mathbf{I} + \tfrac{21-3\sqrt{21}}{686} h_1 \frac{\partial \boldsymbol{f}}{\partial \boldsymbol{x}_1}\right) \\
\frac{\partial \Delta_{1,4M}}{\partial \boldsymbol{x}_{3M}} &= -\tfrac{32}{7}\sqrt{\tfrac{7}{3}}\mathbf{I} - \tfrac{32}{49}\frac{\partial \boldsymbol{f}}{\partial \boldsymbol{x}_{3M}} - h_1 \frac{\partial \boldsymbol{f}}{\partial \boldsymbol{x}_{4M}}\left(\tfrac{16}{49}\mathbf{I} + \tfrac{8}{49}\sqrt{\tfrac{7}{3}} h_1 \frac{\partial \boldsymbol{f}}{\partial \boldsymbol{x}_{3M}}\right) \\
\frac{\partial \Delta_{1,4M}}{\partial \boldsymbol{x}_2} &= \tfrac{90-16\sqrt{21}}{49}\mathbf{I} + \tfrac{\sqrt{21}-9}{98} h_1 \frac{\partial \boldsymbol{f}}{\partial \boldsymbol{x}_2} - h_1 \frac{\partial \boldsymbol{f}}{\partial \boldsymbol{x}_{4M}}\left(\tfrac{231+39\sqrt{21}}{686}\mathbf{I} + \tfrac{-21-3\sqrt{21}}{686} h_1 \frac{\partial \boldsymbol{f}}{\partial \boldsymbol{x}_2}\right)
\end{aligned} \tag{2.48}$$

where **I** is the identity matrix of size n by n (recall n is the number of states in $\boldsymbol{f}$). Although the analytical derivatives look tedious to evaluate, the number coefficients in equation (2.48) are computed a-priori and stored, meaning a programming or scripting language that allows easy manipulations of matrices can quickly implement the analytical derivatives in an algorithmic fashion.

2.3.4 Mesh Refinement

In order to make the integration error smaller, often a mesh refinement strategy is employed, especially if the integration time is large. A constant step size $h_i = h$ is often not the best choice when integrating over large intervals, so the mesh in equation (2.36) is changed. For the problems in the current work, the integration times are no longer than 10 minutes, so mesh refinement is deemed unnecessary as long as a sufficient number of endpoint nodes are specified in the initial mesh. However for detailed description of mesh refinement strategies, see [11] for one that refines the mesh internally while solving the collocation equations, and [12] for ones that refine the mesh after the collocation equations are solved, to approximately distribute the error equally along each segment.

2.4 Shooting Methods

Another method to solve optimal control problems is a shooting method. A shooting method uses explicit integration techniques to propagate forward (or backward) from a set of initial conditions and corrects the initial conditions based on how far off the final integrated values are from the desired boundary conditions. There are various ways to address the corrections process, but the one described here is based off derivatives of the vector field in equation (2.2) with respect to the initial conditions.

Consider a nonlinear system of the form:

$$\dot{\boldsymbol{x}} = \boldsymbol{f}\left[t, \boldsymbol{x}\left(t, \boldsymbol{x}_0, \boldsymbol{p}\right), \boldsymbol{p}\right] \qquad \boldsymbol{x}\left(t_0\right) = \boldsymbol{x}_0 \tag{2.49}$$

where $\boldsymbol{p}$ is a vector of parameters that may need to be solved and $\boldsymbol{x}_0$ is the vector of initial conditions. The elements in vector $\boldsymbol{p}$ could be parameterized controls in a direct shooting method, unknown points in time where certain events occur such as touch points on boundary subarcs, unknown final integration times, or unknown constants in the differential equations. From the fundamental theorem of calculus, the solution to equation (2.49) is given by:

$$\boldsymbol{x}(t)=\boldsymbol{x}(t_0)+\int_{t_0}^{t}\boldsymbol{f}\left[t,\boldsymbol{x}(t,\boldsymbol{x}_0,\boldsymbol{p}),\boldsymbol{p}\right]dt \tag{2.50}$$

Taking a derivative of equation (2.50) with respect to the initial conditions using Leibniz's rule yields:

$$\frac{\partial\boldsymbol{x}}{\partial\boldsymbol{x}_0}=\mathbf{I}+\int_{t_0}^{t}\frac{\partial\boldsymbol{f}}{\partial\boldsymbol{x}}\frac{\partial\boldsymbol{x}}{\partial\boldsymbol{x}_0}dt \tag{2.51}$$

Taking a derivative of equation (2.51) with respect to time yields a new set of differential equations:

$$\frac{d}{dt}\left(\frac{\partial\boldsymbol{x}}{\partial\boldsymbol{x}_0}\right)=\frac{\partial\boldsymbol{f}}{\partial\boldsymbol{x}}\frac{\partial\boldsymbol{x}}{\partial\boldsymbol{x}_0} \tag{2.52}$$

or,

$$\dot{\mathbf{\Phi}}=\frac{\partial\boldsymbol{f}}{\partial\boldsymbol{x}}\mathbf{\Phi} \tag{2.53}$$

where $\mathbf{\Phi}$ is known as the state-transition matrix, which relates how variations in $\boldsymbol{x}$ at time t is related to variations in the initial conditions $\boldsymbol{x}_0$ to first order. The initial condition for the state transition matrix is:

$$\frac{\partial\boldsymbol{x}(t_0)}{\partial\boldsymbol{x}_0}=\mathbf{I} \tag{2.54}$$

as all the initial conditions are independent of each other. To get relationships of the variations in in $\boldsymbol{x}$ at time t to variations of the parameters in $\boldsymbol{p}$, take a derivative of equation (2.50) with respect to $\boldsymbol{p}$:

$$\frac{\partial \boldsymbol{x}}{\partial \boldsymbol{p}} = \int_{t_0}^{t} \left(\frac{\partial \boldsymbol{f}}{\partial \boldsymbol{x}} \frac{\partial \boldsymbol{x}}{\partial \boldsymbol{p}} + \frac{\partial \boldsymbol{f}}{\partial \boldsymbol{p}} \right) dt \tag{2.55}$$

then a derivative with respect to time of the resulting equation gives:

$$\frac{d}{dt}\left(\frac{\partial \boldsymbol{x}}{\partial \boldsymbol{p}} \right) = \frac{\partial \boldsymbol{f}}{\partial \boldsymbol{x}} \frac{\partial \boldsymbol{x}}{\partial \boldsymbol{p}} + \frac{\partial \boldsymbol{f}}{\partial \boldsymbol{p}} \tag{2.56}$$

or,

$$\dot{\boldsymbol{\Theta}} = \frac{\partial \boldsymbol{f}}{\partial \boldsymbol{x}} \boldsymbol{\Theta} + \frac{\partial \boldsymbol{f}}{\partial \boldsymbol{p}} \tag{2.57}$$

In equation (2.57), $\boldsymbol{\Theta}$ gives the relationship of the variations in $\boldsymbol{x}$ at time t to variations of the parameters in $\boldsymbol{p}$ to first-order. The initial condition for $\boldsymbol{\Theta}$ is:

$$\frac{\partial \boldsymbol{x}(t_0)}{\partial \boldsymbol{p}} = \boldsymbol{0} \tag{2.58}$$

as the parameters are independent from the initial conditions.

Upon numerical integration of equations (2.53) and (2.57), the state-transition matrix and $\boldsymbol{\Theta}$ can be implemented in a Jacobian for a root-solving process. If the solver converges, the solution is a proper set of initial conditions that satisfy all boundary conditions. However, for a system of n states and par parameters, the number of differential equations requiring numerical integration increases by $n^2 + n \cdot par$, meaning more computational effort. Higher order Taylor-series expansions of equation (2.51) are sometimes employed to get better relationships in the variations, but this increases the dimensionality of the problem even further.

2.4.1 Single Shooting

Using the state-transition matrix in a root-solving process subdivides into two categories: single and multiple shooting. Single shooting propagates the differential equations forwards over the entire interval $t \in \left[t_0, t_f \right]$ and then a corrections process is performed via a root-solver. Using the state-transition matrix, the single shooter can be highly sensitive to variations in the initial conditions for nonlinear systems, as the solution to equation (2.53) is only a linear estimate. A way to overcome the sensitivity of single shooting is to break up the integration over many segments and distribute the sensitivity over the integration interval. This results in a larger number of free variables and constraints, but gives a larger radius of convergence.

2.4.2 Multiple Shooting

Multiple shooting is a more robust method of obtaining convergence and exploring the phase-space of a system, especially near sources of high nonlinearity where the corrections process becomes sensitive. First the integration interval is divided into N nodes with $N - 1$ segments between the nodes. Each segment has their own set of initial conditions $\boldsymbol{x}_i$ and are propagated forward in time from t_i to t_{i+1}. Thus the initial estimate of each set of initial conditions must be given to the root-solver for corrections. An illustration of the multiple shooting method is in Figure 2.3.

After propagation of each segment, the ith initial conditions vector in general does not match the propagated state of from segment $i - 1$, or $\boldsymbol{x}_{i-1}^{f} \neq \boldsymbol{x}_i$, for $i = 2, \ldots, N$. This means that integrated states and initial conditions of the next segment must be enforced to be equal through equality constraints, which are often called continuity conditions. The free variables in equation (2.25) include every initial conditions vector, the final values at $t = t_f$, and any parameters:

$$\boldsymbol{X} = \left[\boldsymbol{x}_1 \quad \boldsymbol{x}_2 \quad \cdots \quad \boldsymbol{x}_N \quad \boldsymbol{p} \right]^T \tag{2.59}$$

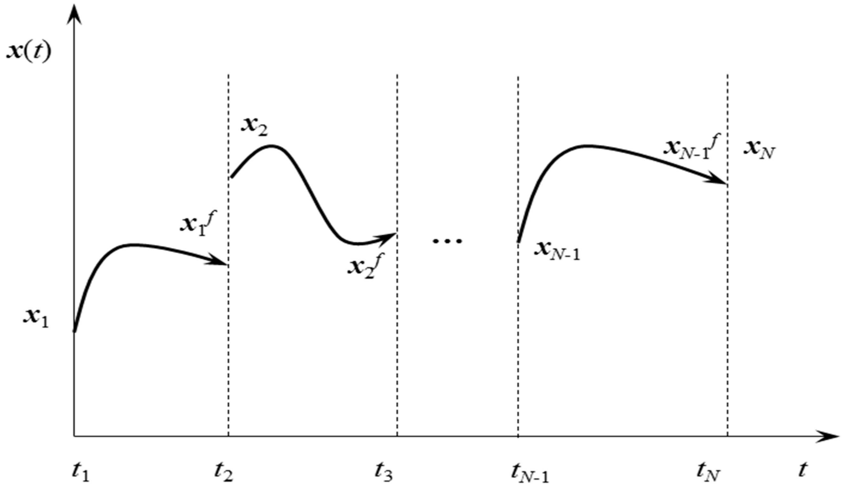

Figure 2.3 Visualization of multiple shooting before corrections.

The constraints include the continuity conditions, and initial and final boundary conditions:

$$\boldsymbol{F}(\boldsymbol{X}) = \begin{bmatrix} \boldsymbol{x}_1^f - \boldsymbol{x}_2 \\ \boldsymbol{x}_2^f - \boldsymbol{x}_3 \\ \vdots \\ \boldsymbol{x}_{N-1}^f - \boldsymbol{x}_N \\ \boldsymbol{BC}_0 \\ \boldsymbol{BC}_f \end{bmatrix} \tag{2.60}$$

The Jacobian matrix is readily computed as:

$$\boldsymbol{F}(\boldsymbol{X}) = \begin{bmatrix} \frac{d\boldsymbol{x}_1^f}{d\boldsymbol{x}_1} & -\mathbf{I} & 0 & \cdots & 0 & 0 & \frac{d\boldsymbol{x}_1^f}{d\boldsymbol{p}} \\ 0 & \frac{d\boldsymbol{x}_2^f}{d\boldsymbol{x}_2} & -\mathbf{I} & \cdots & 0 & 0 & \frac{d\boldsymbol{x}_2^f}{d\boldsymbol{p}} \\ \vdots & \vdots & \vdots & \ddots & \vdots & 0 & \vdots \\ 0 & 0 & 0 & \cdots & \frac{d\boldsymbol{x}_{N-1}^f}{d\boldsymbol{x}_{N-1}} & -\mathbf{I} & \frac{d\boldsymbol{x}_{N-1}^f}{d\boldsymbol{p}} \\ \frac{d\boldsymbol{BC}_0}{d\boldsymbol{x}_1} & 0 & 0 & \cdots & 0 & 0 & \frac{d\boldsymbol{BC}_0}{d\boldsymbol{p}} \\ 0 & 0 & 0 & \cdots & 0 & \frac{d\boldsymbol{BC}_f}{d\boldsymbol{x}_N} & \frac{d\boldsymbol{BC}_f}{d\boldsymbol{p}} \end{bmatrix} \tag{2.61}$$

where $d\boldsymbol{x}_i^f \,/\, d\boldsymbol{x}_i$ and $d\boldsymbol{x}_i^f \,/\, \boldsymbol{p}$ are the state-transition matrices $\boldsymbol{\Phi}_i$ and $\boldsymbol{\Theta}_i$ for each segment respectively. With equations (2.60) and (2.61), the free-variable vector $\boldsymbol{X}$ is updated iteratively with either equation (2.30) or (2.31) depending if there are more free-variables than constraint equations.

CHAPTER 3. AGA TRAJECTORY OPTIMIZATION

The concept of performing aerogravity-assist (AGA) missions has been around since the early 1980s [13–16]. In addition to using the gravitational force of the flyby planet to change a vehicle's interplanetary trajectory, the aerodynamic forces of the planet's atmosphere can be harnessed as well, giving further control to this change. In a pure gravity-assist maneuver, the minimum flyby radius is limited by the planet's sensible atmosphere or the surface of the body, if no atmosphere exists. This altitude constraint limits the hyperbolic turn angle, defined as the angle between the incoming and outgoing V_∞ vectors. By taking advantage of the aerodynamic forces in an AGA maneuver, a larger turn angle can be achieved than that possible by a pure gravity assist, thus increasing the number of potential targets in the Solar System. To perform an AGA maneuver, a vehicle with a high lift-to-drag ratio (*L/D*) is desirable so that the energy lost to drag is minimized for an arbitrary turn angle. It was found that waveriders may be among the best candidate vehicles to perform or test AGA missions due to their potential for high *L/D* ratios [17–20].

Interplanetary trajectories to multiple bodies have been designed assuming patched conics between the planetary bodies and analytical (closed-form) approximations for the AGA maneuvers [21–25]. Indirect optimization techniques have also been applied to the AGA fly-through problem assuming a fixed vehicle maximum L/D (for example, $E^* = 5$) while maximizing or minimizing certain cost functionals [25–30]. For example, Lohar et al. [29] show how to maximize the heliocentric velocity of a vehicle as it exits the atmosphere, while subject to a convective heating constraint, and Lyons et al. [30] explore present a preliminary guidance algorithm based on drag-tracking.

The necessary conditions and formulation of boundary-value problems (BVPs) for AGA flight inside an atmosphere are discussed for different cost functionals and constraints. First, the equations of motion are presented and discussed with the assumptions for the model. Second, the two-point boundary-value problem (TPBVP) is setup and solved for the AGA trajectory with the minimum required $E^* = (L/D)_{\text{Max}}$ to complete the maneuver. This gives a lower bound that the aerodynamic characteristics of the vehicle need to meet. Third, the multi-point boundary-value problem (MPBVP) is setup and solved for the AGA trajectory with the minimum required E^* with a stagnation point convective heating-rate constraint the vehicle cannot exceed. The heating-rate constraint necessitates the inclusion of a state-variable inequality constraint (SVIC) which transforms the TPBVP into a MPBVP. Lastly, the TPBVP for the AGA trajectory that minimizes the total integrated convective heat-load is setup and solved. This cost functional and setup is different than the previous two solutions, as E^* is now a user-defined quantity and allows for more variability in the design of the vehicle model.

3.1 Equations of Motion

The equations of motion inside an atmosphere around a spherical rotating central body with inverse-square gravity are adopted from Vinh et al. [26]:

$$\dot{r} = V \sin\gamma \tag{3.1}$$

$$\dot{\theta} = \frac{V \cos\gamma \cos\psi}{r \cos\phi} \tag{3.2}$$

$$\dot{\phi} = \frac{V \cos\gamma \sin\psi}{r} \tag{3.3}$$

$$\dot{V} = -\frac{D}{m} - \frac{\mu}{r^2}\sin\gamma + \Omega^2 r \cos\phi\left(\sin\gamma\cos\phi - \cos\gamma\sin\phi\sin\psi\right) \tag{3.4}$$

$$\begin{aligned} \dot{\gamma} &= \frac{L}{mV}\cos\sigma - \left(\frac{\mu}{r^2 V} - \frac{V}{r}\right)\cos\gamma + 2\Omega\cos\phi\cos\psi \\ &+ \frac{\Omega^2 r}{V}\cos\phi\left(\cos\gamma\cos\phi + \sin\gamma\sin\phi\sin\psi\right) \end{aligned} \tag{3.5}$$

$$\begin{aligned} \dot{\psi} &= \frac{L}{mV\cos\gamma}\sin\sigma - \frac{V}{r}\cos\gamma\cos\psi\tan\phi \\ &+ 2\Omega\left(\tan\gamma\cos\phi\sin\psi - \sin\phi\right) - \frac{\Omega^2 r}{V\cos\gamma}\cos\phi\sin\phi\cos\psi \end{aligned} \tag{3.6}$$

where the states r, θ, ϕ, V, γ, ψ are the radial distance, longitude, latitude, planet-fixed velocity, planet-fixed flight-path angle, and planet-fixed heading respectively. L and D are the aerodynamic lift and drag respectively, Ω is the rotational rate of the body (with the atmosphere assumed to be rotating with the body at the same rate), σ is the bank angle, and μ is the standard gravitational parameter. It is important to note that V, γ, and ψ are derived with respect to the rotating body, and are not inertial values. Thus these equations are not valid outside the atmosphere, as the terms involving Ω would unrealistically dominate the motion far away from the central body. If the rotational effects from Ω are neglected, then V, γ, and ψ would become inertial values and the motion is valid everywhere. In this chapter (chapter 4) the inner planets are used as AGA bodies, and the rotation rate of the planets are neglected due to the slow rotations and short atmospheric flight durations. In chapter 5 however, an aerocapture model is applied at the outer planets, where the large size and fast turning rates cannot be left out to get an accurate model of the dynamics.

The Lift and Drag terms are defined as:

$$L = \tfrac{1}{2}\rho V^2 S C_L, \qquad D = \tfrac{1}{2}\rho V^2 S C_D \tag{3.7}$$

where ρ is the atmospheric density, S is the aerodynamic reference area, and C_L and C_D are the lift and drag coefficients respectively. The atmospheric density is modeled as exponential with the relationship:

$$\rho = \rho_0 \exp\left[-\beta\left(r - R_0\right)\right] \tag{3.8}$$

where ρ_0 and R_0 is the reference density and radius respectively, and β is the inverse scale-height of the atmosphere. Any model of the atmospheric density can be used, as long as the relationship between density and radius is C^1 continuous, or has one continuous derivative.

In sections 3.2 and 3.3, it is assumed the vehicle is controlled by pitching to increase or decrease the lift coefficient. In order to model the pitching, the lift coefficient is varied, making it possible to follow some specified path through the atmosphere. This control scheme is chosen to simplify the model as in Lohar et al. [29]. In section 3.4, the above control scheme is employed with the additional bank angle as a control. When the research was being conducted, numerical problems arose when bank angle was attempted to be added, however these issues were later overcome and bank angle was able to be included in the analysis.

The drag coefficient is modeled as a function of the lift coefficient according to Vinh et al. [26]:

$$C_D = C_{D_0} + K\left|C_L\right|^n \tag{3.9}$$

It is possible to eliminate C_D from the equations of motion by applying the following analytic expressions for $|C_L^*|$ and C_D^*

$$\left|C_L^*\right| = \left[\frac{C_{D0}}{(n-1)K}\right]^{\frac{1}{n}} \qquad C_D^* = \left(\frac{n}{n-1}\right)C_{D0} \tag{3.10}$$

where equation (3.10) is derived from the stationary value of L/D evaluated at C_L^*. Combining equations (3.9) and (3.10) allows the definition of a normalized drag coefficient, $\overline{C}_D$, to be a function of a normalized lift coefficient, $\overline{C}_L$:

$$\overline{C}_D = \frac{n-1}{n} + \frac{\left|\overline{C}_L\right|^n}{n} \tag{3.11}$$

Values of n between 1.5 and 2.0 in equation (3.11) have been used in literature to model the lift and drag coefficients at hypersonic speeds. Both Lohar et al. [29] and Henning et al. [31] compared the limiting values of n at 1.5 and 2.0 in their analysis, while Casoliva et al. [32] used an average value of 1.75. Section 3.2 compares solutions with $n = 1.5$ and 2, and sections 3.3 and 3.4 use $n = 1.75$.

3.2 Interplanetary AGA Tours with the Minimum $(L/D)_{\mathrm{Max}}$ Solution

Current peer-reviewed papers have treated the interplanetary and atmospheric flythrough phases separately and do not seek the minimum E^*. In the present work, the interplanetary trajectory and the local atmospheric fly-through are unified in a procedure to minimize a vehicle's maximum E^* needed to complete a given mission. As an example, a mission from Earth to Mars, then to Venus and back to Earth using AGA at Mars and Venus is considered.

Following Lohar et al. [29], it is assumed that the sole control mechanism used during the AGA maneuver is lift modulation by varying the angle of attack. The control parameter implemented in the equations of motion is the lift coefficient, C_L, corresponding to pitch modulation as the physical means to shape the trajectory. Normally, C_L is positively valued with the bank angle determining the orientation of the lift vector. In the present work the bank angle is excluded (as in Lohar et al. [29]), thus eliminating out-of-plane motion, and C_L is allowed to take on both positive and negative values. A negative C_L value indicates that the vehicle is flying upside-down, equivalently corresponding to a bank angle of 180 deg about the velocity vector.

The effects of heating and heat loading are not included in the present analysis. In practice, the heating brought on by hypersonic flight through an atmosphere can cause material to ablate from the structure of the vehicle, slightly changing the shape, and thus, also lowering the E^* the vehicle can produce. Possible remedies are to include a thermal protection system or to increase E^*, both of which add mass to the vehicle.

3.2.1 STOUR-AGA

The Satellite Tour Design Program (STOUR), capable of designing interplanetary missions using patched conics, was designed by engineers at JPL [34]. STOUR was then made fully automated by Williams [35], finding every interplanetary trajectory with only a few user inputs written on a scripted file. The inputs include a time-window of launch dates, the sequence of bodies used as gravity assists, maximum time-of-flight (TOF), and bounds on the incoming/outgoing $\boldsymbol{V}_\infty$ vectors. An algorithm to include aerogravity-assist maneuvers was designed by Bonfiglio and Longuski at Purdue University called STOUR-AGA [23]. This addition to STOUR takes the maximum vehicle *L/D* (which will from now on be designated E^*) as an additional input. STOUR computes all the possible patched-conic trajectories for the sequence over a range of designated dates, complete with the output of arrival and departure conditions at each planet. Trajectories are then chosen from the STOUR data that exhibit combined desirable traits such as low launch energy, short TOF, and low arrival V_∞'s.

To compute AGA trajectories, STOUR-AGA uses an E^* matching algorithm similar to the C_3 matching algorithm STOUR uses for traditional gravity assists. For a user-input E^*, STOUR-AGA implements a root-solving technique to match all possible trajectories that possess the same E^* [23], according to the equation:

$$\begin{aligned} E^* &= 2\{\ln[(V_\infty^{-2} + \mu/R_s)/(V_\infty^{+2} + \mu/R_s)]\}^{-1} \\ &\quad \times \{\phi - \sin^{-1}[1/(1 + V_\infty^{-2} R_s/\mu)] - \sin^{-1}[1/(1 + V_\infty^{+2} R_s/\mu)]\} \end{aligned} \tag{3.12}$$

where ϕ is the total turn angle around the planet and Rs is the altitude that the vehicle is assumed to be travelling for the trajectory. This analytical relationship assumes the AGA occurs at a constant altitude and relates the total hyperbolic turn angle of the AGA (inside and outside of the atmosphere) to common Keplerian orbital elements of interest. Consequently, an optimal path through the atmosphere can be found, resulting in the minimum E^* needed to match the V_∞^+ that propels the vehicle to the next body.

Formulation of the optimization for the atmospheric portion of the trajectory uses planar equations of motion for a lifting body around a non-rotating planet. An atmospheric model with density varying exponentially with altitude is assumed, with the reference altitude at the surface. The functional optimization problem is solved by forming a two-point boundary-value problem (TPBVP) in which the vehicle's lift coefficient, C_L, is the control. It is assumed that the vehicle can pitch or roll in such a fashion that the C_L is allowed to vary freely from zero to its maximum. The problem is restricted to planar motion and assumes an analytical normalized drag polar, where the drag coefficient, C_D, is dependent on C_L. The incoming and outgoing V_∞ vectors at the Mars and Venus flybys, which are designed via STOUR-AGA, specify the boundary conditions of the TPBVPs.

Finding the overall minimum E^* is achieved in two steps. Initially, the optimization problem is posed such that the velocity upon exiting the atmosphere is the cost functional to be maximized. The exit velocity is translated to the departure V_∞^+ speed using two-body energy conservation. The second step is to match the $\boldsymbol{V}_\infty^+$ vector to what STOUR-AGA has prescribed, characterized by the magnitude, V_∞^+, and the total turning angle, ϕ. This matching is done via an iterative process, in which both E^* and the total atmospheric turning angle θ_{atm} are gradually adjusted and the TPBVP is solved again at each iteration. In the final iteration, the minimum E^* is obtained which matches the exit $\boldsymbol{V}_\infty^+$ found in STOUR-AGA. The iteration process terminates when the desired exit conditions are met, guaranteeing that the spacecraft reaches its next destination.

The optimization problem is set up to maximize the velocity at atmospheric exit. It turns out that directly minimizing the L/D during the atmospheric fly-through while maintaining the constraint on the exit $\boldsymbol{V}_\infty^+$ leads to significant numerical complications. To get around the numerical problems the two-step method of first maximizing the atmospheric exit velocity and then correcting E^* and θ_{atm} to match the exit conditions dictated by STOUR-AGA is implemented. The method presented here gives the minimum E^* required to complete a given mission by performing the two-step optimization at every AGA fly-by body, and determining which AGA maneuver gives the limiting (highest) E^*.

3.2.2 Interplanetary Trajectory Selection Using STOUR

The examples chosen are EMVE trajectories in which both Mars and Venus are used as AGA bodies. Such missions could be of scientific interest since they would permit atmospheric sample returns, as well as demonstrating the technology required of AGA.

To produce candidate trajectories, a broad search in STOUR was performed. The launch dates that were searched span 25 years, ranging from March 2012 to March 2037 with a maximum TOF of 500 days. The launch V_∞ from Earth was chosen between 4 km/s to 7 km/s. A Delta IV or Atlas V launch vehicle is more than capable of delivering such launch energies assuming the vehicle has a reasonably small mass [36]. The values of the vehicle's maximum E^* considered were 3, 5, 7, and 10 [18]. The lower values are considered feasible for the near future, and the higher values may be achievable in the long term. The higher values are included to illustrate the flexibility and potential of AGA maneuvers in trajectory design.

An example of an EMVE broad search done in STOUR with $E^* = 3$ is shown in Figure 3.1. The figure is restricted to show launch dates between January 2016 and early March 2016 for visual clarity, as well as possessing Earth arrival V_∞'s of less than 10 km/s to allow for current entry technology to be used. Each point represents one trajectory with the launch date and TOF as the coordinates. The launch V_∞ is indicated by the number of the data point. The number 1 indicates a launch V_∞ between 4 and 4.75

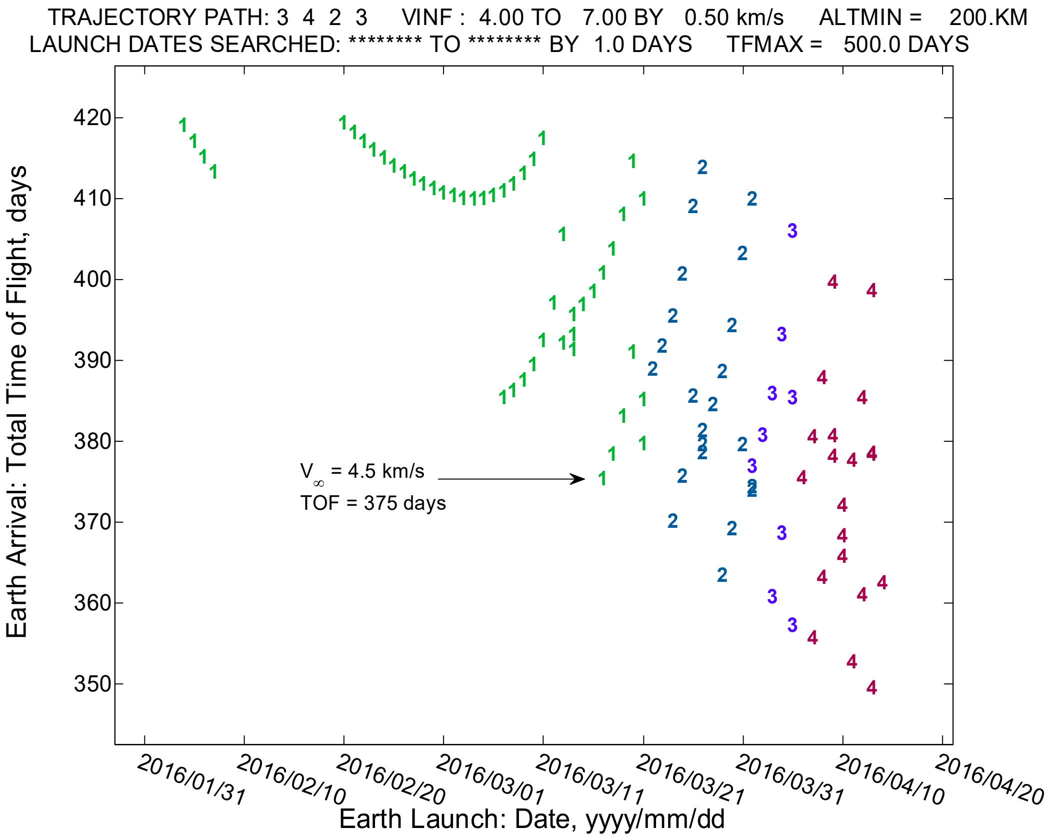

Figure 3.1: EMVE broad search for launch years 2015-2017 ($E^* = 3$, $V_\infty = 4\text{-}7$ km/s).

km/s, the number 2, between 4.75 and 5.5 km/s, the number 3, between 5.5 and 6.25 km/s, and the number 4, between 6.25 and 7 km/s. Based on Figure 3.1, a good launch opportunity used in this analysis occurs on March 17, 2016, as it possesses a relatively low TOF of 375 days, and a launch V_∞ of 4.5 km/s. The trajectory corresponds to the data point at the tip of the arrow with a corresponding number 1. Figure 3.2 shows a heliocentric view of this trajectory.

Other launch windows were found in the search but were not considered in this analysis. Two windows of opportunity with relatively low launch V_∞s occur between 2028 and 2029 as well as between 2034 and 2036.

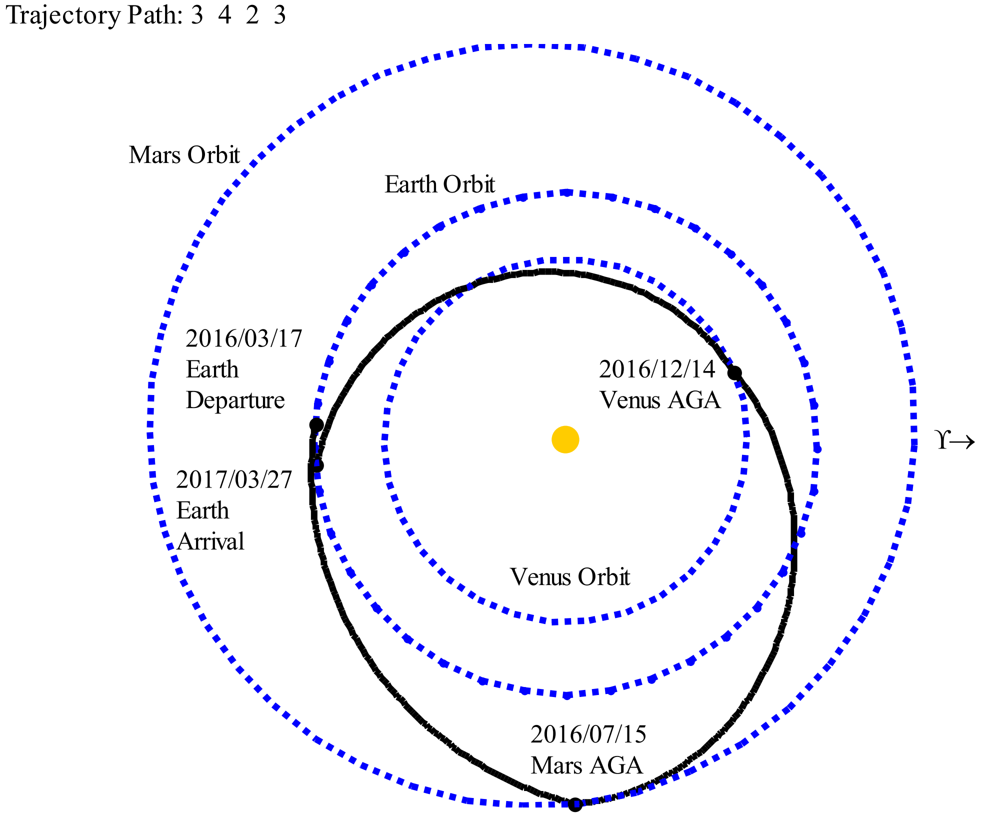

Figure 3.2: EMVE trajectory with E^* = 3 and launch V_∞ = 4.5 km/s for launch on March 22, 2016.

3.2.3 Approximate Calculation For AGA Boundary Conditions

For simplicity, an exponential atmospheric density model is assumed at the flyby planets of interest. The density, ρ, at a given altitude, r, is computed using equation (3.8) where R_0 and ρ_0 are the altitude and density on the surface, and β is the inverse of the density scale height. From Vinh et al. [26], scale heights of 10.6 km and 6 km for Mars and Venus, are used respectively.

STOUR-AGA provides the necessary incoming ($\boldsymbol{V}_\infty^-$) and outgoing ($\boldsymbol{V}_\infty^+$) vectors to get to the next target in a given tour, however specific vehicle parameters are necessary to describe the aerodynamics during flight. Finding appropriate vehicle parameters is found by analyzing where the vehicle maintains approximate level flight, denoted here as R_{ref}, as this altitude is where it receives the most lift.

To maintain level flight the applied and inertial accelerations must balance according the following equation:

$$g_{grav} + g_{aero} = g_{cent} \tag{3.13}$$

where g_{grav}, g_{aero}, and g_{cent} are the gravitational, aerodynamic, and centripetal accelerations, respectively. The accelerations are modeled using the following equations

$$g_{grav} = \frac{\mu}{r^2}, \qquad g_{aero} = \frac{\rho_0 \exp\left[-\beta\left(r - R_0\right)\right] V^2 S C_L^*}{2m}, \qquad g_{cent} = \frac{V^2}{r} \tag{3.14}$$

where the coefficient of lift is evaluated at maximum L/D in the g_{aero} term as the vehicle will produce the most efficient lift during the level flight. The two-body conservation of orbital energy equation is used to find the corresponding velocity at entry and departure of the atmosphere:

$$V = \sqrt{2\mu/r + V_\infty^2} \tag{3.15}$$

where we take r at the sensible edge of the planets' atmosphere. The atmosphere's edge is chosen to be 500 km altitude, but this can be any altitude where the density becomes negligible in the equations of motion. Since the entry and exit velocities at the atmosphere are known, the velocity the vehicle will have at R_{ref} is estimated by taking the average of the two.

The reference altitude, although only an approximation, is useful in characterizing a suitable vehicle in terms of its size-to-weight ratio and lift capability. By substituting equation (3.15) into equation (3.16), multiplying through by $2r/V^2$, rearranging, and evaluating r at R_{ref}, the following useful parameter is constructed:

$$\eta = \frac{\rho_0 \exp\left[-\beta\left(R_{ref} - R_0\right)\right] S C_L^* R_{ref}}{m} = 2\left(1 - \frac{\mu}{R_{ref} {V_{est}}^2}\right) \tag{3.16}$$

where V_{est} is the estimated velocity at the reference altitude, taken as the average of the speeds at the entrance and exit of the atmosphere.

The parameter η lends insight into the physics of the problem with respect to the vehicle's characteristics. For a given R_{ref}, there is a set of vehicle parameters that balances the vertical accelerations in equation (3.14). The desired reference altitude is targeted by appropriately adjusting η, or equivalently, by changing the ballistic characteristics of the vehicle. Being able to choose a reference altitude is useful for avoiding terrestrial objects that would otherwise hinder the vehicle's progress. As in Smith and Longuski [37], Table 3.1 contains the data that describes an example of an AGA vehicle. The mass, lifting area, maximum lift coefficient, along with the flyby speed determines the reference altitude at a given planet, and the efficiency of the optimal flythrough depends on E^*.

Smith and Longuski [37] show that the vehicle described in Table 3.1 would fly at reasonable altitudes (i.e. high enough above the surfaces) within the atmospheres of Mars

Table 3.1 Initial vehicle parameters

Parameter	Value
Mass [kg]	1336
Area [m^2]	5.574
C_L^*	0.0571
E^*	3.6603

and Venus. However, according to Anderson et al. [18], if the vehicles are designed specifically to fly at Mars or Venus, the aerodynamic characteristics would be different. For optimally shaped vehicles at Venus and Mars, lift coefficients of approximately 0.015 and 0.034, respectively are to be expected. If the vehicle design has slightly different lift coefficients than these at either planet, the result would be a higher or lower reference altitude.

At Mars for example, the atmosphere is very thin compared to Earth or Venus. A given vehicle will have a much lower reference altitude at Mars than at either Earth or Venus. In addition, Mars has some of the tallest mountains in the Solar System, with Olympus Mons reaching nearly 22 km above the mean radius of Mars. Assuming the lift coefficients given by Anderson et al. [18], a vehicle mass-to-area ratio of approximately 100 kg/m^2 would keep the vehicle around 25 to 30 km during cruise at the reference altitude, which clears the Martian mountains. At Venus, the same vehicle would cruise in a range of about 85 to 90 km, depending on the velocity. Venus' maximum elevation is approximately 11 km, meaning there is no terrestrial threat to the vehicle at Venus. The vehicle parameters used in the simulation are listed in Table 3.2, where R_{ref} is chosen to be 28 km at Mars to avoid terrestrial collisions. The same vehicle gives an R_{ref} of 63 km

Table 3.2 Vehicle parameters and constants used in EMVE simulation

Parameter	Mars	Venus
m [kg]	1500	1500
S [m^2]	15	15
C_L^*	0.034	0.015
E^*	3	3
η	23	5.9×10^4
ρ_0 [kg/m^3]	0.02	65
β [km^{-1}]	0.094	0.17

at Venus which is above any terrestrial threat there.

Once the $\boldsymbol{V}_\infty$ vectors and the vehicle parameters are specified, there exists enough information to transform the data into boundary conditions for the TPBVP. The height of the sensible atmosphere of 500 km altitude is used for both the arrival and departure boundary conditions for the position, r. The velocities at atmospheric entry and exit are found via equation (3.15). The reference altitude gives the approximate atmospheric turning angle, θ_{atm}. The true atmospheric turn angle is found via an iterative process, to match the $\boldsymbol{V}_\infty$ vectors given from STOUR-AGA, discussed in a later section. The problem is not strictly two-body due to the fact that the AGA maneuver rotates the line of apsides.

In order to obtain the approximate θ_{atm}, the true anomalies at entry and departure of the atmosphere are calculated. With R_{ref}, the true anomaly is found by rearranging the classic conic equation and isolating the true anomaly

$$f = \cos^{-1}\left\{\left[h^2/\left(r\mu\right)-1\right]/e\right\} \tag{3.17}$$

The expressions for the specific angular momentum, h, and the eccentricity, e, are

$$h = \left|\boldsymbol{r}\times\boldsymbol{V}\right| = R_{ref}V_{ref} \tag{3.18}$$

$$e = \left(V_{ref}^2 R_{ref}\big/\mu\right)-1 \tag{3.19}$$

where the reference altitude is used as an approximation for the periapsis radius of the AGA maneuver. The assumption that R_{ref} is the periapsis value is valid since the vehicle will be traveling at about that altitude for most of the time. Equation (3.15) is used again to get V_{ref} at both entry and exit of the atmosphere, which is substituted into equations (3.18) and (3.19). It is important to note that V_{ref} is different at atmospheric entry and

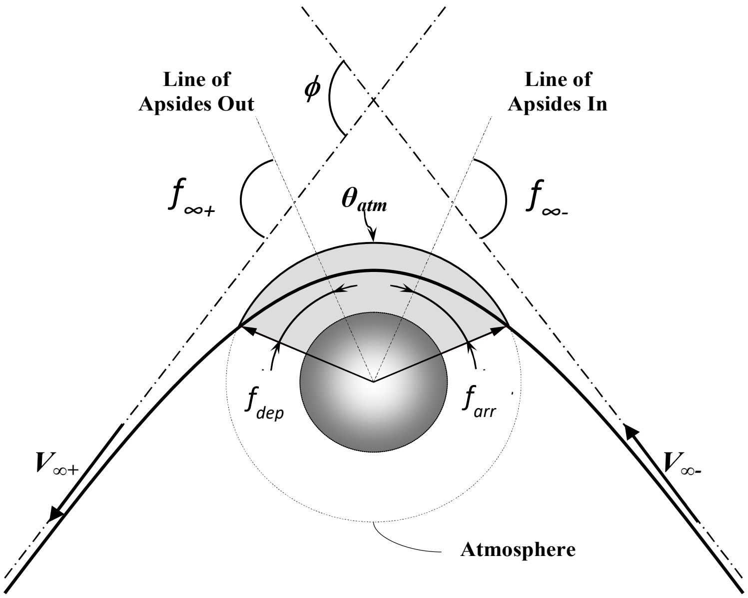

Figure 3.3 Planar view of an AGA maneuver.

departure, and is in fact a velocity the vehicle will never achieve due to the energy dissipation from atmospheric drag. With the approximate values for h at atmospheric entry and departure, it is possible to find the corresponding true anomalies using equation (3.17). The boundary condition for θ_{atm} is then calculated using the angle geometry of the AGA maneuver. Figure 3.3 highlights the relationship between the angles involved in the AGA maneuver. The shaded area on Figure 3.3 represents the atmospheric portion of flight, which is spanned by θ_{atm}. The schematic in Figure 3.3 is presented again in a more convenient form in Figure 3.4.

Equation (3.20) gives the expression for the approximate θ_{atm}, using the geometry of AGA.

$$\theta_{atm} = \pi + \phi - \left(f_{\infty}^{+} - f_{\infty}^{-}\right) + \left(f_{dep} - f_{arr}\right) \tag{3.20}$$

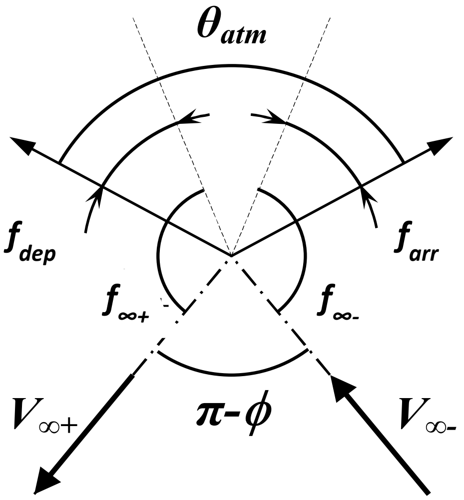

Figure 3.4: AGA angle relationships between incoming and outgoing hyperbolic trajectories.

The angle ϕ is the total turning angle between the incoming and outgoing $\boldsymbol{V}_\infty$ vectors. This angle is found using equation (3.21), which comes from the definition of the inner product of two vectors.

$$\phi = \cos^{-1}\left(\frac{\boldsymbol{V}_\infty^{-} \bullet \boldsymbol{V}_\infty^{+}}{\left|\boldsymbol{V}_\infty^{-}\right|\left|\boldsymbol{V}_\infty^{+}\right|}\right) \tag{3.21}$$

With all the available boundary conditions, an optimization problem is now posed with the objective of maximizing the velocity upon exiting the atmosphere.

3.2.4 Nondimensional Equations of Motion

A further simplification is made to equations (3.1) – (3.6), assuming only planar motion which reduces the number of dependent variables from six to four.

$$\begin{aligned} \frac{dr}{dt} &= V \sin \gamma \\ \frac{d\theta}{dt} &= \frac{V \cos \gamma}{r} \\ \frac{dV}{dt} &= \frac{-D}{m} - \frac{\mu}{r^2} \sin \gamma \\ V \frac{d\gamma}{dt} &= \frac{L}{m} - \frac{\mu}{r^2} \cos \gamma + \frac{V^2 \cos \gamma}{r} \end{aligned} \tag{3.22}$$

where the bank angle term that would appear in the first term of the right-hand side of the last in equation (3.22) (i.e. $L/m \cos \sigma$, where σ is the bank angle) has been excluded in favor of the control scheme described earlier, involving angle of attack, enforcing the trajectory to remain planar.

The four state variables are r, θ, V, and γ, which correspond to the radius, atmospheric turning angle, velocity, and flight path angle, respectively. The four equations of motion are given as first-order derivatives with respect to time, however time is not a variable of interest in this problem, nor do any available boundary conditions exist. Instead, the independent variable is transformed from time to θ and its boundary conditions are known with zero being the initial condition and θ_{atm} being the final condition. Changing independent variables in equation (3.22), gives with the following reduced equations of motion.

$$\begin{aligned} \frac{dr}{d\theta} &= r \tan \gamma \\ \frac{dV}{d\theta} &= -\frac{\rho V S r C_D}{2m \cos \gamma} - \frac{\mu \tan \gamma}{rV} \\ \frac{d\gamma}{d\theta} &= \frac{\rho S r C_L}{2m \cos \gamma} - \frac{\mu}{rV^2} + 1 \end{aligned} \tag{3.23}$$

where the lift and drag variables have been replaced with the relationships in equation (3.7). For numerical simplicity the equations of motion are nondimensionalized with the following substitutions for the radius and velocity respectively:

$$\tilde{r} = \frac{r}{R_0}, \qquad \tilde{u} = \frac{V^2 R_0}{\mu}, \qquad \xi = \frac{\rho_0 S C_L^* R_0}{2m} \tag{3.24}$$

It is important to note that ξ in equation (3.24), although similar to η in equation (3.16), does not possess the same value. The parameter ξ is merely used for making the equations of motion more compact, whereas η is used to determine the characteristics of the vehicle. Furthermore, the density is nondimensionalized by the reference density ρ_0 for compactness.

$$\tilde{\rho} = \frac{\rho}{\rho_0} = \exp\left[-\beta R_0 \left(\tilde{r} - 1\right)\right] \tag{3.25}$$

Finally, the normalized lift and drag coefficients are introduced:

$$\tilde{C}_L = \frac{C_L}{C_L^*}, \qquad \tilde{C}_D = \frac{C_D}{C_D^*} \tag{3.26}$$

where C_L^* and C_D^* correspond to the lift and drag coefficients when the *L/D* is at its maximum value, E^*. Combining equations (3.15) and (3.24) – (3.26), and substituting into equation (3.23), results in the following nondimensionalized equations of motion used in this analysis:

$$\begin{aligned} \frac{d\tilde{r}}{d\theta} &= \tilde{r}\tan\gamma \\ \frac{du}{d\theta} &= -\frac{\tilde{u}\xi\tilde{r}\tilde{C}_D}{E^*\cos\gamma}\tilde{\rho} - \frac{2\tan\gamma}{\tilde{r}} \\ \frac{d\gamma}{d\theta} &= \frac{\xi\tilde{r}\tilde{C}_L}{2\cos\gamma}\tilde{\rho} - \frac{1}{\tilde{r}\tilde{u}} + 1 \end{aligned} \tag{3.27}$$

3.2.5 Optimization of Atmospheric Flight

The optimization problem is solved in two steps. First, the optimal trajectory is defined as a TPBVP that maximizes the velocity as the vehicle exits the atmosphere, using the approximate boundary conditions derived from Equations (3.14) – (3.21). This is equivalent to minimizing the amount of velocity lost to drag over the course of the trajectory. Second, depending on whether the departure $\boldsymbol{V}_{\infty}^{+}$ vector possesses the same magnitude and direction as determined by STOUR-AGA, both E^{*} and θ_{atm} are reduced (or increased) and the TPBVP is re-solved iteratively until the departure $\boldsymbol{V}_{\infty}^{+}$ vector is matched to within a specified tolerance.

3.2.5.1 Two-Point Boundary Value Problem

The cost functional for the problem is

$$\text{Max J} = V\left(t_f\right) = V\left(\theta_f\right) \tag{3.28}$$

where the independent variable of time has been replaced by the longitude θ; this substitution does not change the physical meaning of equation (3.28). The cost functional is subject to the equations of motion given in equation (3.27). The Hamiltonian is given by:

$$H = L + \boldsymbol{\lambda}^{T}\boldsymbol{f} = \lambda_r\left(\tilde{r}\tan\gamma\right) - \lambda_u\left[\frac{\tilde{u}\xi\tilde{r}\tilde{C}_D}{E^{*}\cos\gamma}\tilde{\rho} + \frac{2\tan\gamma}{\tilde{r}}\right] + \lambda_\gamma\left(\frac{\xi\tilde{r}\tilde{C}_L}{2\cos\gamma}\tilde{\rho} - \frac{1}{\tilde{r}\tilde{u}} + 1\right) \tag{3.29}$$

The costate equations are obtained by applying the Euler-Lagrange theorem:

$$\frac{d\lambda_r}{d\theta} = -\frac{\partial H}{\partial \tilde{r}}, \qquad \frac{d\lambda_u}{d\theta} = -\frac{\partial H}{\partial u}, \qquad \frac{d\lambda_\gamma}{d\theta} = -\frac{\partial H}{\partial \gamma} \tag{3.30}$$

For brevity, these equations are omitted. The optimal control law is found by computing $\partial H / \partial \tilde{C}_L = 0$ and yields:

$$\tilde{C}_L = \frac{E^* \lambda_\gamma}{2\tilde{u}\lambda_u} \tag{3.31}$$

when n = 2, and

$$\tilde{C}_L = \left(\frac{E^* \lambda_\gamma}{2\tilde{u}\lambda_u}\right)^2 \operatorname{sgn}\left(\frac{E^* \lambda_\gamma}{2\tilde{u}\lambda_u}\right) \tag{3.32}$$

when n = 1.5, and sgn is the signum function.

Because only five boundary conditions are known, a set of transversality conditions is necessary for a well-defined TPBVP. The transversality conditions used to obtain a full set of eight boundary conditions is found with:

$$\left[H d\theta - \lambda^T d\boldsymbol{x} \right]\Big|_{\theta_0}^{\theta_f} + d\Phi = 0 \tag{3.33}$$

where $\Phi = \tilde{u}\left(\theta_f\right)$ is the Mayer form of the cost functional. Expanding equation (3.33) gives:

$$\lambda_{\gamma_0} d\gamma_0 - \lambda_{\gamma_f} d\gamma_f + \left(1 - \lambda_{u_f}\right) d\tilde{u}_f = 0 \tag{3.34}$$

The λ costates in equation (3.34) correspond to the states that are, thus far, unconstrained. Because the states and costates are independent and the differentials of the final values of the states are nonzero, the coefficients are chosen such that equation (3.34) is satisfied:

$$\lambda_\gamma\left(\theta_0\right) = 0, \qquad \lambda_\gamma\left(\theta_f\right) = 0, \qquad \lambda_u\left(\theta_f\right) = 1 \tag{3.35}$$

Eight boundary conditions have now been acquired, which is needed for a well-defined TPBVP.

Note that in equations (3.31) and (3.32) the control law is expressed as a ratio of two costates. Upon defining another new costate as the ratio of two costates:

$$C_5 = \frac{\lambda_r}{\lambda_u} \tag{3.36}$$

The number of overall costates required in the optimization problem can be reduced from three to two. This reduction is convenient from a numerical perspective, as only five differential equations need to be integrated instead of six. Taking the differentials of equations (3.31) and (3.36) with $n = 2$, and substituting the necessary equations of motion from equation (3.27), gives the new costate differential equations:

$$\begin{aligned}
\frac{d\tilde{C}_L}{d\theta} &= \frac{\tilde{r}\xi \sin\gamma\left(1-\tilde{C}_L^2\right)}{4\cos^2\gamma}\tilde{\rho} - \frac{\tilde{r}E^* C_5}{2\tilde{u}\cos^2\gamma} + \frac{E^*}{\tilde{u}\tilde{r}\cos^2\gamma} + \frac{2\tilde{C}_L \tan\gamma}{\tilde{u}\tilde{r}} + \frac{2\tilde{C}_L^2}{\tilde{u}\tilde{r}E^*} \\
\frac{dC_5}{d\theta} &= -C_5\tan\gamma + \frac{\tilde{u}\xi\left(1+\tilde{C}_L^2\right)\left(1-\tilde{r}\beta R_0\right)}{2E^*\cos\gamma}\tilde{\rho} - \frac{2\tan\gamma}{\tilde{r}^2} - \frac{2\tilde{C}_L}{\tilde{r}^2 E^*} \\
&\quad - \frac{\tilde{u}\xi\tilde{C}_L^2\left(1-\tilde{r}\beta R_0\right)}{E^*\cos\gamma}\tilde{\rho} - \frac{\tilde{r}\xi C_5\left(1+\tilde{C}_L^2\right)}{2E^*\cos\gamma}\tilde{\rho} + \frac{2\tilde{C}_L C_5}{\tilde{u}\tilde{r}E^*}
\end{aligned} \tag{3.37}$$

When $n = 1.5$, the new costate differential equations become:

$$\begin{aligned}
\frac{d\tilde{C}_L}{d\theta} &= -\frac{C_5 E^* \tilde{r}\left|\tilde{C}_L\right|^{1/2}}{\tilde{u}\cos^2\gamma} + \frac{\xi\tilde{r}\left|\tilde{C}_L\right|^{1/2}\left(1-\left|\tilde{C}_L\right|^{3/2}\right)\sin\gamma}{3\cos^2\gamma}\tilde{\rho} + \frac{2E^*\left|\tilde{C}_L\right|^{1/2}}{\tilde{r}\tilde{u}\cos^2\gamma} + \frac{4\left|\tilde{C}_L\right|^{3/2}}{E^*\tilde{r}\tilde{u}} \\
&\quad + \frac{4\tilde{C}_L\tan\gamma}{\tilde{r}\tilde{u}} \\
\frac{dC_5}{d\theta} &= -C_5\tan\gamma + \frac{\tilde{u}\xi\left(1-\beta R_0\tilde{r}\right)\left(1-\left|\tilde{C}_L\right|^{3/2}\right)}{3E^*\cos\gamma}\tilde{\rho} - \frac{2\tan\gamma}{\tilde{r}^2} - \frac{2\left|\tilde{C}_L\right|^{1/2}\operatorname{sgn}\tilde{C}_L}{E^*\tilde{r}^2} \\
&\quad - \frac{C_5\xi\tilde{r}\left(1+2\left|\tilde{C}_L\right|^{3/2}\right)}{3E^*\cos\gamma}\tilde{\rho} + \frac{2C_5\left|\tilde{C}_L\right|^{1/2}\operatorname{sgn}\tilde{C}_L}{E^*\tilde{r}\tilde{u}}
\end{aligned} \tag{3.38}$$

Now that a well-defined TPBVP has been posed, the optimal open-loop control history can be obtained numerically.

3.2.5.2 V_∞ Matching

After finding the maximum atmospheric departure velocity obtained from the optimization scheme, which has a corresponding departure hyperbolic excess velocity, $\boldsymbol{V}_{\infty opt}$, it must be matched to the prescribed $\boldsymbol{V}_\infty^+$ that came out of STOUR-AGA. The $\boldsymbol{V}_\infty^+$ matching is done iteratively by adjusting both E^* and θ_{atm} and re-solving the TPBVP, to find the overall mission minimum E^*. After an AGA trajectory is computed, the outgoing $\boldsymbol{V}_{\infty opt}$ vector will differ slightly from the desired $\boldsymbol{V}_\infty^+$ from STOUR-AGA, as illustrated in Fig. 4. The error between $\boldsymbol{V}_\infty^+$ and $\boldsymbol{V}_{\infty opt}$, $\Delta\boldsymbol{V}$, is a vector with both direction and magnitude. The error in direction is characterized by the angle $\Delta\phi$, found via the difference between equation (3.21) and the desired turn angle, while the magnitude error is found using equation (3.39):

$$\Delta V^2 = V_\infty^{+2} + V_{\infty opt}^2 - 2V_\infty^+ V_{\infty opt}\cos(\Delta\phi) \tag{3.39}$$

In the computations $\Delta\phi$ turns out to be small, equation (3.39) becomes a perfect square,

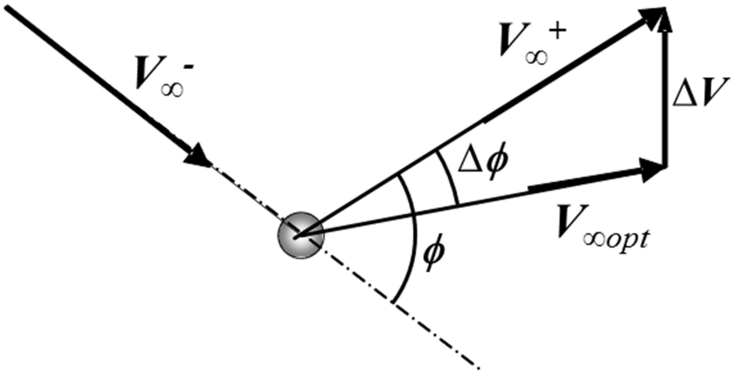

Figure 3.5: $\boldsymbol{V}_\infty^+$ Matching Schematic

and the difference between the velocity magnitudes is approximated by:

$$\Delta V = V_{\infty}^{+} - V_{\infty opt} \tag{3.40}$$

A line search is performed that adjusts both E^* and θ_{atm} iteratively until the error between the V_∞ vectors is eliminated. The velocity magnitude at atmospheric departure is most directly influenced by E^* since it determines the amount of velocity lost to drag. E^* is updated using the following formula:

$$E^* = E_0^* \left(1 - \omega \Delta V\right) \tag{3.41}$$

where E_0^* is the initial E^* used when solving the TPBVP the first time. θ_{atm} is adjusted in a similar fashion to correct the direction error $\Delta\phi$, with:

$$\theta_{atm} = \theta_{atm,0} \left(1 - \kappa \Delta\phi\right) \tag{3.42}$$

where $\theta_{atm,0}$ is the initial θ_{atm} used when solving the TPBVP the first time. The variables ω and κ are arbitrary parameters that were picked by trial and error. The parameters can be made larger or smaller to hasten the calculations or to avoid overshooting the desired values and should be updated simultaneously to speed up convergence. Each time these variables are updated, the TPBVP is re-solved and the errors are recalculated. This process continues until the desired departure conditions are met.

3.2.5.3 Results

Figure 3.6 – Figure 3.8 contain the optimal altitude, velocity, and *L/D* profiles for the Mars atmospheric flythrough for the trajectory presented in Figure 3.3 with a launch date of March 22, 2016. Venus trajectory profiles look similar, so they are omitted for brevity. The vehicle enters the atmosphere and steadily plunges deeper until it reaches the reference altitude of approximately 28 km above the surface as illustrated in Figure 3.6.

As expected, the vehicle spends much of its time around this altitude. The velocity of the vehicle with respect to Mars is given in Figure 3.7. First the vehicle gains velocity by trading potential energy for kinetic energy as it quickly plunges into the atmosphere, but then abruptly loses the kinetic energy accumulation as the aerodynamic forces build when reaching the reference altitude. During this period, the vehicle steadily loses speed due to drag. Upon the ascent to exit the atmosphere, the vehicle loses additional speed, but at a slower rate, as aerodynamic forces become less pronounced at higher altitudes.

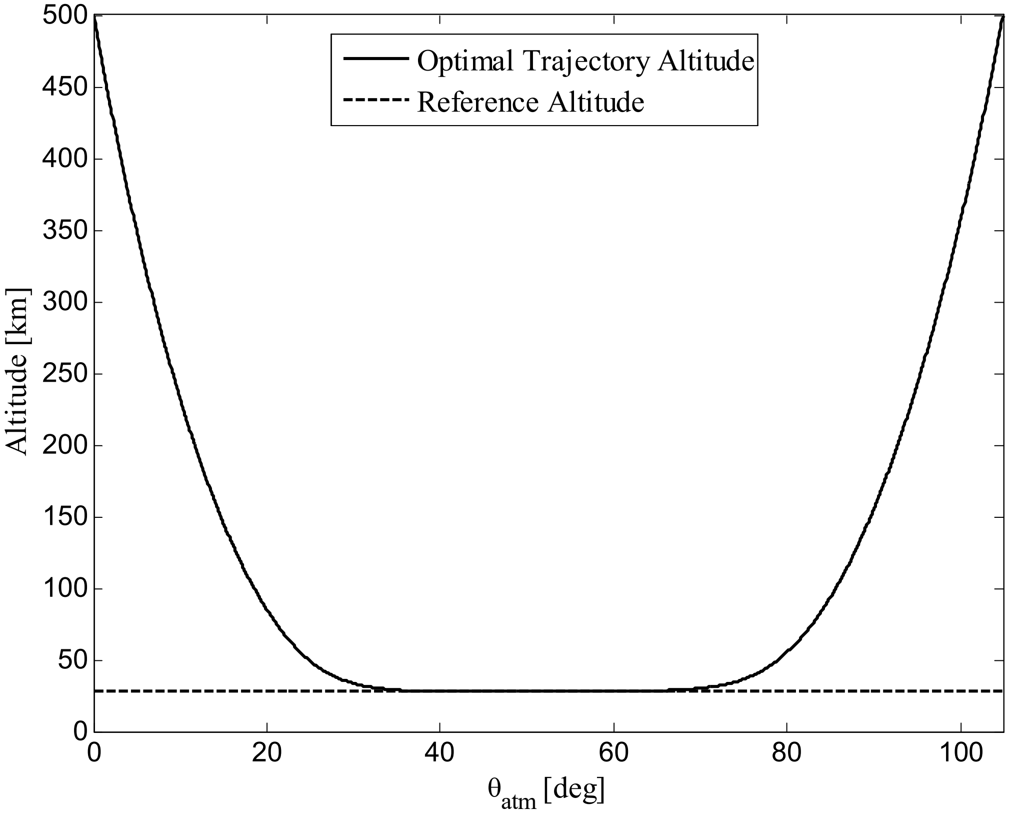

Figure 3.6: Altitude vs θ_{atm} above Mars.

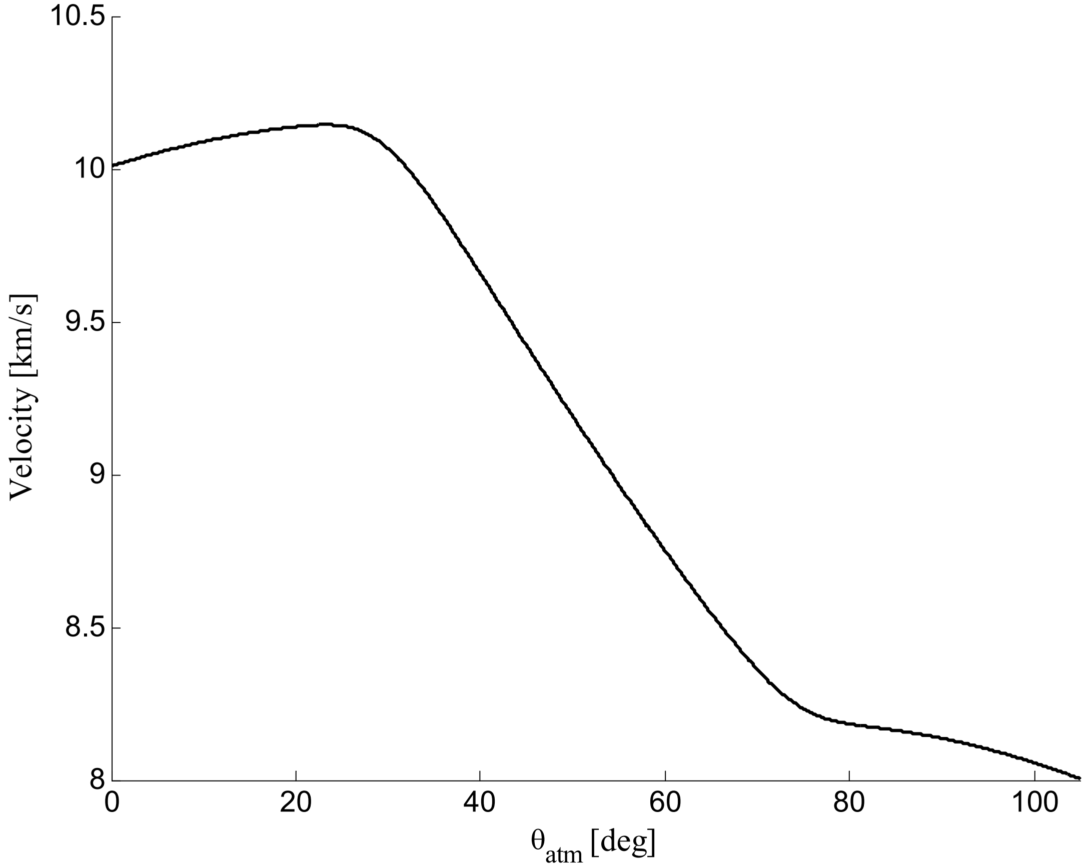

Figure 3.7: Velocity vs θ_{atm} above Mars.

The question arises as to why the velocity history in Figure 3.7 would be the optimal solution, as the vehicle seems to lose the majority of its speed during the cruising period. The answer is more apparent when looking at the *L/D* history of the vehicle in Figure 3.8. During the cruising period at the reference altitude, the

vehicle's prescribed E^*, is achieved and held constant, meaning that the vehicle was receiving the most efficient aerodynamic lift possible. As described earlier, the lift coefficient is allowed to take on positive and negative values due to the exclusion of a

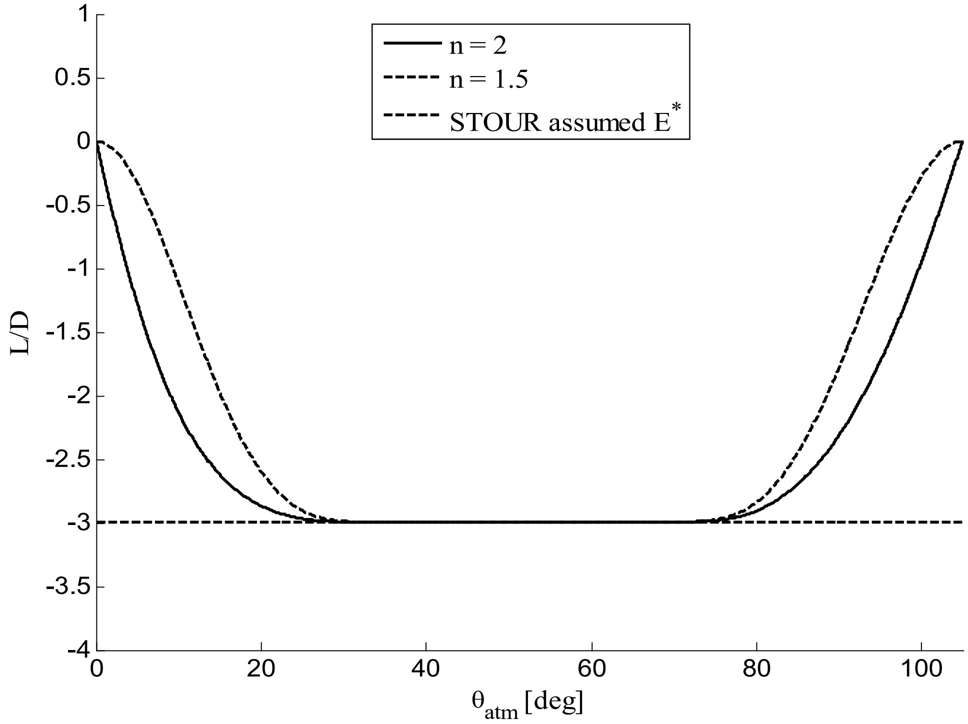

Figure 3.8: *L/D* vs. θ_{atm} above Mars.

bank angle. In Figure 3.8, the L/D scale is negative in the figure to indicate that the lift vector is pointed down towards the planet.

Note that in Figure 3.6 and Figure 3.7, only the position and velocity histories with a drag polar using $n = 2$ is shown. With the hypersonic model of $n = 1.5$, the figures are very similar making them difficult to distinguish. However the control history shown in Figure 3.8 makes the differences in the two models more apparent. The main difference in the optimal control for each case occurs during the descending and ascending phases of the atmospheric flythrough. The subsonic model ($n = 2$) calls for a steeper *L/D* at first with a more gradual shift into the maximum *L/D* region, while the hypersonic model ($n = 1.5$) dictates the opposite behavior. Figure 3.8 suggests that there is an interesting, but insignificant difference in using one aerodynamic model over the other, since the vehicle spends most of the trajectory at the reference altitude where the *L*/*D* is closest to E^*. Additionally, the *L*/*D* values are negative corresponding to the vehicle flying upside-down in the model.

Overall, STOUR's approximations for E^* are fairly accurate. After matching the outgoing $\boldsymbol{V}_\infty^+$ vectors with equations (3.41) and (3.42), the optimal (minimum) E^* needed for the atmospheric flythroughs at Mars and Venus are computed as 2.994 and 3.015 respectively. Thus an overall mission minimum E^* for a vehicle performing such atmospheric sample return at Mars and Venus is 3.015. With the process outlined in this paper, a minimum E^* can be calculated for any interplanetary mission employing AGA.

A method for identifying and optimizing AGA trajectories for exploration of the Solar System has been developed. In previous work in the literature, the design of AGA missions has been treated as two separate problems. In the first case the interplanetary trajectories are represented by conics that are patched together via a closed-form approximation for the AGA. In the second case, research has centered on the details of the atmospheric fly-through phase for a given (but not minimum) E^* while often satisfying, for example, a heating constraint.

In the present work the interplanetary trajectory and atmospheric fly-through trajectory are unified in a process to determine an overall mission minimum E^*. Starting with an automated patched-conic approach, interplanetary trajectories were found which employed AGA maneuvers. The characteristics of these AGA maneuvers (e.g. initial $E^*$and assumed fly-by altitude, R_s) were determined for the interplanetary trajectories using a simplified model. For the atmospheric fly-through portion of the trajectory, a more sophisticated model was used to find the minimum lift-to-drag ratio, E^*. In order to avoid certain numerical difficulties, the minimization of E^* was obtained in a two-step process. First, based on the interplanetary trajectories found using the patched-conic approach, two-point boundary value problems were set up to maximize the velocity at departure of the atmosphere at each AGA body. Second, E^* and θ_{atm} are corrected using a line search approach to match the $\boldsymbol{V}_\infty^+$ vectors from STOUR-AGA. The overall minimum E^* required of the vehicle needed to complete a given mission is found by taking the limiting case of the AGA maneuvers in the mission (the one with the largest E^*).

An example of an Earth-Mars-Venus-Earth atmospheric sample return mission using AGA is calculated with a total flight time of just over a year with an E^* of 2.994 for Mars and 3.015 for Venus (i.e. Venus is the limiting case). The aerodynamic models based on the parabolic (n = 2) and hypersonic (n = 1.5) drag polars produced very similar results with the exception in the upper atmosphere where the aerodynamic effects are insignificant. This short-duration trajectory suggests the possibility of a mission that can serve as both a technology demonstrator and as an atmospheric science sample return mission.

3.3 Minimum AGA $(L/D)_{Max}$ Solution with Convective Heating-Rate Constraint

Section 3.2 detailed a method to obtain the optimal E^* for interplanetary tours using AGA, but neglected to consider a key element to make AGA realizable in the near future: heating. This section uses the necessary conditions for a local optimum using optimal control theory employing state-variable inequality constraints (SVIC). The method of obtaining interplanetary AGA tours is the same as in section 3.2, but now a convective heating-rate constraint is imposed on the atmospheric portions of the trajectory.

In atmospheres of considerable density, AGA maneuvers produce a considerable amount of heating that can lead to ablation. Ablation can warp the outside structure of the vehicle, causing the aerodynamic properties of the vehicle to change or the structure to break apart causing mission failure. In order to mitigate vehicle warping due to excessive heating, the trajectory of the vehicle through the atmosphere can be flown such that the heating rate is kept within tolerable levels. For the current investigation, the heating rate measured at the stagnation point is maintained under a prescribed maximum value.

The two main types of heating involved during atmospheric flight are convective heating and radiative heating. Lohar et al. has shown that at low altitudes, the effects of radiative heating dominate the convective heating, and the reverse is true at high altitudes [29]. Since AGA maneuvers are performed at higher altitudes, to minimize energy loss due to drag as well as avoid terrestrial obstacles, the convective heating rate is constrained in this investigation.

The stagnation point convective heating rate, $\dot{q}_c$, is computed via Sutton and Graves [39]:

$$\dot{q}_c = k\sqrt{\frac{\rho}{r_n}}V^3 \tag{3.43}$$

where k is a constant dictated by the atmospheric composition, r_n is the radius of the stagnation region (commonly located at the tip, or nose of the vehicle), V is the velocity, and the density ρ is given by equation (3.8). During the atmospheric fly-through, $\dot{q}_c$ is kept below a prescribed maximum value, $\dot{q}_{c,\max}$, introducing the following SVIC to the optimal control problem:

$$S = \dot{q}_c \leq \dot{q}_{c,\max} \tag{3.44}$$

Equation (3.44) is used to mitigate the effects of vehicle degradation due to aerodynamic heating during an AGA maneuver.

An additional change to the formulation of optimal AGA tours from section 3.2 is the full three degree-of-freedom model and six differential equations of motion are now used, for an inverse-square gravitational potential with nonrotating atmosphere:

$$\begin{aligned}
\bar{r}' &= \bar{v}\sin\gamma \\
\theta' &= \frac{\bar{v}\cos\gamma\cos\psi}{\bar{r}\cos\phi} \\
\phi' &= \frac{\bar{v}\cos\gamma\sin\psi}{\bar{r}} \\
\bar{v}' &= -\frac{\bar{\rho}\xi\bar{v}^2\left(n-1+\left|\bar{C}_L\right|^n\right)}{nE^*} - \frac{\bar{\mu}}{\bar{r}^2}\sin\gamma \\
\gamma' &= \xi\bar{v}\bar{C}_L\bar{\rho}\cos\sigma - \left(\frac{\bar{\mu}}{\bar{r}^2\bar{v}} - \frac{\bar{v}}{\bar{r}}\right)\cos\gamma \\
\psi' &= \xi\bar{v}\bar{C}_L\bar{\rho}\frac{\sin\sigma}{\cos\gamma} - \frac{\bar{v}}{\bar{r}}\cos\gamma\cos\psi\tan\phi
\end{aligned} \tag{3.45}$$

The equations of motion in equation (3.45) now have a nondimensionalized time as the independent variable with:

$$\tau = t\frac{V_0}{R_0}, \qquad (.)' = \frac{d(.)}{d\tau} \tag{3.46}$$

and have the following additional nondimensional variables:

$$\bar{v} = V / V_0, \qquad \bar{\mu} = \mu / (R_0 V_0^2) \tag{3.47}$$

The exponential atmospheric density model in equation (3.8) is used along with the analytic drag polar in equation (3.11) with $n = 2$. Also, the bank angle σ is included as a second control variable in the optimal control formulation.

3.3.1 Optimal Control Problem with Heat Constraint

The AGA optimal control problem is solved using an indirect method with Pontryagin's Maximum Principle. The cost functional is the maximization of the final velocity upon exiting the atmosphere:

$$\text{Max } J = \Phi(t_f, \boldsymbol{x}_f) = V(t_f) = \bar{v}(\tau_f) \tag{3.48}$$

subject to the equations of motion in equation (3.45), the SVIC in equation (3.44), and a number of boundary conditions specified for an AGA maneuver (described later). First the order of the SVIC must be determined by taking total derivatives of equation (3.44) with respect to nondimensional time until a control appears explicitly. The nondimensional form of equation (3.44) is:

$$S = \exp\left[-\tfrac{1}{2}\beta R_0\left(\bar{r}-1\right)\right]\bar{v}^3 \le \bar{\dot{q}}_{c,\max} \tag{3.49}$$

where the limiting value of the stagnation point convective heating rate on the right-hand side of equation (3.49) in nondimensional form is:

$$\bar{\dot{q}}_{c,\max} = \frac{\dot{q}_{c,\max}}{kV_0^3}\sqrt{\frac{r_n}{\rho_0}} \tag{3.50}$$

Taking the first total derivative of equation (3.49) with respect to τ yields:

$$S' = -\bar{v}^2\left(\tfrac{1}{2}\bar{v}^2\beta R_0 + \frac{3\bar{\mu}\sin\gamma}{\bar{r}^2}\right)e^{-\frac{1}{2}\beta R_0(\bar{r}-1)} - \frac{3\xi\bar{v}^4(n-1+\bar{C}_L^n)}{nE^*}e^{-\frac{3}{2}\beta R_0(\bar{r}-1)} \tag{3.51}$$

The control $\overline{C}_L$ appears explicitly in equation (3.51), indicating the state-variable inequality constraint is of first order. Equation (3.51) is adjoined to the Hamiltonian with a time-varying Lagrange multiplier, *κ*. The new Hamiltonian takes the form:

$$\begin{aligned} H &= \lambda_{\bar{r}}\bar{v}\sin\gamma + \lambda_\theta \frac{\bar{v}\cos\gamma\cos\psi}{\bar{r}\cos\phi} + \lambda_\phi \frac{\bar{v}\cos\gamma\sin\psi}{\bar{r}} \\ &+ \lambda_{\bar{v}}\left(-\frac{\bar{\rho}\xi\bar{v}^2\overline{C}_D}{E^*} - \frac{\bar{\mu}}{\bar{r}^2}\sin\gamma \right) + \lambda_\gamma \left[\xi\bar{v}\overline{C}_L\bar{\rho}\cos\sigma - \left(\frac{\bar{\mu}}{\bar{r}^2\bar{v}} - \frac{\bar{v}}{\bar{r}} \right)\cos\gamma \right] \\ &+ \lambda_\psi \left(\xi\bar{v}\overline{C}_L\bar{\rho}\frac{\sin\sigma}{\cos\gamma} - \frac{\bar{v}}{\bar{r}}\cos\gamma\cos\psi\tan\phi \right) + \kappa S' \end{aligned} \tag{3.52}$$

The necessary conditions for local optimality come from applying the Euler-Lagrange theorem along with Pontryagin's Maximum Principle to set up a multi-point boundary-value problem (MPBVP). The necessary conditions are:

$$\boldsymbol{\lambda}' = -\frac{\partial H}{\partial \boldsymbol{x}}, \qquad \frac{\partial H}{\partial \boldsymbol{u}} = \boldsymbol{0}, \qquad \frac{\partial^2 H}{\partial \boldsymbol{u}^2} \le 0 \tag{3.53}$$

where $\boldsymbol{u} = [C_L, \sigma]^T$ is the vector of control parameters. The evaluation of the first of equation (3.53) is omitted for brevity. Evaluating the second of equation (3.53), the control law on arcs not on the SVIC boundary is

$$\tan\sigma = \frac{\lambda_\psi}{\lambda_\gamma\cos\gamma}, \qquad \overline{C}_L = \left[\frac{E^*}{\bar{v}\lambda_{\bar{v}}} \sqrt{\frac{\lambda_\psi^2}{\cos^2\gamma} + \lambda_\gamma^2} \right]^{\frac{1}{n-1}} \tag{3.54}$$

with $\kappa = 0$. Since the cost functional is being maximized, the Hessian matrix resulting from the third of equation (3.53) must be negative semi-definite. On boundary arcs of the SVIC, the control law for $\overline{C}_L$ is found by setting equation (3.51) equal to zero:

$$\bar{C}_L = \left\{1 - n\left[1 + \frac{E^*}{6\eta\bar{\rho}}\left(\beta R_0 + \frac{6\bar{\mu}\sin\gamma}{\bar{v}^2\bar{r}^2}\right)\right]\right\}^{\frac{1}{n}} \tag{3.55}$$

Since the bank angle control σ did not appear in equation (3.51), it obeys the first of equation (3.54) over the entire trajectory. The equation for κ changes when the trajectory hits a boundary subarc:

$$\kappa = \begin{cases} 0 & \tau \notin \left[\tau_{entry}, \tau_{exit}\right] \\ -\dfrac{\partial H / \partial \bar{C}_L}{\partial S' / \partial \bar{C}_L} & \tau \in \left[\tau_{entry}, \tau_{exit}\right] \end{cases} \tag{3.56}$$

where [t_{entry}, t_{exit}] is the time interval on the boundary subarc.

The necessary conditions also dictate a set of transversality conditions to obtain a well-defined boundary-value problem. These transversality conditions are found by finding the initial and final conditions such that

$$\left[H d\tau - \boldsymbol{\lambda}^T d\boldsymbol{x}\right]\Big|_{\tau_0}^{\tau_f} + d\Phi = 0 \tag{3.57}$$

Or upon evaluation:

$$\lambda_\gamma(\tau_0) = 0, \quad \lambda_\psi(\tau_0) = 0, \quad H(\tau_f) = 0, \quad \lambda_{\bar{v}}(\tau_f) = -1, \quad \lambda_\gamma(\tau_f) = 0, \quad \lambda_\psi(\tau_f) = 0 \tag{3.58}$$

Finally, the MPBVP has tangency and jump conditions to maintain at the entrance of a boundary arc [6]. The tangency conditions require equation (3.49) set to its maximum value at the entry interface ($\tau = \tau_{entry}$):

$$\exp\left[-\tfrac{1}{2}\beta R_0\left(\bar{r}(\tau_1) - 1\right)\right]\bar{v}(\tau_1)^3 = \dot{\bar{q}}_{c,\max} \tag{3.59}$$

A set of jump conditions exist that must satisfy:

$$\lambda(\tau_1^-) = \lambda(\tau_1^+) + \pi \left.\frac{\partial S}{\partial \boldsymbol{x}}\right|_{\tau=\tau_{entry}} \tag{3.60}$$

where π is an additional constant Lagrange multiplier accounting for the discontinuity in both $\lambda_{\bar{r}}$ and $\lambda_{\bar{v}}$. Since the Hamiltonian is regular [6], the condition that the Hamiltonian is constant across τ_{entry} and τ_{exit} can be replaced with the control $\bar{C}_L$ being continuous instead:

$$\bar{C}_L(\tau_{entry}^-) = \bar{C}_L(\tau_{entry}^+), \qquad \bar{C}_L(\tau_{exit}^-) = \bar{C}_L(\tau_{exit}^+) \tag{3.61}$$

The advantage using equation (3.61) is that it is more numerically tractable than using the Hamiltonian, as the Hamiltonian is a function of more variables.

All other physical boundary conditions to construct a well-formulated MPBVP are known. Integrating equations (3.45) with the control laws in equations (3.54) and (3.55), adhering to the interior and jump conditions of equations (3.60) and (3.61), while satisfying all boundary and transversality conditions in equation (3.58) gives a locally optimal solution.

3.3.2 Numerical Results

All numerical results are found by solving the MPBVP using the multiple-shooting technique. Due to sensitivities, the results were iteratively found via a homotopy method by first solving the problem without a convective stagnation point heating rate constraint, then increasing $\dot{q}_{c,\max}$ to the desired maximum using the solution to the previous iteration as the guess for the for the next one.

Table 3.3 Parameters and constants used in Venus AGA with heating-rate constraint

Parameter	Symbol	Value	Units
Vehicle mass	m	1500	kg
Aerodynamic reference area	S	15	m^2
Analytic drag polar exponent	n	2	—
Lift coefficient at maximum *L*/*D*	C_L^*	0.0868	—
Inverse scale-height	β	1/15.9	km
Reference density	ρ_0	65	kg/m^3
Reference radius	R_0	6052	km
Height of atmosphere	h_{atm}	500	km
Nose radius	r_n	0.3	m
Sutton-Graves constant	k	1.9027e-8	$kg^{1/2}/m$
Total hyperbolic turn angle	δ	64.6	deg
Arrival hyperbolic excess speed	V_∞^-	8.842	km/s
Departure hyperbolic excess speed	V_∞^+	6.488	km/s
Maximum convective heating rate allowed	$\dot{q}_{c,max}$	800	W/cm^2

An example case for AGA with a convective heating-rate constraint is computed at Venus for the interplanetary trajectory depicted in Figure 3.2. The relevant vehicle parameters and arrival and departure conditions are listed in Table 3.3. The physical boundary conditions are computed via the method outlined in section 3.2.3.

The solutions of the unconstrained (no heat-rate limitation) and constrained trajectories are in Figure 3.9 – Figure 3.12. When no heating-rate limit is imposed on the trajectory, E^* must be at least 3.06 in order to satisfy the boundary conditions on the V_∞^+ vector and get to the next interplanetary target (Mars). However, when the SVIC for the convective heating-rate is involved, E^* must be equal to 5.23, a 2.17 increase from the unconstrained case. The need for the increase in E^* becomes apparent when looking at Figure 3.9, as the altitude profile for the constrained case is about 40 km higher than the unconstrained case at the lowest point. In order to generate enough lift to be able to fly higher, E^* must be increased accordingly. Since the convective heating-rate relationship

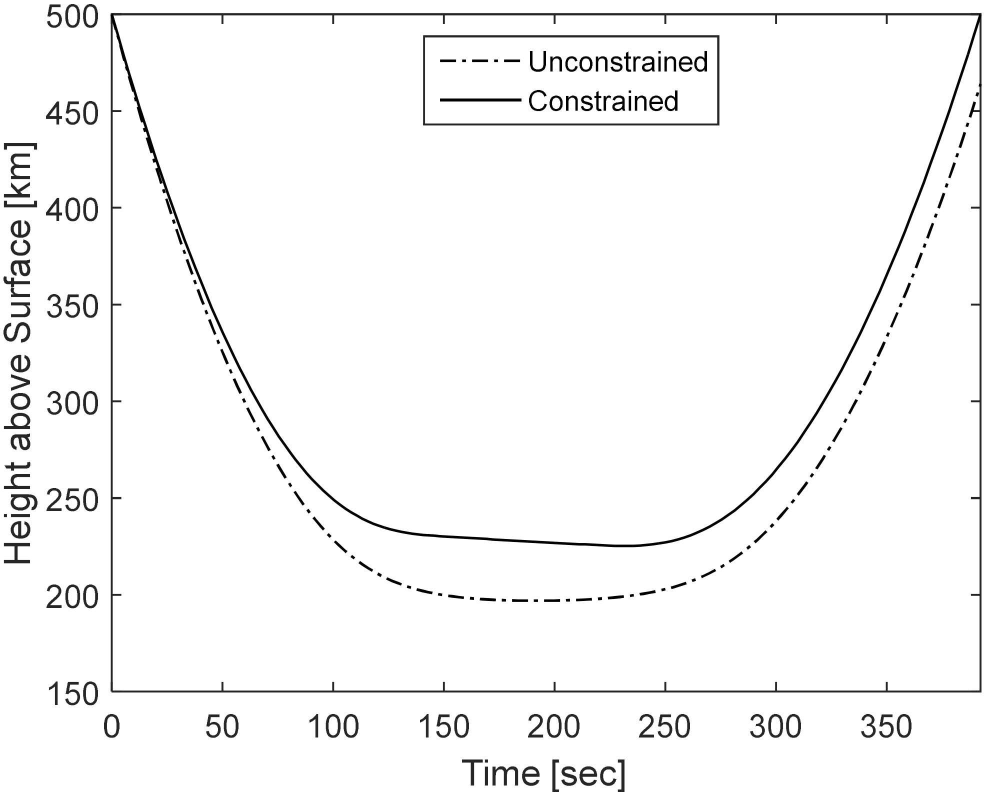

Figure 3.9: Altitude versus time for constrained and unconstrained trajectories.

in equation (3.43) is function of both atmospheric density (hence radius) and velocity, it makes sense to fly higher and hit the less dense air at when at high speeds.

The velocity profile in Figure 3.10 shows the constrained case losing its speed faster than the unconstrained case when flying at the bottom of the "trough" shaped out by the altitude profile. Since the convective heating-rate is a function of the speed cubed, there is a need to bleed off the high speeds to maintain the heating-rate constraint. However since the heating-rate is a function of both speed and altitude, the optimal control history reduces them in a way that the cost functional is minimized as well.

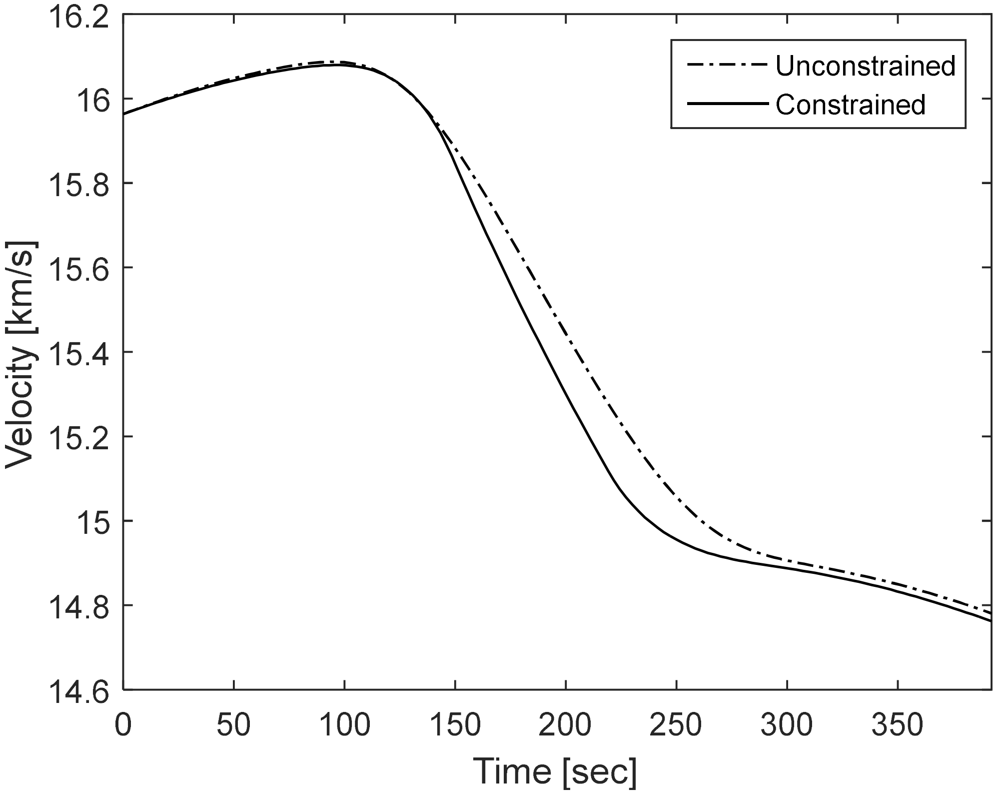

Figure 3.10: Velocity versus time for constrained and unconstrained trajectories.

Figure 3.11 shows the convective heating-rate, and the reason behind the drastic increase required in E^*. The constrained case plateaus at the maximum allowable heating-rate between approximately 130 – 240 seconds, while the unconstrained case shoots up to a maximum value of 2178 W/cm^2. For many thermal protection system materials, a high heating-rate will cause heavy ablation. In AGA one of the goals is to fly a trajectory with only a minimal amount of ablation, as the aerodynamic characteristics would change, compromising the mission.

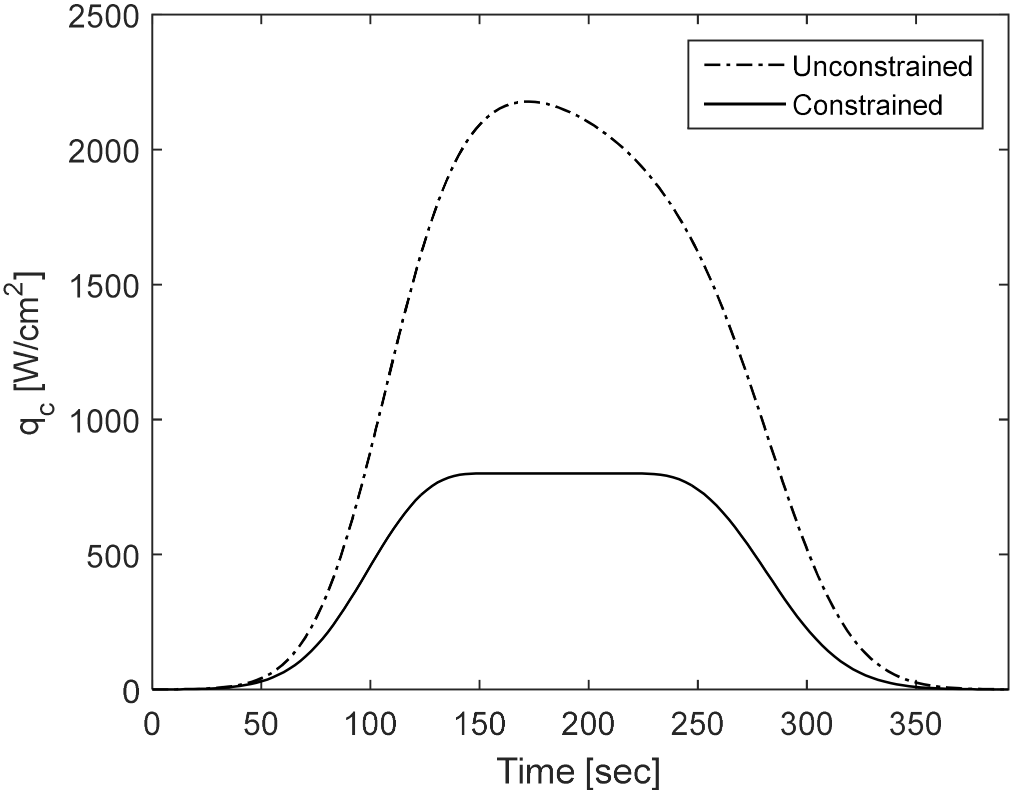

Figure 3.11: Convective heat-rate versus time for constrained and unconstrained trajectories.

The control history of *L*/*D* displayed in Figure 3.12 shows a clear distinction between the maximum E^* required for the constrained and unconstrained trajectories. When unconstrained, the *L*/*D* smoothly climbs to the maximum E^* of 3.06 during descent, then reverts back to zero during ascent. With the heating-rate constraint, the control shows three separate phases in the trajectory. The first phase during descent has the control quickly rise to the maximum E^* of 5.23, then decrease to a value of ~2.5 when the SVIC for the heating-rate constraint becomes active at ~150 seconds. Then the control effort increases fairly linearly until ~230 seconds when the vehicle departs the SVIC

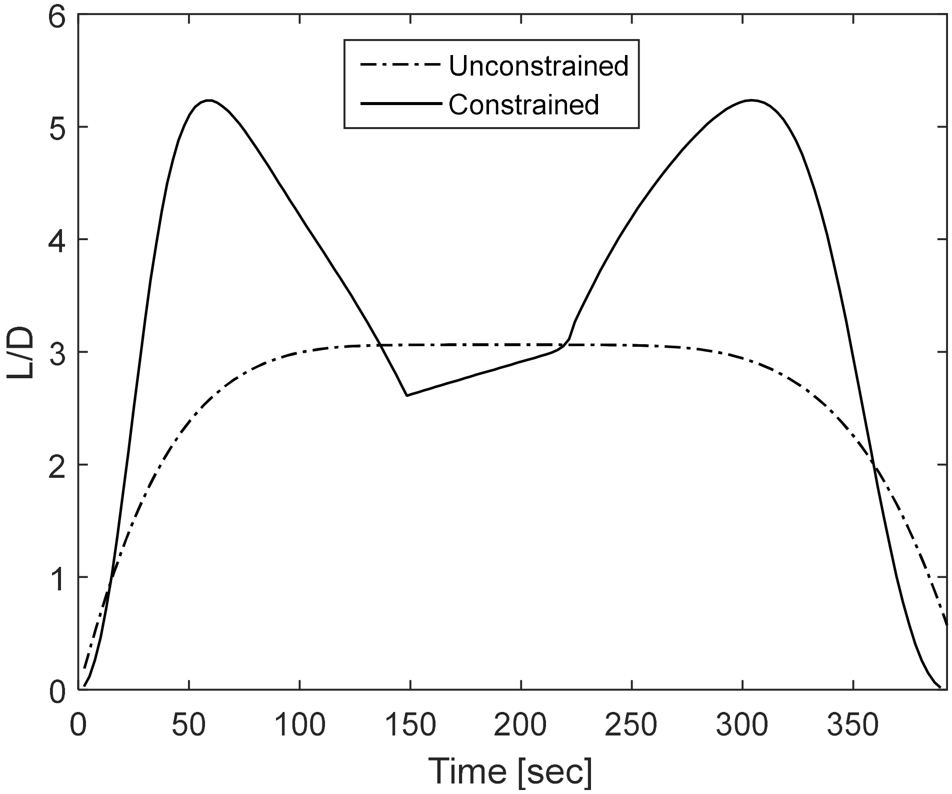

Figure 3.12: *L*/*D* versus time for constrained and unconstrained trajectories.

boundary and increases the E^* back to the maximum. Finally when the vehicle ascends out of the atmosphere, the control effort goes back to zero.

3.4 Minimum AGA Heat Load Solution

The heating rate and subsequent total heat load may be one of the most mission critical aspects of an AGA maneuver [27]. In section 3.3, a method for obtaining the minimum E^* solution for AGA subject to a convective heating-rate constraint in the form of a SVIC was developed. If the AGA vehicle has a high enough E^*, it can fly high up enough in an atmosphere to reduce the convective heating-rate in equation (3.43), as it is a function of atmospheric density (which is a function of altitude). However, the vehicle must remain in the atmosphere over a long duration of time at hypersonic speeds meaning it accrues a high total heat load. The current section formulates an optimal control problem to minimize the total convective heat-load. Numerical problems in directly targeting the outgoing V_∞^+ vector in the boundary conditions are overcome via the implementation of a collocation scheme. In sections 3.2 and 3.3 the V_∞^+ vector direction and magnitude were solved in an iterative way, by matching E^* and θ_f via the method outlined in section 3.2.5.2. Now both the V_∞^+ magnitude and direction are satisfied in the boundary conditions of the optimal control problem itself.

Using equation (3.15) along with equations (3.20) and (3.21), the physical boundary conditions are rewritten in terms of the state variables, and an optimal control problem is solved using indirect methods. In order to numerically solve the resulting two-point boundary value problem, a 3rd-order Gauss-Lobatto collocation scheme is used to get an accurate initial guess, and the solution is refined using a multiple shooting technique with an eighth-order Runge-Kutta Prince-Dormand explicit integrator. The absolute and relative integration error tolerances are both set to 10^{-16}.

The properties of the vehicle modeled in this analysis are defined in terms of E^*, C_L^*, S, and m. A previous paper by the authors found the minimum required E^* for a given mission by solving an optimal control problem based on maximizing atmospheric exit velocity [31]. However the solution to the previous paper was found by targeting the outgoing V_∞ (boundary conditions) by adjusting E^*, limiting the choice of vehicle parameters to a restricted set. The solution in this paper is an improvement in two ways. First, the characteristics defining the vehicle have more room for design, as E^* can now be chosen, and the optimal control history can be adjusted to meet the design requirement (assuming the vehicle can generate the required lift to complete the AGA maneuver). Second, the optimal trajectory is a local minimum for the total heat load the vehicle will accumulate, as stated by the necessary conditions derived from Pontryagin's Minimum Principle [3–5].

The equations of motion are for a spherical, non-rotating planet, given by equations (3.1) – (3.6) with Ω set to zero. The aerodynamics is modeled by the analytic drag polar given by equation (3.11) with $n = 1.75$, and the atmospheric density is modeled exponentially via equation (3.8). The equations of motion are nondimensionalized with the same parameters in section 3.3, yielding the form of equation (3.45).

As the vehicle traverses the atmosphere, some of the kinetic energy is dissipated into heat, affecting the structure of the vehicle. In flythroughs deep in the atmosphere, major heating can lead to ablation problems that can warp the outside structure of the vehicle. If the outside structure were to change during flight, the aerodynamic properties of the vehicle could degrade. In order to mitigate vehicle degradation due to excessive heating, the trajectory of the vehicle through the atmosphere should be flown such that the heating rate, and thus the integrated heat load, is kept within the capabilities of the thermal protection system. For this investigation, the heat load at the stagnation point is minimized.

The two main types of heating involved during atmospheric flight are convective heating and radiative heating. Lohar et al. has shown that at low altitudes the effects of radiative heating dominate the convective heating and the reverse is true at high altitudes

[29]. Since AGA maneuvers are performed at high altitudes the convective heating rate is the more important metric in this investigation.

The stagnation point convective heating rate is computed via Sutton and Graves [39] in equation (3.43). The radiative heating rate is calculated via

$$\dot{q}_r = C r_n^a \rho^b f(V) \tag{3.62}$$

where C, a, b, and $f(V)$ depend on a body's atmosphere. Different models for the constants in equation (3.62) for Earth and Mars have been given by Tauber and Sutton [40], and Brandis and Johnston [41]. Although this study only focuses on minimizing the convective heat load the radiative heating is still calculated to show that it is small in comparison to convective heating for AGA maneuvers.

3.4.1 Optimal Control Problem FormulationmI

The AGA optimal control problem is solved using an indirect method with Pontryagin's Minimum Principle. The cost functional is chosen to minimize the total heat load found by integrating equation (3.43):

$$\text{Min J} = \int_0^{t_f} k\sqrt{\frac{\rho}{r_n}} V^3 dt = \int_0^{\tau_f} \sqrt{\bar{\rho}}\bar{v}^3 d\tau \tag{3.63}$$

where the far right-hand side of the equation is in nondimensional form. Equation (3.63) is subject to the equations of motion in equation (3.45), as well as appropriate boundary conditions for a specific AGA flythrough.

Using an indirect method, the optimization problem is posed as a two-point boundary-value problem (TPBVP). The Hamiltonian takes the form

$$\begin{aligned} H &= \sqrt{\bar{\rho}}\bar{v}^3 + \lambda_{\bar{r}}\bar{v}\sin\gamma + \lambda_\theta \frac{\bar{v}\cos\gamma\cos\psi}{\bar{r}\cos\phi} + \lambda_\phi \frac{\bar{v}\cos\gamma\sin\psi}{\bar{r}} \\ &+\lambda_{\bar{v}}\left(-\xi\frac{\bar{v}^2\bar{C}_D}{E^*}\bar{\rho} - \frac{\bar{\mu}}{\bar{r}^2}\sin\gamma\right) + \lambda_\gamma\left[\xi\bar{v}\bar{C}_L\bar{\rho}\cos\sigma - \left(\frac{\bar{\mu}}{\bar{r}^2\bar{v}} - \frac{\bar{v}}{\bar{r}}\right)\cos\gamma\right] \\ &+\lambda_\psi\left(\xi\bar{v}\bar{C}_L\bar{\rho}\frac{\sin\sigma}{\cos\gamma} - \frac{\bar{v}}{\bar{r}}\cos\gamma\cos\psi\tan\phi\right) \end{aligned} \tag{3.64}$$

The necessary conditions for local optimality come from applying the Euler-Lagrange theorem along with Pontryagin's Minimum Principle. They are:

$$\boldsymbol{\lambda}' = -\frac{\partial H}{\partial \boldsymbol{x}}, \qquad \frac{\partial H}{\partial \boldsymbol{u}} = \mathbf{0}, \qquad \frac{\partial^2 H}{\partial \boldsymbol{u}^2} \geq 0 \tag{3.65}$$

where $\boldsymbol{u}$ is the vector of control parameters, in this case $\boldsymbol{u} = [\,\bar{C}_L\,,\, \sigma]^T$. The evaluation of the first and third of equation (3.65) is omitted for brevity. Evaluating the second of equation (3.65) while ensuring the resulting Hessian matrix from the third of equation (3.65) is positive semi-definite, the control laws are:

$$\sin\sigma = \frac{-\lambda_\psi}{\sqrt{\lambda_\gamma^2\cos^2\gamma + \lambda_\psi^2}}, \qquad \cos\sigma = \frac{-\lambda_\gamma\cos\gamma}{\sqrt{\lambda_\gamma^2\cos^2\gamma + \lambda_\psi^2}} \tag{3.66}$$

$$\bar{C}_L = \left|\frac{-E^*}{\bar{v}\lambda_{\bar{v}}}\left(\frac{\lambda_\psi^2}{\cos^2\gamma} + \lambda_\gamma^2\right)^{\frac{1}{2}}\right|^{\frac{1}{n-1}} \operatorname{sgn}\left[\frac{-E^*}{\bar{v}\lambda_{\bar{v}}}\left(\frac{\lambda_\psi^2}{\cos^2\gamma} + \lambda_\gamma^2\right)^{\frac{1}{2}}\right] \tag{3.67}$$

Conditions for local optimality require a set of transversality conditions to ensure a well-defined TPBVP. The transversality conditions are found by finding the terms of the nonzero differentials on the boundaries such that

$$\left(H d\tau - \boldsymbol{\lambda}^T d\boldsymbol{x}\right)\Big|_{\tau_0}^{\tau_f} = 0 \tag{3.68}$$

subject to:

$$d\mathbf{\Psi} = 0 \tag{3.69}$$

where $\mathbf{\Psi}$ is the vector of boundary conditions. For this study, the entry radius, longitude, latitude, and speed, as well as the final radius, latitude, and speed are known. Additionally the total turn angle δ is known so that the vehicle leaves on its departing V_∞^+ vector. Knowing these values, the boundary conditions vector is:

$$\begin{aligned}\psi^T = \big[&\bar{r}(\tau_0) - \bar{r}_0, \quad \theta(\tau_0) - \theta_0, \quad \phi(\tau_0) - \phi_0, \quad \bar{v}(\tau_0) - \bar{v}_0, \\ &\bar{r}(\tau_f) - \bar{r}_f, \quad \phi(\tau_f) - \phi_f, \quad \bar{v}(\tau_f) - \bar{v}_f, \quad \delta - \delta_d\big] = \mathbf{0}\end{aligned} \tag{3.70}$$

where δ_d is the desired turning angle. Taking the total differential of equation (3.70), the only boundary condition with a non-trivial evaluation is δ.

Switching notation for the hyperbolic turn angle in equation (3.20) from ϕ to δ and solving for δ yields:

$$\delta = \theta_{atm} - \pi + (f_\infty^+ - f_\infty^-) - (f_{dep} - f_{arr}) \tag{3.71}$$

where $\theta_{atm} = \theta(t_f)$. From the geometry of an AGA around a planet, the right-hand side of equation (3.71) can be expressed as a function of the initial and final radii, velocities and flight path angles when entering and exiting the atmosphere respectively. The true anomalies are

$$f_\infty^{-/+} = \mp\cos^{-1}\left[-1\Big/\sqrt{1 + (\bar{v}_{0,f}^2 - 2/\bar{r}_{0,f})\bar{r}_{0,f}^2\bar{v}_{0,f}^2\cos^2\gamma(t_{0,f})}\right] \tag{3.72}$$

and

$$f_{arr/dep} = \mp\cos^{-1}\left[\frac{\bar{r}_{0,f}\bar{v}_{0,f}^2\cos^2\gamma(t_{0,f}) - 1}{\sqrt{1 + (\bar{v}_{0,f}^2 - 2/\bar{r}_{0,f})\bar{r}_{0,f}^2\bar{v}_{0,f}^2\cos^2\gamma(t_{0,f})}}\right] \tag{3.73}$$

Evaluating equations (3.68) and (3.69), the following set of transversality conditions is obtained:

$$H(t_f)=0, \qquad \lambda_\gamma(t_0)+\lambda_\theta(t_f)\frac{\partial\delta}{\partial\gamma_0}, \qquad \lambda_\gamma(t_f)-\lambda_\theta(t_f)\frac{\partial\delta}{\partial\gamma_f}, \qquad \lambda_\psi(t_{0,f})=0 \tag{3.74}$$

where the partial derivatives in equation (3.74) are omitted for brevity.

In summary, a well-defined two-point boundary value problem has been posed. Equation (3.45) and the first of equation (3.65) give the state and costate differential equations, equations (3.66) and (3.67) give the control law, and equations (3.70) and (3.74) give the necessary number of boundary conditions for a local minimum.

3.4.2 Results

An example atmospheric sample return mission using AGA at Mars with a flyby of Venus is presented and compared with a very similar trajectory without using traditional gravity assists. The vehicle is launched from Earth orbit on November 22,

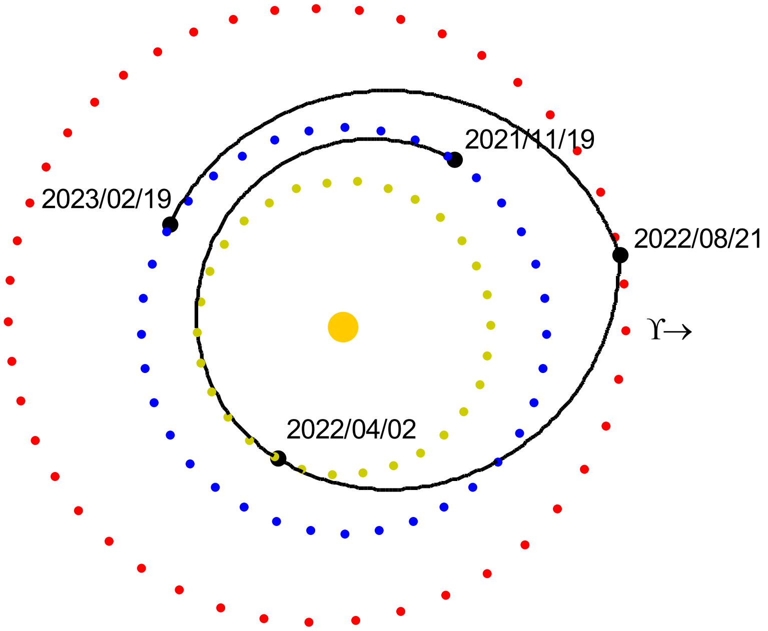

Figure 3.13: EVME trajectory using AGA at Mars, with encounter dates.

2021, makes a flyby of Venus on April 2, 2022, performs an AGA at Mars on August 21, 2022, and then returns to Earth on February 19, 2023 (referred to as an EVME trajectory).

The relevant mission characteristics are displayed in Table 3.4, and the interplanetary trajectory is presented in Figure 3.13. EVME trajectories with $E^* = L/D_{max} = 3.0$, and possessing low Earth launch and arrival V_∞s were searched for over a 20-year time period in STOUR-AGA (2020–2040), and the trajectory was selected from a Pareto front analysis. The trajectory presented in Figure 3.13 is very similar to an EVME trajectory (with launch date November 22, 2021) found as an alternative to the Inspiration Mars mission proposed for early 2018 [42]. Although a mission using AGA would not have humans on board until after the technology is proven, the comparison of the AGA trajectory to a similar trajectory using only gravity assists gives insight to its benefits. At Mars, the total turn angle is augmented by 40 degrees, and the resulting Earth arrival V_∞ is reduced by 2.9 km/s.

Next the atmospheric flythrough is optimized using a vehicle with planetary constants, selected aerodynamic properties, and boundary values, given in Table 3.5 (all other physical boundary values not given in Table 3.5 are set to zero). The vehicle values including r_n, m, S, and C_L^* are from Casoliva et al. [32], while E^* was set to a value more representative of the one used in STOUR-AGA. The initial and final radii (r_0, r_f) are is

Table 3.4 Interplanetary Trajectory Characteristics

Parameter	AGA	GA
Launch Date	November 19, 2021	November 22, 2021
Earth Launch V_∞ [km/s]	4.5	4.5
Earth Arrival V_∞ [km/s]	3.63	6.53
TOF [days]	458	582
δ [degrees]	72.6	32.5

the sum of the Mars radius and height of the sensible atmosphere. The entry and exit speeds (V_0, V_f) are found using equation (3.15), and their respective V_∞s at Mars arrival and departure. The desired hyperbolic turn angle, δ_d, is found with equation (3.21) with the V_∞ vectors given by STOUR-AGA.

Table 3.5: Constants, vehicle properties, and boundary values

Name	Symbol	Value	Units
Reference density	ρ_0	0.02	kg/m^3
Reference radius (Mars radius)	R_0	3397	km
Inverse scale height	β	1/7.1	km^{-1}
Sensible height of atmosphere	h_{atm}	163	km
Mars gravitational constant	μ	42828	km^3/s^2
Sutton-Graves constant	k	1.9027 x 10^{-5}	kg$^{1/2}$·km/cm^2
Nose radius	r_n	1	m
Vehicle mass	m	800	kg
Aerodynamic reference area	S	19	m^2
Drag polar parameter	n	1.75	—
Maximum *L/D*	E^*	3.5	—
Lift coefficient at maximum *L/D*	C_L^*	0.08	—
Initial, final radius	r_0, r_f	3560	km
Mars arrival hyperbolic excess velocity, and entry speed	$[V_\infty^-, V_0]$	[6.204, 7.909]	km/s
Mars departure hyperbolic excess velocity, and exit speed	$[V_\infty^+, V_f]$	[4.565, 6.701]	km/s
Hyperbolic turn angle	δ_d	72.6	deg

Solving the TPBVP with the parameters given above yields a minimal convective heat load of 27.7 kJ/cm^2, and a peak stagnation point convective heating rate of 88.8 W/cm^2. The corresponding radiative heat load, not necessarily minimal, is 1.67 kJ/cm^2 with a peak radiative heating rate of 7.00 W/cm^2. In terms of maximums, the peak total heat flux is 95.9 W/cm^2 and the total heat load is approximately 29.4 kJ/cm^2. Figure 3.14 – Figure 3.18 contain the optimal altitude, velocity, flight-path angle, L/D, and heating rate, both convective and radiative, profiles of the Mars atmospheric flythrough.

The vehicle enters the atmosphere with an entry flight-path angle of -13.3 degrees, and increases until approximately two minutes in when the vehicle appears to level off. The vehicle does not truly become level, but rather the flight-path angle steadily increases slowly, keeping a negative value, meaning a slow decrease in altitude. As a result, the vehicle progressively loses speed and the *L/D* increases until about six minutes into the maneuver when the vehicle starts its ascent out of the atmosphere. Interestingly, the L/D of the vehicle never reaches its maximum value of E* meaning that in a practical sense the vehicle has room to correct for unknown variations in the atmosphere or aerodynamic coefficients.

Comparing the peak heating rates and total heat load for this particular AGA

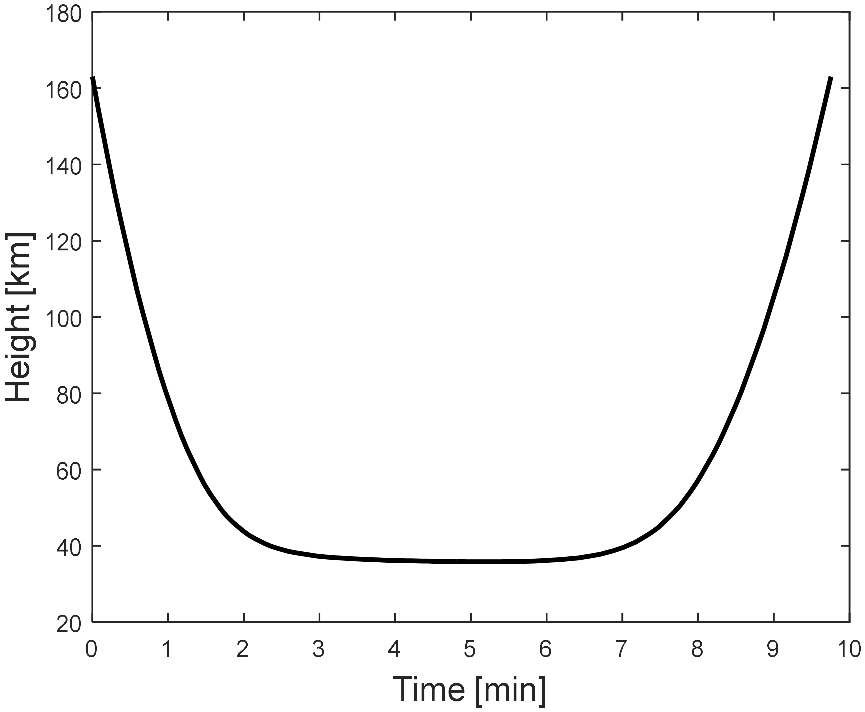

Figure 3.14: Altitude versus time plot showing a nearly symmetrical descent and ascent, with holding a fairly constant altitude of ~35 km between minutes 3 and 7.

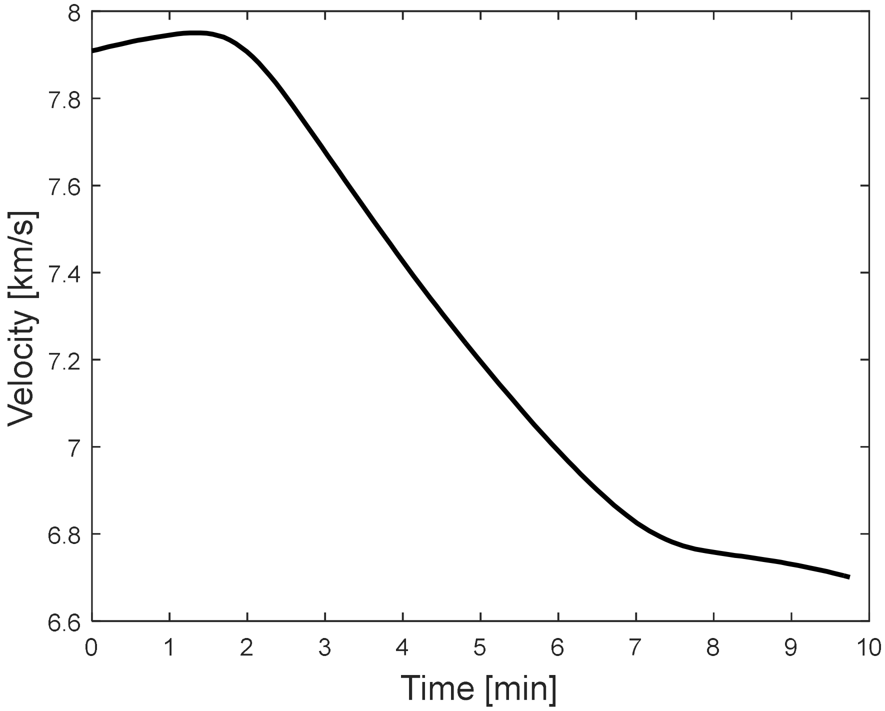

Figure 3.15: Velocity versus time plot showing a steady loss of speed during the period where the vehicle is deepest in the atmosphere.

mission, the type of TPS material and the amount needed is within current or near-future material technologies. In the NASA report on technologies for extreme environments [43], a peak heat flux of 95.9 W/cm^2 is under the maximum allowed heat flux created for the TPS materials on the Mars Pathfinder, and Mars Science Laboratory missions.

The material used was SLA 561 V, with peak heat fluxes of 106 and 155 W/cm^2 respectively for the two missions. The total heat load, which determines the mass fraction of TPS material required on a vehicle, requires about 1.5 times more material than what was used on Apollo capsules upon reentry. Using a fitted curve from historical data relating heat load to the TPS mass fraction, the approximate amount of TPS required for the AGA mission, excluding Earth reentry, is 18.3% [43].

One way to quantitatively measure the TPS mass fraction is to compare it to the amount of propellant required to get the same effect from a powered flyby at Mars. In order to increase the hyperbolic turn angle and reduce the outgoing V_∞ at Mars from a powered flyby, a burn is made at the distance of closest approach assumed to be at the edge of the atmosphere at 163 km. The ΔV required is found from the vis viva equation, and the propellant mass fraction is calculated from the well-known Tsiolkovsky rocket equation giving a mass fraction of 29.7%. The 11.4% difference in mass fraction can be used for additional science instruments, probes, or payload, while also highlighting the amounts in mass savings from using AGA over traditional GA and additional burn maneuvers.

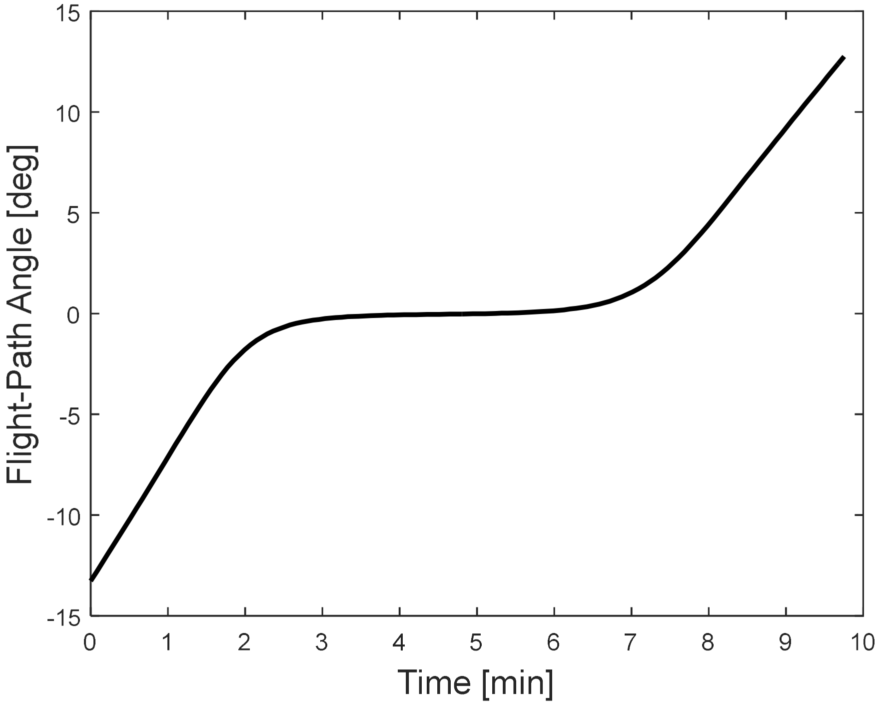

Figure 3.16: Flight-path angle versus time plot depicting the descent, then leveling out between minutes 3 and 7, before starting the ascent.

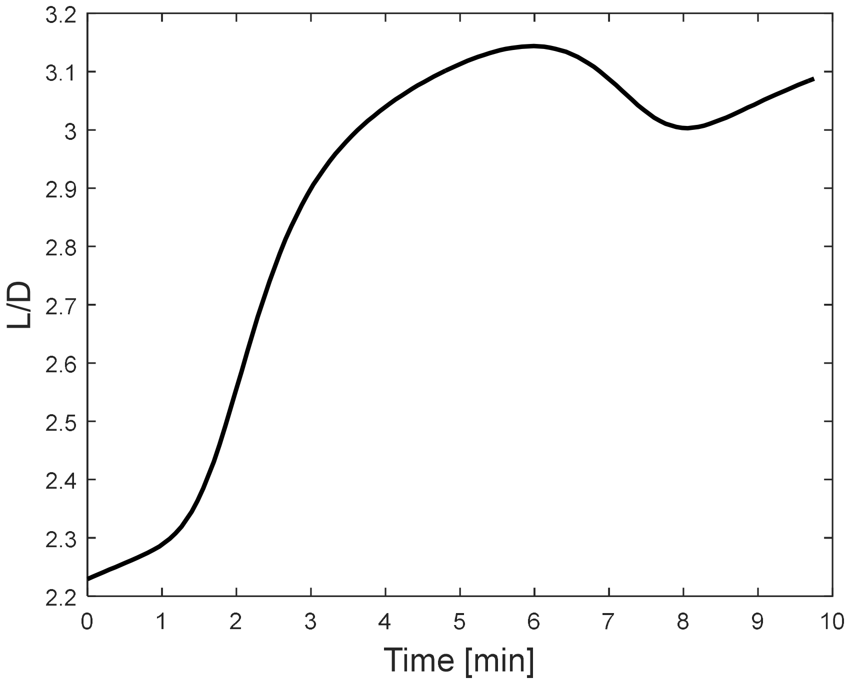

Figure 3.17: L/D versus time showing a steady increase in control authority until the vehicle begins ascending out of the atmosphere, where the L/D is kept at a high value, but never reaches the maximum of 3.5.

A method for optimizing AGA trajectories based on minimizing the total convective heat load has been developed. Desired interplanetary trajectories are found with STOUR-AGA, approximating the AGA maneuver with an analytical solution. The incoming and outgoing V_∞ vectors at the AGA body are used to get the physical boundary conditions for the optimal control problem. The AGA maneuver is optimized with a given vehicle characterized by its mass and aerodynamic properties.

With a carefully chosen interplanetary mission it may be possible to fly an AGA trajectory with already proven technology. It is shown that TPS materials exist that can withstand the peak heat flux, one of the two mission critical technologies required for AGA. The other critical technology is the high *L/D* capability which is still in the early stages of development.

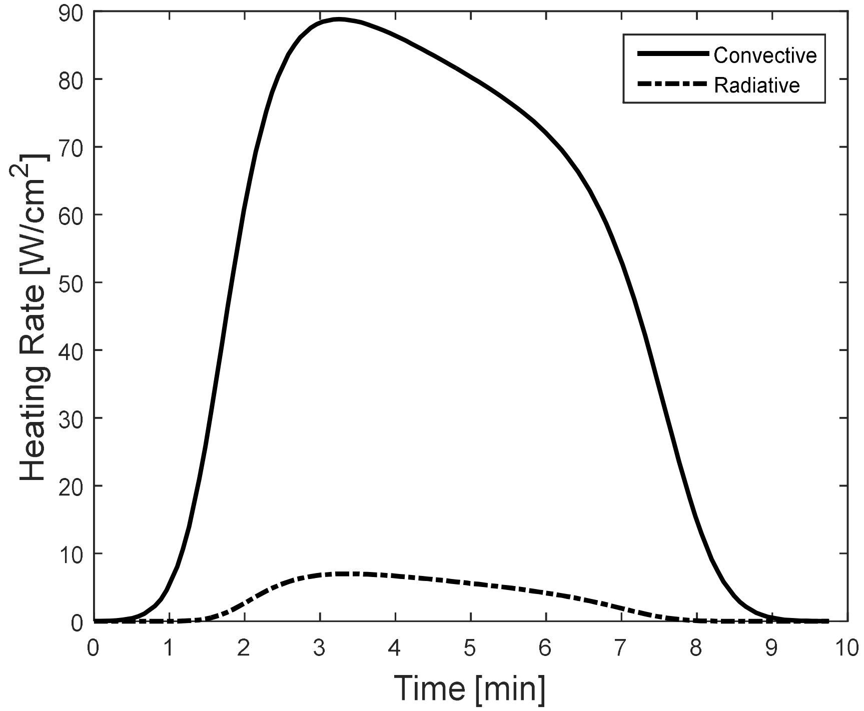

Figure 3.18: Convective and radiative heating rates versus time, with the peak heating rates occurring when the flight-path angle begins to level out at ~3 minutes.

CHAPTER 4. AGA GUIDANCE ALGORITHM

Apart from the hard technology requirements of a high L/D vehicle at hypersonic speeds and the thermal protection system to withstand high heat-loads, AGA can only become realizable with a robust guidance scheme able to guide the vehicle from atmospheric entry to exit, subject to model dispersions. The guidance algorithm outlined here uses angle-of-attack guidance through directly controlling the lift coefficient by means of pitching. A predictor-corrector provides continual new updates for a reference trajectory that the vehicle will attempt to follow by means of radius (or altitude) tracking.

The algorithm is divided into three phases: an entry phase where it follows an on-board pre-computed reference path to an altitude where the vehicle is able to perform steady-level flight. The second phase is the cruise phase where the vehicle maintains a constant altitude until a calculated exit time, continuously updated by the predictor-corrector. Once the exit time is reached the vehicle enters the last phase, the exit phase, and tracks the last radius profile the predictor-corrector produced to atmospheric exit.

The final metric the guidance algorithm attempts to minimize is the corrective ΔV_∞ to get back on the nominal interplanetary trajectory to the next target in the AGA tour. Since corrective maneuvers are often made days after a planetary encounter, the metric ΔV_∞ is used instead of the usual ΔV in the heliocentric frame, and they have relatively the same meaning. The model is subject to dispersions in both atmospheric density as well as variations in the initial conditions at atmospheric entrance. The aerodynamic uncertainties (e.g. C_L, C_D, S) are not modeled in this investigation and the measured states from the IMU are assumed to be known perfectly.

One of the major issues being addressed in the AGA guidance algorithm is that AGA requires precise targeting of a final vector with both direction and magnitude. A similar guidance problem to AGA is one tailored to aerocapture, however the end-goals of aerocapture are different. In the aerocapture problem, the final orbit size (captured orbit period) is targeted; however orientation characteristics are usually not as much of a concern. If orientation is taken into account as in AGA, the distance traveled through the atmosphere is limited to some angle between the incoming and outgoing V_∞ vectors. Exiting the atmosphere too soon or too late leads to large, typically infeasible corrective burns. In addition, large dispersions in atmospheric density can necessitate design changes in the nominal entry flight-path angle from aerocapture missions. Entering at a nominal flight-path angle with a 50% thinner atmosphere than predicted may prevent the vehicle from attaining the required lift to reach the exit conditions, as the centripetal acceleration would be too overpowering. To address this issue, the entry flight-path angle is biased such that the guidance algorithm can handle $\pm 3\sigma$ variations in atmospheric density.

A literature search revealed that only one conference paper has addressed the AGA guidance problem subject to model dispersions. Casoliva et al. [32] uses bank angle modulation to control the vehicle with an additional terminal phase to offset unwanted out-of-plane effects. Lyons et al. [30] uses angle-of-attack to guide the AGA vehicle and was able to specify an entry corridor in terms of flight-path angle, but no model dispersions were incorporated. One peer-reviewed article [44] provided a flight-path angle guidance law to guide the vehicle from atmospheric entrance to exit for a variety of boundary conditions, but model dispersions were also not taken into account. The lack of published work in AGA guidance indicates there is much room for fundemental analysis of this problem.

4.1 Radius Tracking

The equations of motion used in the AGA guidance scheme are from Vinh [26] for a spherical planet with non-rotational atmosphere:

$$\begin{aligned} \dot{r} &= V \sin\gamma \\ \dot{\theta} &= \frac{V\cos\gamma}{r} \\ \dot{V} &= -\frac{D}{m} - \frac{\mu}{r^2}\sin\gamma \\ \dot{\gamma} &= \frac{L}{mV}\cos\sigma - \left(\frac{\mu}{r^2 V} - \frac{V}{r}\right)\cos\gamma \end{aligned} \tag{4.1}$$

where planar motion is assumed. The algorithm revolves around tracking a reference radius profile from atmospheric entry to exit. A numerical predictor-corrector, described in section 4.3.1.1, updates the reference radius profile every user-input guidance cycle t_G. Using the same notation for the variables and constants as section 3.4, the radius tracking law is designed with feedback linearization to achieve second-order linear radius error dynamics of the form:

$$\left(\ddot{r} - \ddot{r}_{ref}\right) + 2\zeta\omega_n\left(\dot{r} - \dot{r}_{ref}\right) + \omega_n^2\left(r - r_{ref}\right) = 0 \tag{4.2}$$

where ζ and ω_n are damping and natural frequency gains tuned for the specific guided trajectory, and the subscript *ref* denotes the radius and its derivatives of the reference radius profile. Due to the sensitive nature of AGA, trajectories with varying incoming and outgoing V_∞ vectors will need to have ζ and ω_n tuned manually to achieve good performance.

The radius tracking law needs at a minimum of two time-derivatives in order to work due to the fact that an explicit control parameter to satisfy equation (4.2) only appears in $\ddot{r}$:

$$\dot{r} = \dot{r}\left(V,\gamma\right), \qquad \ddot{r} = \ddot{r}\left(r,V,\gamma,\bar{C}_L\right) \tag{4.3}$$

Attempting to solve equation (4.2) explicitly for $\bar{C}_L$, after substituting in equation (4.3), leads to a transcendental equation:

$$\begin{aligned}&\left(nE^*\bar{C}_L\cos\sigma - \left|\bar{C}_L\right|^n\tan\gamma\right)\frac{\rho V^2 S\cos\gamma}{2mnE^*} = \frac{\sin^2\gamma}{r^2} + \left(\frac{1}{r^2}-\frac{V^2}{r}\right)\cos^2\gamma\\&+\ddot{r}_{ref} - 2\zeta\omega_n\left(V\sin\gamma - \dot{r}_{ref}\right) - \omega_n^2\left(r-r_{ref}\right) + \left(n-1\right)\tan\gamma\end{aligned} \tag{4.4}$$

It has been experimentally discovered that a solution always exists when solving equation (4.4) using Newton's method, as long as the vehicle is "nearby" the reference trajectory. It is difficult to quantify how "nearby" the vehicle must be since the tracking equation has three dimensions in $\bar{r}$, $\bar{v}$, and γ, however the root-solver has not diverged for any guided cases in the present work. Every second throughout the guided flythrough, IMU measurements are taken and a new control is solved and fed back into the system model.

4.2 Vehicle Characteristics

A vehicle loosely based on Casoliva et al. [32] with $E^* = 5$ is used for the guided trajectories in the current work, but with a more realistic value of $E^* = 3.5$. The vehicle is a waverider with pertinent characteristics listed in Table 4.1.

Table 4.1 Waverider vechicle characteristics

Parameter	Value
Mass m [kg]	800
Aerodynamic Reference Area S [m^2]	19
C_L^*	0.08
E^*	3.5
n	1.75

The lift and drag coefficients are described by the same equations in [32] with:

$$\begin{aligned} C_L &= \operatorname{sgn}\left(\alpha + 5^\circ\right) 0.0076415 \left|\alpha + 5^\circ\right|^{1.25} \\ C_D &= C_{D0} + k_D \left|C_L\right|^n \end{aligned} \tag{4.5}$$

where α is the angle-of-attack. Equation (4.5) differs from [32] in the drag coefficient numbers for C_{D0} and k_D. They have been modified to fit the C_L^*, n, and E^* in the table above so that $C_{D0} = 0.00980$ and $k_D = 1.085$. The angle-of-attack when $(L/D)_{\max}$ occurs is approximately $\alpha = 1.5°$. The bounds on α are $-10° \le \alpha \le 25°$, corresponding to bounds on the control in the guidance algorithm, C_L to be $-0.057 \le C_L \le 0.54$. Furthermore, rates of change on angle-of-attack are limited to $-20 \le \dot{\alpha} \le 20$ deg/s and $-6.8 \le \ddot{\alpha} \le 6.8$ deg/s^2

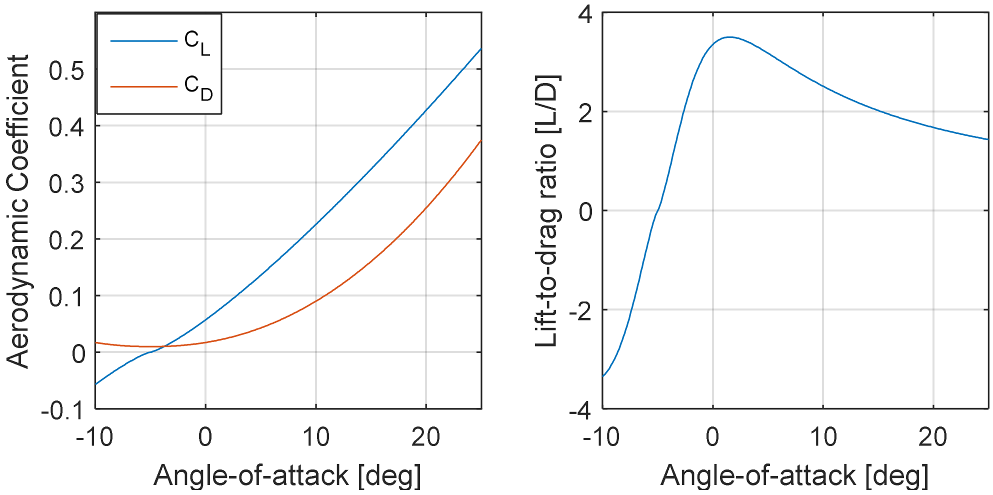

Figure 4.1: Aerodynamic coefficients and L/D for waverider vehicle.

giving rate limits on C_L of $-0.45 \le \dot{C}_L \le 0.45$ s^{-1} and $-0.15 \le \ddot{C}_L \le 0.15$ s^{-2}. The limits on the rates are found by taking time-derivatives of the first of equations (4.5) and using parameter optimization software to find the global maximum and minimum, as the resulting equations are nonlinear with bounds on the variables. The rate limiting is enforced on C_L using backwards differencing during every control update.

4.3 Guidance Algorithm Phases

The guidance algorithm is divided up into three stages: entry, cruise, and exit (see Figure 4.2). During the entry phase, the vehicle tracks a radius profile given by the solution to the optimal control problem in section 0 to a specified altitude such that steady-level flight can be achieved. This specific radius profile is chosen to minimize the heat-rate the vehicle acquires during descent, as that is when heat-rate is highest. The entry flight-path angle is biased so that the guidance algorithm can handle atmospheric dispersions that could be 50% thinner than expected.

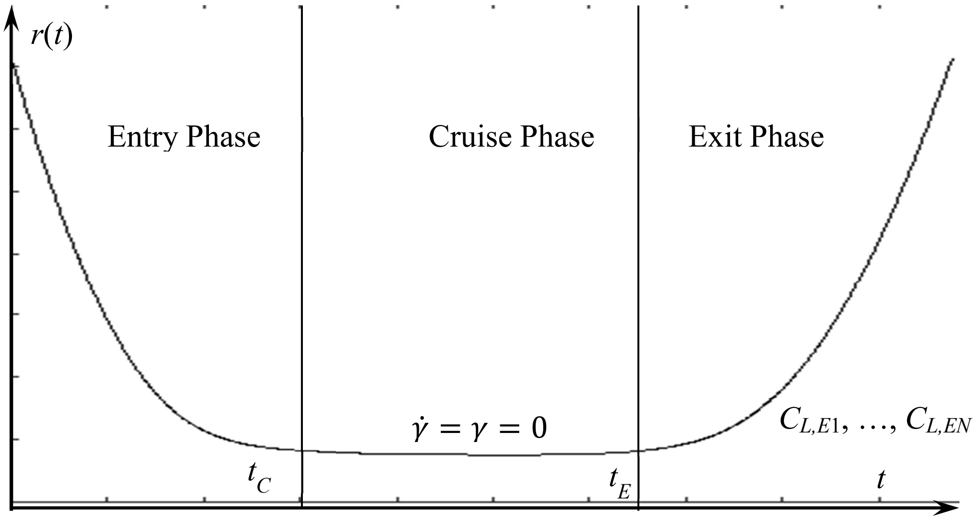

Figure 4.2: Three phases of AGA guidance Algorithm

Once an altitude where steady-level flight is possible, the vehicle enters the cruise phase at t_C and the predictor-corrector starts to update the reference radius profile every guidance cycle t_G. The predictor corrector solves a parameterized control problem getting an exit time t_E when the vehicle should end steady-level flight and the N parameterized controls at evenly spaced times between t_E and t_f, $C_{L,E1}$, …, $C_{L,EN}$, during the exit phase that drive the vehicle to the desired exit state. Once t_E is reached, the vehicle tracks the last reference profile calculated from the predictor-corrector to atmospheric exit.

4.3.1 Entry/Cruise Phase

The entry phase tracks a nominal reference radius profile that is found by solving the optimal control problem that gives the minimum accrued total heat load. However the nominal profile must have an entry flight-path angle that is steep enough to be able to handle up to a 50% thinner atmosphere than predicted. If the entry flight-path angle is too shallow with a thin atmosphere, a suitable altitude for steady-level flight will not be achievable, as the lift will not be able to overcome the centripetal acceleration. See Figure 4.3 for visualization of accelerations. Without being able to reach an altitude where

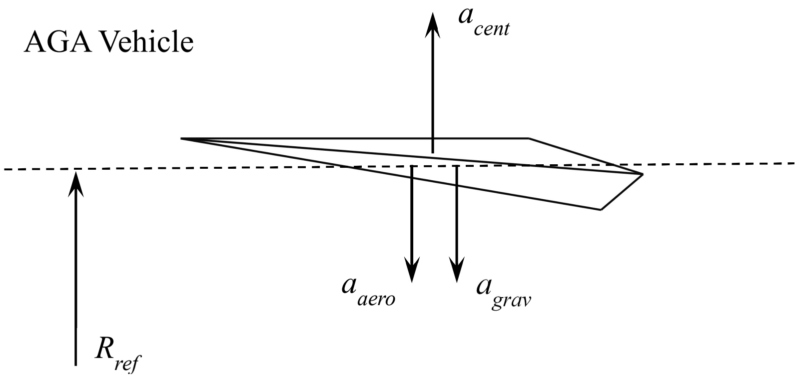

Figure 4.3: Acting accelerations during steady-level flight.

steady-level flight occurs, the vehicle will skip out of the atmosphere early, and recovery of the mission is likely not possible. Figure 4.4 illustrates the entry flight-path angle problem during an example Mars entry.

In the Figure 4.4, altitude profiles with the same entry flight-path angle for a -3σ, $+3\sigma$, and nominal atmospheric density conditions where 1σ is $\approx 15\%$ dispersion from the nominal are given. The lift vector of the vehicle in this case is constant and always pointing downwards towards the ground. The nominal case steadily approaches the reference altitude where steady-level flight can occur. The case with a $+3\sigma$ *thicker* atmospheric density approaches the reference altitude steeper, as the vehicle is taking advantage of more lift. With the thicker atmosphere, the vehicle has no problem reaching the reference altitude. When the atmosphere is *thinner* than expected, the vehicle *cannot* reach the reference altitude, as it is not able to generate enough lift to balance the gravitational and centripetal accelerations. Where the -3σ line ends is the lowest the vehicle can go under these conditions.

To address the entry-flight path angle problem, the reference entry radius profile used is the solution to the minimum heat-load problem with the -3σ density model assumed to be the nominal. In this way, the entry flight-path angle is steep enough to handle the entire range of assumed dispersions in atmospheric density.

Steady-level flight is achieved at an altitude where the gravitational, aerodynamic, and centripetal accelerations balance each other out. A depiction of the accelerations is in Figure 4.3, where the centripetal acceleration, a_{cent}, acts radially upward, and the aerodynamic lift acceleration, a_{aero}, and gravitational acceleration, a_{grav}, balance it in the opposite direction. The reference altitude is calculated by the acceleration balance via:

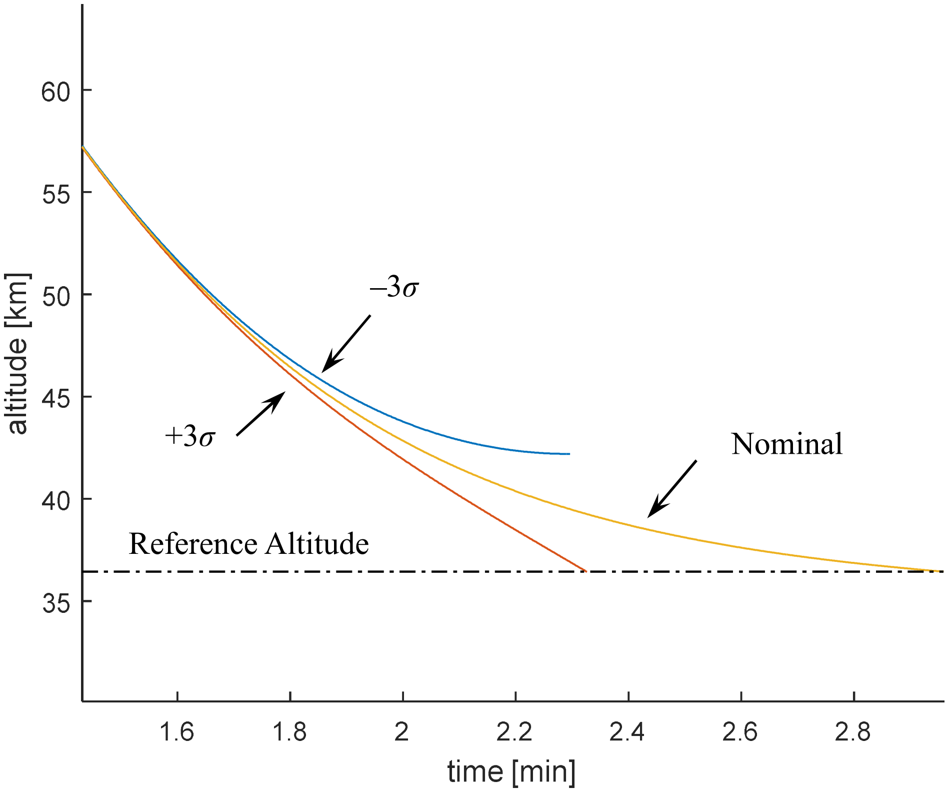

Figure 4.4: Altitude profiles for thinner, thicker, and nominal atmospheric density dispersions.

$$\frac{\rho V^2 S C_L}{2m} + \frac{\mu}{r^2} = \frac{V^2}{r} \tag{4.6}$$

where dimensional variables are being used. Once the vehicle reaches an altitude where steady-level flight can begin, the predictor-corrector starts updating the reference radius profile every guidance cycle.

The altitude where steady-level flight is possible (cruise altitude) depends on the central body's atmosphere and gravity, and the aerodynamic capabilities of the vehicle. A range of acceptable cruise altitudes are calculated by solving equation (4.6) for the radius using the chosen vehicle for the AGA maneuver. The reference radius profile is updated by the predictor-corrector at an altitude slightly above the maximum allowable predicted cruise altitude, denoted R_S. Starting the predictor-corrector above the range of predicted cruise altitudes ensures that the vehicle can approach the actual cruise altitude *from above*. The reason for approaching from above is to prevent too much energy dissipation upon entry, preventing the exit conditions from being reached. Approaching the cruise altitude *from below* by means of overshooting may cause too much drag, making it impossible to achieve the exit conditions. A visualization of the two different approaches to the cruise altitude is in Figure 4.5. For example, at Mars, for the vehicle described above, the altitude where the predictor-corrector starts is approximately 40 km above the surface. As indicated by equation (4.2), an approach from above has a higher chance of occuring for values of $\zeta \geq 1$ making the system critically damped or over-damped. From trial and error, the results of this guidance algorithm were better for the over-damped case than critically damped, thus values used for ζ are kept strictly greater than one.

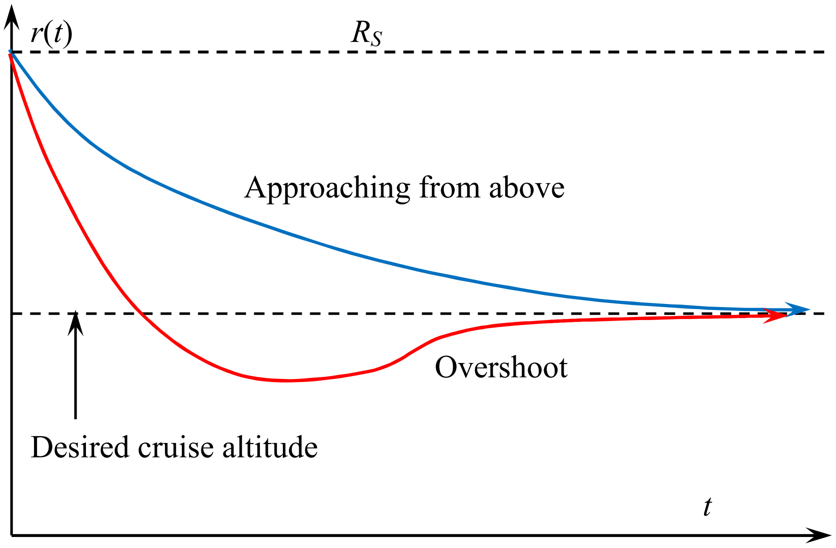

Figure 4.5: Visualization of approaching the desired cruise altitude.

4.3.1.1 Predictor-Corrector

The numerical predictor-corrector used in the guidance scheme updates the reference radius profile that guides the vehicle to the desired exit state. The algorithm starts at the beginning of the cruise phase at t_C and updates the reference profile every guidance cycle t_G until the predicted exit time t_E is reached. At t_E the vehicle ends steady-level flight and begins its ascent until atmospheric exit.

The reference radius profile is constructed by solving a parameterized targeting problem to get to the desired outgoing V_∞ vector. The targeting problem is summarized as follows:

$$\begin{aligned}
&\text{Find}: t_E, t_f, \theta_f, \gamma_f, C_{L,E1}, \ldots, C_{L,EN} \\
&\text{such that}: \\
&r\left(t_f\right) = r_f, V\left(t_f\right) = V_f, \delta\left(t_f\right) = \delta_d \\
&\text{with cruise condition}: \\
&\dot{\gamma} = \gamma = 0 \quad \forall \quad t \in \left[t_C, t_E\right]
\end{aligned} \tag{4.7}$$

In equation (4.7), t_f, θ_f, and γ_f are the unknown final time and end states that are solved at every guidance cycle. The final velocity V_f and final hyperbolic turn angle δ_f are functions of the beginning and end states given by:

$$
\begin{aligned}
&V_f = \sqrt{V_\infty^{+} + \frac{2\mu}{r_f}} \\
&\delta_f = \theta_f - \pi + \cos^{-1}\left\{ -\left[1 + \frac{\left(V_0^2 - 2\mu/r_0\right) r_0^2 V_0^2 \cos^2\gamma_0}{\mu^2} \right]^{-1/2} \right\} \\
&+\cos^{-1}\left\{ -\left[1 + \frac{\left(V_f^2 - 2\mu/r_f\right) r_f^2 V_f^2 \cos^2\gamma_f}{\mu^2} \right]^{-1/2} \right\} \\
&-\cos^{-1}\left[\frac{r_0 V_0^2 \cos^2\gamma_0 - \mu}{\sqrt{\mu^2 + \left(V_0^2 - 2\mu/r_0\right) r_0^2 V_0^2 \cos^2\gamma_0}} \right] \\
&-\cos^{-1}\left[\frac{r_f V_f^2 \cos^2\gamma_f - \mu}{\sqrt{\mu^2 + \left(V_f^2 - 2\mu/r_f\right) r_f^2 V_f^2 \cos^2\gamma_f}} \right]
\end{aligned}
\tag{4.8}
$$

Additionally there are a pre-specified N number of parameterized control values $C_{L,E1}$, …, $C_{L,EN}$ that are also determined by the predictor-corrector. The control values are spaced at N equally distant points between t_E and t_f. Often one parameterized control does not give enough control authority to achieve the desired exit conditions. With the higher value for N comes the issue of dimensionality along with convergence issues; however for all guided cases in the current work, a value of $N = 2$ has been sufficient. During the cruise phase, the control law is specified by setting $\dot{\gamma}$ in equation (4.1) to zero and solving for C_L:

$$
C_L = \frac{2m}{\rho V^2 S}\left(\frac{\mu}{r^2} - \frac{V^2}{r}\right)\frac{\cos\gamma}{\cos\sigma} \qquad t \in \left[t_C, t_E\right] \tag{4.9}
$$

The predictor-corrector is performed by setting up a multiple shooting algorithm between different boundaries with $N = 2$. The first boundary is the cruise phase between t_C and t_E, the second boundary is halfway between t_E and t_f (denoted t_1), and the final boundary is at t_f. Additionally, in order to minimize the number of constraints, the predictor-corrector is solved using both forward and backwards propagation. At every guidance cycle, the predictor-corrector starts by propagating forward from the current time, $t \in \left[t_C, t_E\right]$ to t_E, then again propagates forward again to t_1. Lastly, propagation is performed from the desired end-states backwards from t_f to t_1. A corrections process then takes place, updating the initial estimate of the design variables and matching the states at the boundaries until the l^2 norm of the constraint vector is less than 10^{-12}.

The design variable vector for the predictor-corrector is:

$$\boldsymbol{X} = \begin{bmatrix} t_E & r_E & \theta_E & V_E & \gamma_E & C_{L,E1} & t_f & \theta_f & \gamma_f & C_{L,E2} \end{bmatrix}^T \tag{4.10}$$

While the constraint vector takes the form:

$$\boldsymbol{F}\left(\boldsymbol{X}\right) = \begin{bmatrix} r_C^f - r_E\left(t_E\right) \\ \theta_C^f - \theta_E\left(t_E\right) \\ V_C^f - V_E\left(t_E\right) \\ \gamma_C^f - \gamma_E\left(t_E\right) \\ r_E^f - r_2^0 \\ \theta_E^f - \theta_2^0 \\ V_E^f - V_2^0 \\ \gamma_E^f - \gamma_2^0 \\ \delta\left(t_f\right) - \delta_d \end{bmatrix} \tag{4.11}$$

The superscripts *f*, 0 in equation (4.11) indicate the corresponding state evaluated at the final forwards propagated time and final backwards propagated time respectively. The subscript *E* refers to the exit time t_E, and the subscript 2 refers to the backwards propagated leg. The Jacobian matrix for the above system is:

$$DF(\boldsymbol{X})=\begin{bmatrix} \dfrac{\partial \boldsymbol{x}_C}{\partial t_E} & -\mathbf{I} & 0 & 0 & 0 & 0 & 0 \\ \dfrac{\partial \boldsymbol{x}_E^f}{\partial t_E}-\dfrac{\partial \boldsymbol{x}_2^0}{\partial t_E} & \Phi(t_1,t_E) & \dfrac{\partial \boldsymbol{x}_E}{\partial C_{L,E1}} & \dfrac{\partial \boldsymbol{x}_E^f}{\partial t_f}-\dfrac{\partial \boldsymbol{x}_2^0}{\partial t_f} & -\dfrac{\partial \boldsymbol{x}_2^f}{\partial \theta_f} & -\dfrac{\partial \boldsymbol{x}_2^f}{\partial \gamma_f} & -\dfrac{\partial \boldsymbol{x}_2}{\partial C_{L,E2}} \\ 0 & 0 & 0 & 0 & \dfrac{\partial \delta_f}{\partial \theta_f} & \dfrac{\partial \delta_f}{\partial \gamma_f} & 0 \end{bmatrix} \tag{4.12}$$

The size of the Jacobian given in equation (4.12) is 9 by 10. Since the number of design variables in greater than the number of constraints, the update on the design variable vector $\boldsymbol{X}$ is done using equation (2.31), meaning the update is not unique and the converged solution is a “best fit” to the initial estimate. The initial estimate for $\boldsymbol{X}$ when the guidance algorithm begins the cruise phase is based on the reference profile used in the cruise phase. At every guidance cycle thereafter, the initial estimate is the converged solution from the previous iteration.

4.3.2 Exit Phase

The exit phase of the guidance algorithm follows the last reference radius profile found from the predictor-corrector to atmospheric exit when the vehicle reaches the predicted exit time t_E. At this point the vehicle is ascending out of the atmosphere where atmospheric density is low, limiting the amount of control authority the lift vector has on

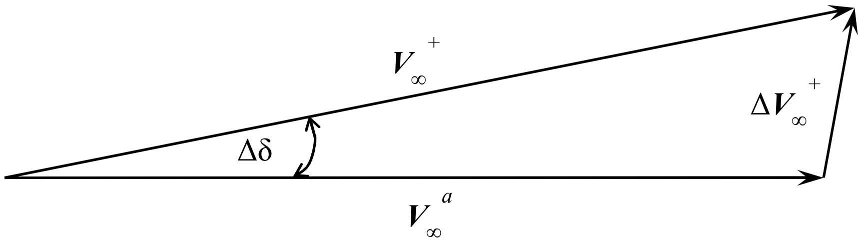

Figure 4.6: Required clean-up in $\boldsymbol{V}_\infty^+$ after AGA guidance.

the system dynamics. Upon atmospheric exit, the vehicle will leave the gravitational influence of the central body and perform any necessary clean-up burns required to get back on the nominal interplanetary trajectory. The clean-up burn metric is measured as the change in the desired $\boldsymbol{V}_\infty^+$ (denoted $\Delta\boldsymbol{V}_\infty^+$) to get back on the nominal interplanetary trajectory. A diagram of the clean-up maneuver is depicted in Figure 4.6 where the superscript *a* stand for the actual value attained post-guidance and the difference in the hyperbolic turn angle is $\Delta\delta = \delta_d - \delta_a$. The value for the clean-up ΔV_∞^+ is derived from the law of cosines with:

$$\Delta V_\infty^+ = \sqrt{\left(V_\infty^a\right)^2 + \left(V_\infty^+\right)^2 - 2\left(V_\infty^a\right)\left(V_\infty^+\right)\cos\Delta\delta} \qquad (4.13)$$

4.4 Modeled Dispersions and Assumptions

The guidance algorithm simulates a Mars AGA that is subject to model dispersions in atmospheric density and initial conditions. Aerodynamic or IMU dispersions are not modeled in the current analysis. The interplanetary trajectory is the same found in section 0 with a Mars encounter date of August 21, 2022 and arrival V_∞ of 6.2 km/s. The target outgoing V_∞ is 4.6 km/s with a total hyperbolic turn angle of 72.6°. All pertinent vehicle characteristics, physical parameters, initial conditions, dispersions, and control gains are available in Table 4.2.

A ±3σ dispersion in an exponentially modeled atmospheric density is assumed with a nominal reference density of 0.02 kg/m^3 at the planet's surface. The dispersions in initial height, entry velocity, and initial flight-path angle are uniform with bounds set to ±800 m, ±6 m/s, and ±0.45° respectively. These bounds are the limits of convergence for the predictor-corrector. One limitation to how this guidance scheme is set up is that if convergence fails, most likely due to the fact too much energy has been lost from drag to reach the desired exit conditions, then the vehicle is considered “lost” and the algorithm fails. Possible methods to overcome this issue and open up the solution space are addressed in the Future Work section.

Table 4.2 Constants, initial conditions, vehicle parameters, and gains

Parameter	Symbol	Value	Units
Vehicle mass	m	800	kg
Reference area	S	19	m^2
Drag polar exponent	n	1.75	—
Reference density	ρ_0	0.02	kg/m^3
Inverse scale-height	β	1/7.1	km^{-1}
Height of atmosphere	h_{atm}	163	km
Planet radius	R_0	3397	km
Arrival hyperbolic excess speed	V_∞^-	6.2	km/s
Departure hyperbolic excess speed	V_∞^+	4.6	km/s
Hyperbolic turn angle	δ	72.6	deg
Initial nominal radius	r_0	3560	km
Initial nominal entry speed	V_0	7.9	km/s
Initial nominal flight-path angle	γ_0	-13.85	deg
Dispersion in initial radius from nominal	Δr_0	±800	m
Dispersion in initial entry speed from nominal	ΔV_0	±6	m/s
Dispersion in initial flight-path angle from nominal	$\Delta \gamma_0$	±0.45	deg
Dispersion in atmospheric density	$\Delta \rho_0$	$\pm 3\sigma$	kg/m^3
Natural frequency gain	ω_n	0.1	s^{-1}
Damping gain	ζ	2	—

Computed from an accelerometer on the vehicle measuring the drag force, the air density is assumed to be measurable with the following accuracy:

$$\rho_m = \begin{cases} \mathrm{N}\left(\rho_a, 0.5\rho_a\right) & h > 65\,\mathrm{km} \\ \mathrm{N}\left(\rho_a, 0.15\rho_a\right) & h \le 65\,\mathrm{km} \end{cases} \tag{4.14}$$

where ρ_m is the measured density, and $\mathrm{N}(a, \sigma)$ is a Gaussian distribution of mean a, and standard deviation σ. Above an altitude of 65 km, the drag force is assumed to have a

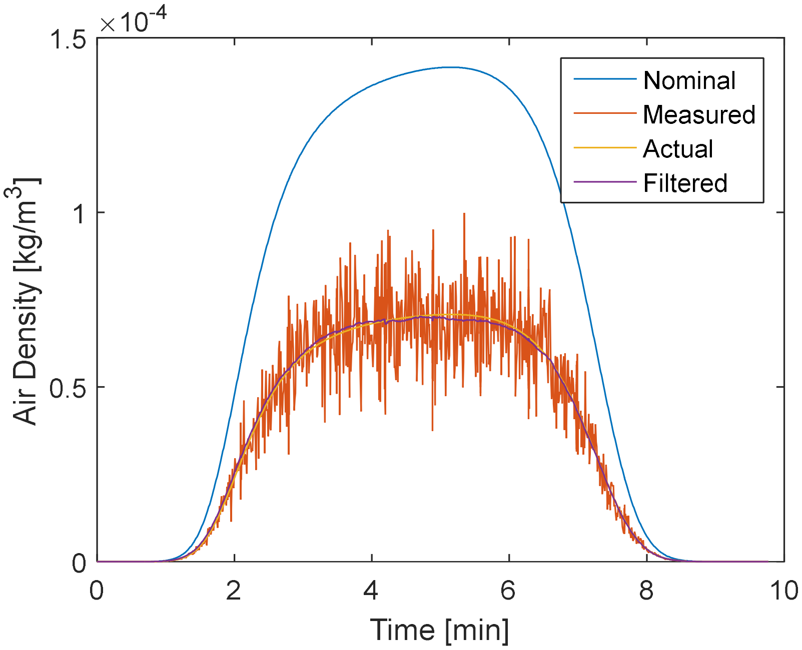

Figure 4.7: Nominal, measured, actual, and filtered air densities for a guided case with 50% thinner atmosphere.

higher degree of error, as the atmosphere is much thinner. Due to the error in the air density measurements a low-fidelity first-order fading-memory filter is used for better accuracy. The reason for using a low-fidelity filter is to emphasize that this algorithm is robust enough to work without sophisticated statistical techniques.

Let the ratio between the measured and nominal air density be $\kappa = \rho_m / \rho_n$ where ρ_n is the nominal density. The fading-memory filter is updated with every measurement via:

$$\begin{aligned} &\kappa_{n+1} = \kappa_n + (1-\xi)(\kappa - \kappa_n) \\ &\kappa_0 = 1, \quad 0 < \xi < 1 \end{aligned} \tag{4.15}$$

with filter coefficient $\xi = 0.95$. An example output for the nominal, actual, measured, and filtered air densities for a 50% thinner atmosphere than predicted (nominal) is in Figure 4.7. The nominal (blue) line represents an exponential atmospheric density model with reference density 0.02 kg/m^3. The measured air density (red) from drag deceleration samples is erratic and noisy. Actual air density (yellow) and filtered (purple) are close to each other, representing what is actually being fed into the system model, and what the algorithm predicts is being fed, respectively.

4.5 Monte Carlo Results and Analysis

A Monte-Carlo simulation of guided AGA around Mars for 2000 dispersed cases is performed with the parameters and assumptions discussed above. Figure 4.8 gives the clean-up ΔV_∞^+ metric required (color bar) with the corresponding errors in hyperbolic turn-angle δ (horizontal axis), and V_∞^+ magnitude (vertical axis). A histogram of how many cases lie within ~4 m/s between each other is in Figure 4.9.

Approximately 50% (1000) of the cases have less than a 4 m/s clean-up maneuver. The rest of the results display a nearly uniform distribution of clean-up ΔV_∞s with an overall average of 11.51 m/s and a maximum of 39.33 m/s. This distribution is most likely the result of the random variables used for the initial conditions being uniform.

There is no correlation between the clean-up ΔV_∞ and the dispersions in either entry radius r_0, or entry speed V_0. From Figure 4.8, the statistics appear to be one-sided which is due to the fact that the vehicle is always approaching the reference trajectory from above, and not from below. The algorithm is designed this way to ensure convergence of the predictor-corrector.

Looking into the dispersions and trajectories of the outliers in Figure 4.8, which are the few dots below the main streak, there is no reoccuring trend among them indicating that they truly are phenomena of the different parameters used and uncertainties inherant in the algorithm. Figure 4.10 plots the off-nominal entry flight-path angle versus the errors in final velocity, and shows a correlation with positive $\Delta\gamma_0$; a steeper flight-path angle entry is preferred when using this algorithm, as there is a smaller clean-up V_∞^+ magnitude. It is conjectured that the correlation is due to the bias in flight-path angle from assuming a -3σ atmosphere in the radius reference profile. Figure 4.11 shows the altitude profiles for all 2000 cases. The colors are mapped to gray-scale to

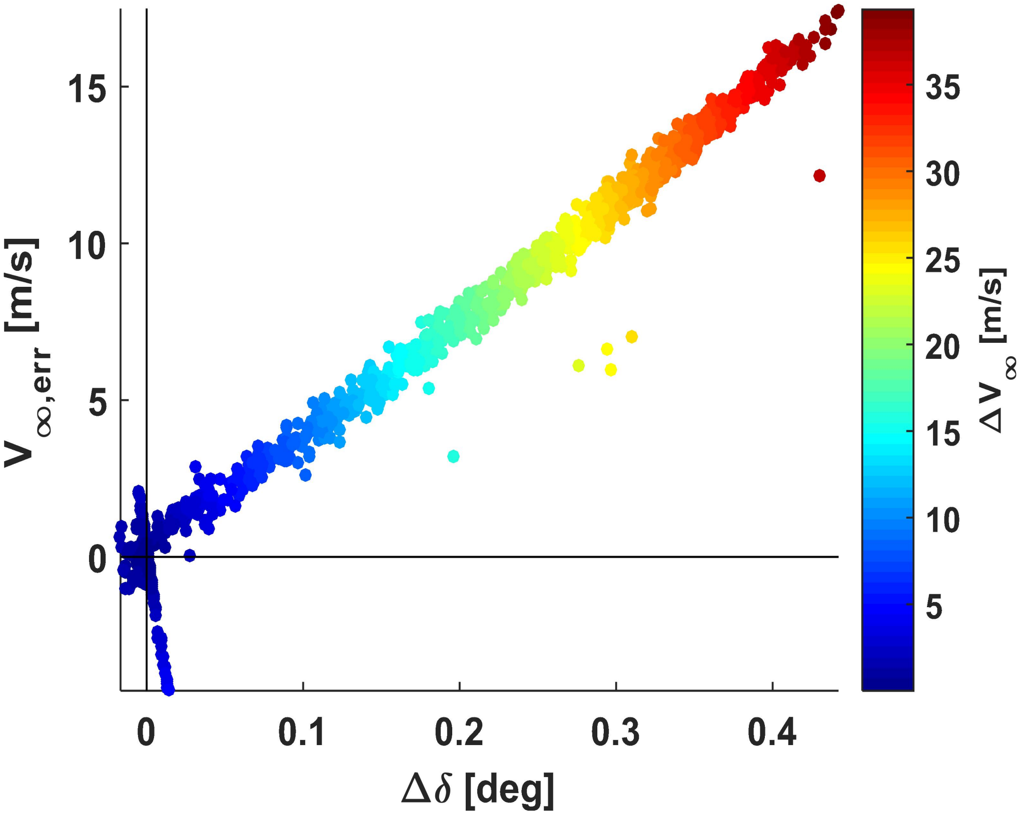

Figure 4.8: Monte Carlo results for Mars AGA guidance.

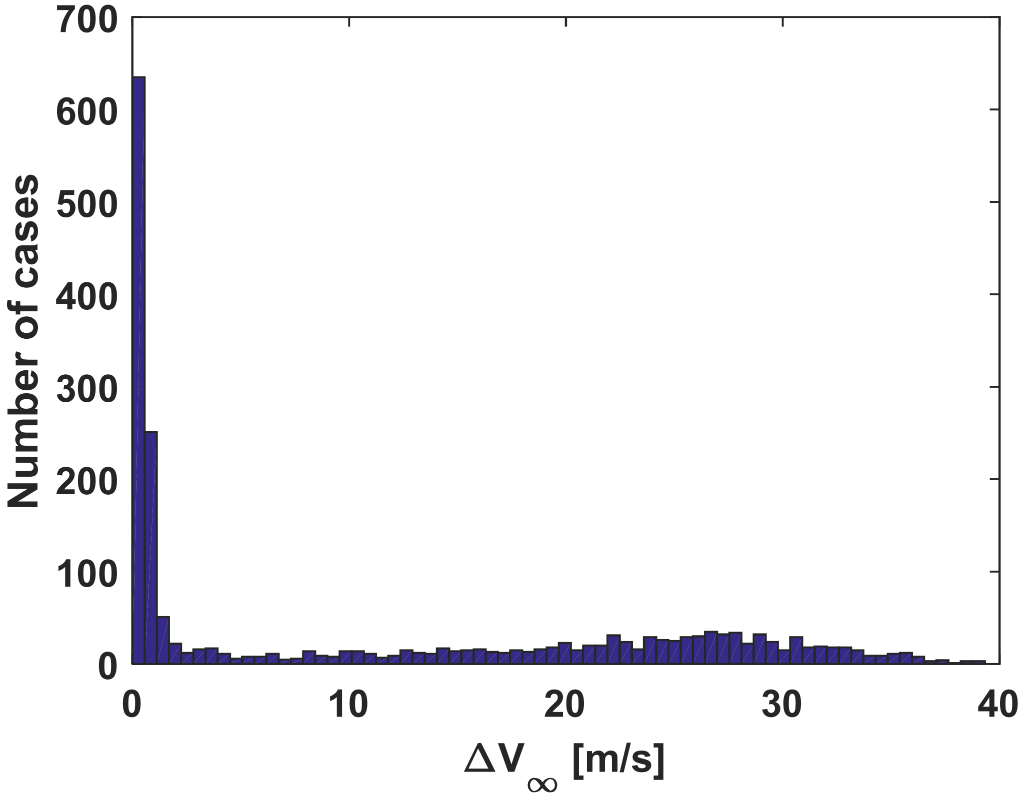

Figure 4.9: Histogram of clean-up ΔV_∞ for 2000 cases.

depict the darker the trajectory, the higher the clean-up ΔV_∞. There is a clear region of darker trajectories at the 2 minute mark, and these are trajectories that have both higher cruise altitudes and shallower entry flight-path angles. Higher cruise altitudes indicate that the atmosphere is thicker for these trajectories, thus for shallow entry flight-path angles, the guidance algorithm performs more poorly with thicker atmospheres.

The guidance algorithm presented here uses the lift coefficient as the control, changed by a means of pitching, and is subject to dispersions in atmospheric density and initial conditions. A predictor-corrector updates a reference radius profile every guidance cycle that the vehicle tracks until exiting the atmosphere. Through a Monte Carlo analysis, the algorithm robustly guides the vehicle to the desired exit V_∞^+ vector with a maximum

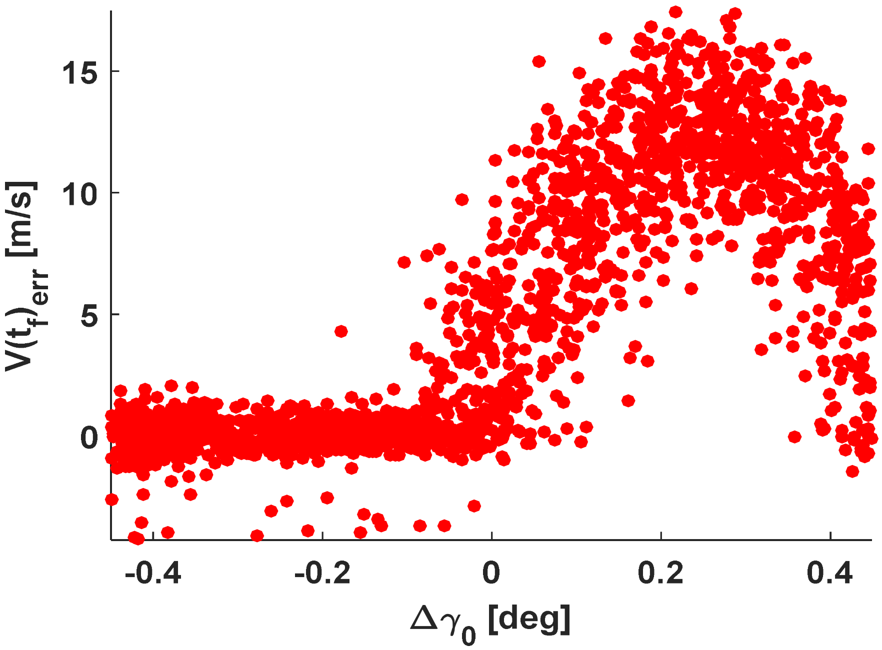

Figure 4.10: Correlation of change in initial FPA with final velocity error.

correction maneuver of 39.33 m/s. In reality the vehicle will be subject to aerodynamic and IMU uncertainties which are not modeled here, but are an issue requiring investigation in future work.

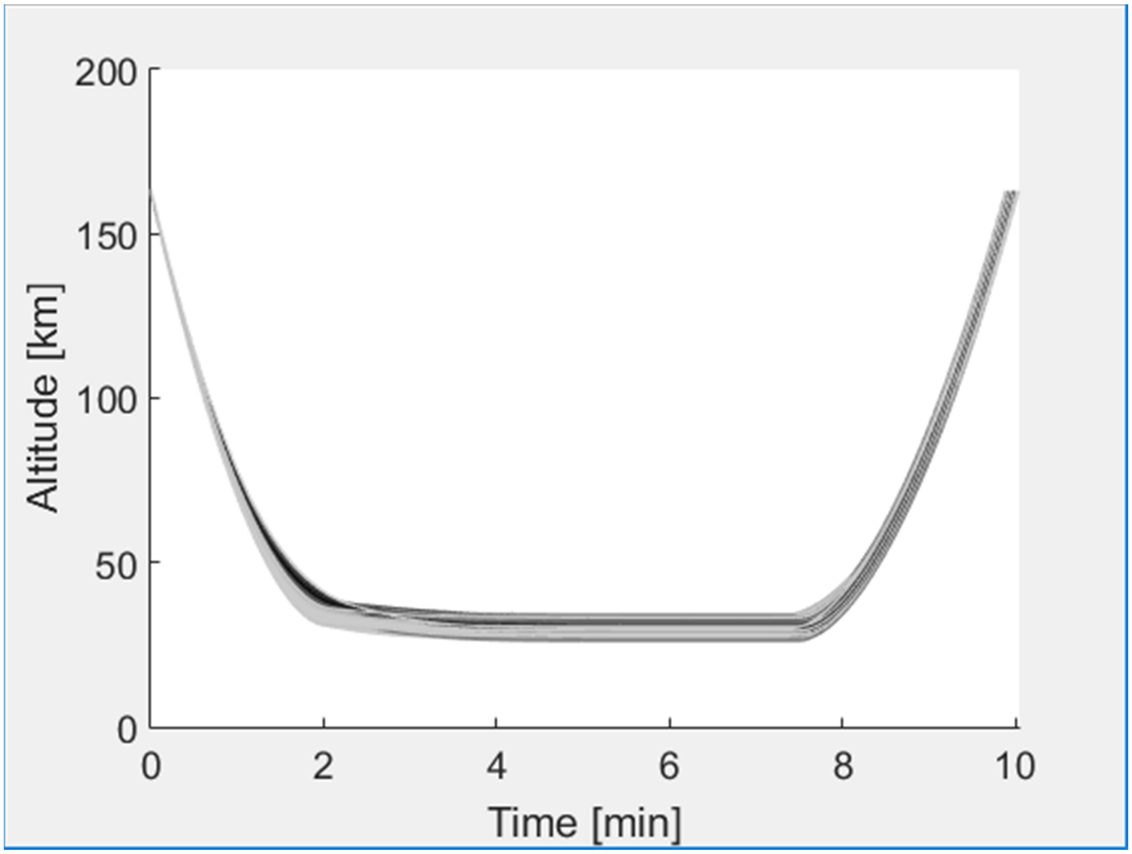

Figure 4.11: Altitude plots from Monte Carlo simulation.

CHAPTER 5. AEROCAPTURE TRAJECTORY OPTIMIZATION WITH ROTATING ATMOSPHERE

Aerocapture is another aeroassisted maneuver where a spacecraft approaching a central body on a hyperbolic trajectory uses the atmosphere to deplete the orbital energy to get into a captured elliptic orbit upon atmospheric exit. Recently JPL has developed interest in missions to the Ice Giants (Uranus and Neptune) and wants to investigate the potential advantages that aerocapture might offer at these planets [45].

The Ice Giants (as well as the Gas Giants, Jupiter and Saturn), are large and rotating at high rates with sidereal rotation periods of less than a 24 hours. Upon entering the atmosphere the rotational rate of the planets cannot be ignored when considering the velocity vector of the aerocapture flythrough. For example, around the equator of Uranus at an altitude of 1 bar atmospheric pressure the tangential speed of the atmosphere's rotation, assuming the entire atmosphere rotates at the same rate as the planet, is approximately 2.6 km/s. Thus the entirety of equations (3.1) – (3.6) must be taken into account to model aerocapture at these large planets.

One of the critical technologies to be able to realize aerocapture is the thermal protection system required to withstand the high heat-rates and heat-loads when travelling at hypersonic speeds through an atmosphere. The current work finds the optimal bank angle profile to guide an aerocapture vehicle to a desired capture orbit period using optimal control theory, while including the rotational rate of the atmosphere in the dynamic equations of motion. It turns out that due to the fast speeds of approach and the limited aerodynamic capabilities of an aerocapture vehicle, a suboptimal control of bank equal to zero, a full lift-up configuration, gives roughly the same result in total heat-load as the more complex optimal control with a much simpler implementation. The work presented here verifies that result.

5.1 Aerocapture Vehicle and Model Assumptions

The aerocapture vehicle is modeled at Uranus using the bank angle as the sole control variable and is flying at a trimmed angle of attack, corresponding to a constant (maximum) L/D. The atmospheric density is modeled exponentially via equation (3.8), but any model will suffice that is at least C^1 continuous for indirect methods. Table 5.1 includes all the constants and vehicle parameters used in the simulation. The aerodynamics are defined by the ballistic coefficient B, and the maximum lift-to-drag ratio E^*. The ballistic coefficient is defined by:

$$B = \frac{m}{SC_D} \tag{5.1}$$

Table 5.1: Vehicle parameters and constants in aerocapture simulation

Parameter	Symbol	Value	Units
Vehicle mass	m	1000	kg
Ballistic coefficient	B	250	kg/m^2
Nose radius	r_n	2	m
Lift-to-drag ratio	E^*	0.8	—
Sidereal rotation rate	Ω	1.0124e-4	rad/s
Inverse scale-height of atmosphere	β	1/27.7	km^{-1}
Reference density	ρ_0	0.42	kg/m^3
Radius of Uranus	R_0	25500	km
Height of atmosphere above 1 bar	h_{atm}	1500	km
Incoming hyperbolic excess velocity	V_∞^-	18	km/s
Target capture orbit period	P	20	days

where S and C_D are the aerodynamic reference area and drag coefficient respectively. The two types of heating affecting the vehicle during entry are convective and radiative heating. The relationship modeled in the current work uses an empirical form of the heating-rates with:

$$\dot{q} = \dot{q}_c + \dot{q}_r = k_c \rho^a V^b + k_r \rho^c V^d \tag{5.2}$$

where $\dot{q}_c$ and $\dot{q}_r$ are the convective and radiative heating rates respectively. k_c, a, b, k_r, c, and d are empirical constants given by:

$$\begin{aligned} k_c &= \sqrt{\frac{0.291}{r_n}}\left(2.24008\times10^{-7}\right) \\ a &= 0.452130 \\ b &= 2.6918 \\ k_r &= \sqrt{\frac{r_n}{0.291}}\left(2.8699\times10^{-63}\right) \\ c &= 0.498140 \\ d &= 15.113 \end{aligned} \tag{5.3}$$

5.2 The Rotating Atmosphere

Certain considerations must be taken into account when including atmospheric rotation in the equations of motion. In deriving the equations of motion from Vinh [26], the velocity vector is derived with respect to the planet. This means the velocity, flight-path angle, and heading (V, γ, ψ) in equations (3.1) – (3.6) are all formulated with respect to the rotating planet. When approaching the atmosphere, V, γ, and ψ are all inertial until atmospheric entry. Upon entry, they must be transformed to be with respect to the planet with the following relationships:

$$\begin{aligned}
V &= \sqrt{{V_{PL}}^2 + r^2\Omega^2\cos^2\phi + 2r\Omega V_{PL}\cos\phi_{PL}\cos\psi_{PL}\cos\gamma_{PL}} \\
\sin\gamma &= \frac{V_{PL}}{V}\sin\gamma_{PL} \\
\cos\psi &= \frac{V_{PL}\cos\gamma_{PL}\cos\psi_{PL} + r\Omega\cos\phi}{V\cos\gamma} \\
\sin\psi &= \frac{V_{PL}\cos\gamma_{PL}\sin\psi_{PL}}{V\cos\gamma}
\end{aligned} \tag{5.4}$$

The subscript *PL* indicates that the variable is taken with respect to the planet; the others are inertial variables.

In the formulation of the TPBVP, equation (5.4) must be included in the boundary conditions as terminal constraints, as some initial and final conditions are given in the inertial frame, but the dynamics are modeled with respect to the planet. The variables can be uniquely determined with three equations. First the entry or exit speed with respect to the planet is evaluated with the first in equation (5.4). Since the flight-path-angle is defined as being between $-\pi/2 \leq \gamma \leq \pi/2$ and is found directly with the second equation:

$$\gamma_{PL} = \sin^{-1}\left(\frac{V}{V_{PL}}\sin\gamma\right) \tag{5.5}$$

The heading angle is defined between $-\pi \leq \psi \leq \pi$, meaning a quadrant check is necessary to get the correct value. However, unless the vehicle is approaching the planet with an inclination close to $\pm\pi/2$ (polar orbit), the initial and final orbits pre and post-aerocapture will in general, both be prograde or retrograde. This means either the last or second-to last equation in (5.4) can be used to find the appropriate ψ with a careful consideration of signs. Trying to include both equations in the terminal constraints gives a problem of scale invariance, making the Jacobian matrix singular upon getting close to the solution.

The known initial boundary conditions of the aerocapture problem are $r_0, \theta_0, \phi_0, V_{0,i}$, and $\psi_{0,i}$, where the subscript *i* indicates the variable is taken with respect to an inertial reference frame. The final boundary conditions are r_f and $V_{f,i}$. The final inertial velocity $V_{f,i}$ is found by the vis viva equation using the desired captured orbital period *P*. Since the boundary conditions have inertial values and the dynamics are derived with respect to the planet, a terminal constraint vector is used to relate them. After substituting equation (5.5) into equation (5.4), the terminal constraints are:

$$\boldsymbol{\Psi} = \begin{bmatrix} \sqrt{V_0^2 + r_0^2\Omega^2\cos^2\phi_0 + 2r_0\Omega V_0\cos\phi_0\cos\psi_0\cos\gamma_0} - V_{0i} \\ \dfrac{V_0\cos\gamma_0\sin\psi_0}{\sqrt{V_{0i}^2 - V_0^2\sin^2\gamma_0}} - \sin\psi_{0i} \\ \sqrt{V_f^2 + r_f^2\Omega^2\cos^2\phi_f + 2r_f\Omega V_f\cos\phi_f\cos\psi_f\cos\gamma_f} - V_{fi} \end{bmatrix} = \mathbf{0} \tag{5.6}$$

where the last of equation (5.4) is used to relate the inertial heading.

5.3 Optimal Control Formulation

The optimal control problem is set up by adjoining the terminal constraint vector in equation (5.6) to the cost functional:

$$\text{Min } J = \int_{t_0}^{t_f} \left(k_c\rho^a V^b + k_r\rho^c V^d\right)dt + \boldsymbol{\nu}^T\boldsymbol{\Psi} \tag{5.7}$$

with constant Lagrange multipliers ν^T. Nondimensionalizing the problem yields better computational performance when solving the problem numerically. The nondimensional variables are:

$$\bar{r} = r/r_0, \quad \bar{v} = V\sqrt{r_0/\mu}, \quad \bar{\Omega} = \Omega\sqrt{r_0^3/\mu}, \quad \tau = t\sqrt{\mu/r_0^3} \tag{5.8}$$

giving the following set of differential equations:

$$\begin{aligned}
\bar{r}' &= \bar{v}\sin\gamma \\
\theta' &= \frac{\bar{v}\cos\psi\cos\gamma}{\bar{r}\cos\phi} \\
\phi' &= \frac{\bar{v}\sin\psi\cos\gamma}{\bar{r}} \\
\bar{v}' &= -\bar{D} - \frac{1}{\bar{r}^2}\sin\gamma + \bar{\Omega}^2\bar{r}\cos\phi\left(\sin\gamma\cos\phi - \cos\gamma\sin\phi\sin\psi\right) \\
\gamma' &= \frac{\bar{L}}{\bar{v}}\cos\sigma - \left(\frac{1}{\bar{r}^2\bar{v}} - \frac{\bar{v}}{\bar{r}}\right)\cos\gamma + 2\bar{\Omega}\cos\phi\cos\psi \\
&\quad + \frac{\bar{\Omega}^2\bar{r}}{\bar{v}}\cos\phi\left(\cos\gamma\cos\phi + \sin\gamma\sin\phi\sin\psi\right) \\
\psi' &= \frac{\bar{L}}{\bar{v}\cos\gamma}\sin\sigma - \frac{\bar{v}}{\bar{r}}\cos\gamma\cos\psi\tan\phi \\
&\quad + 2\bar{\Omega}\left(\tan\gamma\cos\phi\sin\psi - \sin\phi\right) - \frac{\bar{\Omega}^2\bar{r}}{\bar{v}\cos\gamma}\cos\phi\sin\phi\cos\psi
\end{aligned} \tag{5.9}$$

where the derivatives are taken with respect to the nondimensional time τ. The lift and drag variables are given in terms of the lift-to-drag ratio and the ballistic coefficient:

$$\bar{D} = \frac{\rho\bar{v}^2 r_0}{2B}, \qquad \bar{L} = \frac{\rho\bar{v}^2 r_0}{2B}E^* \tag{5.10}$$

The Hamiltonian is formed with:

$$\begin{aligned}
H &= \lambda_{\bar{r}}\left(\bar{v}\sin\gamma\right) + \lambda_{\theta}\left(\frac{\bar{v}\cos\psi\cos\gamma}{\bar{r}\cos\phi}\right) + \lambda_{\phi}\left(\frac{\bar{v}\sin\psi\cos\gamma}{\bar{r}}\right) \\
&+ \lambda_{\bar{v}}\left[-\bar{D} - \frac{1}{\bar{r}^{2}}\sin\gamma + \bar{\Omega}^{2}\bar{r}\cos\phi\left(\sin\gamma\cos\phi - \cos\gamma\sin\phi\sin\psi\right)\right] \\
&+ \lambda_{\gamma}\left[\frac{\bar{L}}{\bar{v}}\cos\sigma - \left(\frac{1}{\bar{r}^{2}\bar{v}} - \frac{\bar{v}}{\bar{r}}\right)\cos\gamma + 2\bar{\Omega}\cos\phi\cos\psi\right. \\
&\left.+ \frac{\bar{\Omega}^{2}\bar{r}}{\bar{v}}\cos\phi\left(\cos\gamma\cos\phi + \sin\gamma\sin\phi\sin\psi\right)\right] + \lambda_{\psi}\left[\frac{\bar{L}}{\bar{v}\cos\gamma}\sin\sigma\right. \\
&- \frac{\bar{v}}{\bar{r}}\cos\gamma\cos\psi\tan\phi + 2\bar{\Omega}\left(\tan\gamma\cos\phi\sin\psi - \sin\phi\right) \\
&\left.- \frac{\bar{\Omega}^{2}\bar{r}}{\bar{v}\cos\gamma}\cos\phi\sin\phi\cos\psi\right]
\end{aligned} \tag{5.11}$$

and the necessary conditions for local optimality are applied:

$$\boldsymbol{\lambda}' = -\frac{\partial H}{\partial \boldsymbol{x}}, \qquad \frac{\partial H}{\partial \sigma} = \mathbf{0}, \qquad \frac{\partial^{2} H}{\partial \sigma^{2}} \geq 0 \tag{5.12}$$

The costate differential equations are omitted for brevity. The algebraic equations for the control variable are found from satisfying the second and third equation in (5.12):

$$\begin{aligned}
\cos\sigma &= -\frac{\lambda_{\gamma}\cos\gamma}{\sqrt{\lambda_{\gamma}^{2}\cos^{2}\gamma + \lambda_{\psi}^{2}}} \\
\sin\sigma &= -\frac{\lambda_{\psi}}{\sqrt{\lambda_{\gamma}^{2}\cos^{2}\gamma + \lambda_{\psi}^{2}}}
\end{aligned} \tag{5.13}$$

where the negative sign is required to ensure the Hessian is positive semi-definite. Lastly, the transversality conditions must be satisfied to obtain the necessary number of boundary conditions for a well-defined TPBVP. These boundary conditions are:

$$\begin{aligned}
&\lambda_{V0} = -\boldsymbol{\nu}^{T}\frac{\partial \boldsymbol{\Psi}}{\partial V_{0}},\ \lambda_{\psi 0} = -\boldsymbol{\nu}^{T}\frac{\partial \boldsymbol{\Psi}}{\partial \psi_{0}},\ \lambda_{\gamma 0} = -\boldsymbol{\nu}^{T}\frac{\partial \boldsymbol{\Psi}}{\partial \gamma_{0}},\ \lambda_{\phi f} = \boldsymbol{\nu}^{T}\frac{\partial \boldsymbol{\Psi}}{\partial \phi_{f}}, \\
&\lambda_{Vf} = \boldsymbol{\nu}^{T}\frac{\partial \boldsymbol{\Psi}}{\partial V_{f}},\ \lambda_{\gamma f} = \boldsymbol{\nu}^{T}\frac{\partial \boldsymbol{\Psi}}{\partial \gamma_{f}},\ \lambda_{\psi f} = \boldsymbol{\nu}^{T}\frac{\partial \boldsymbol{\Psi}}{\partial \psi_{f}},\ H_{f} = 0
\end{aligned} \tag{5.14}$$

5.4 Simulation and Analysis

Initial and final conditions for a Uranus aerocapture simulation are given in Table 5.2. The optimal control problem was first numerically solved using a collocation method with a third-order polynomial to fit the dynamics to get an accurate initial estimate. Then a multiple shooting method using an eighth-order Runge-Kutta Prince Dormand explicit numerical integrator was employed to refine the solution.

Table 5.2 Boundary conditions for aerocapture simulation

Parameter	Value	Units
r_0	27000	km
θ_0	0	deg
ϕ_0	–74	deg
$V_{0,i}$	27.444	km/s
$\psi_{0,i}$	12	deg
r_f	27000	km
$V_{f,i}$	20.532	km/s

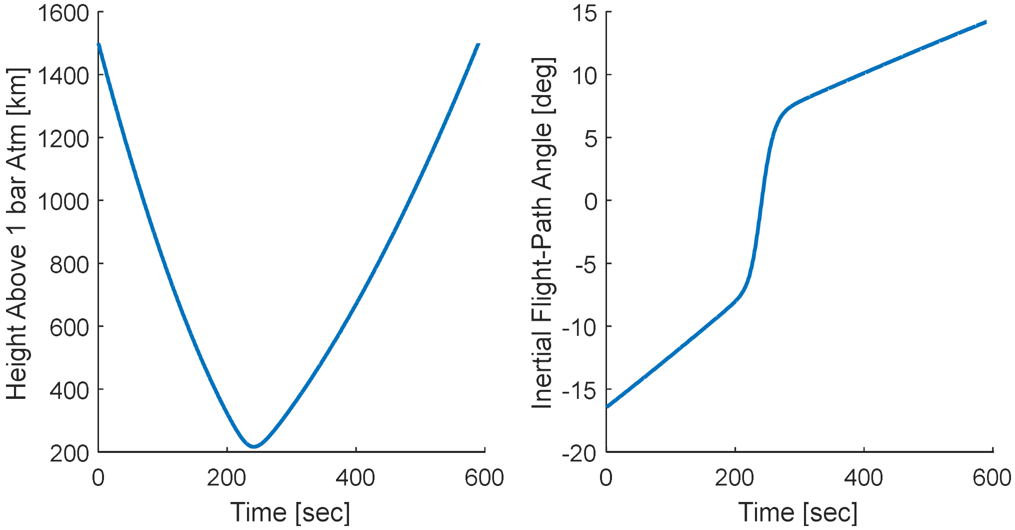

Figure 5.1: Altitude and inertial flight-path angle profiles for Uranus aerocapture.

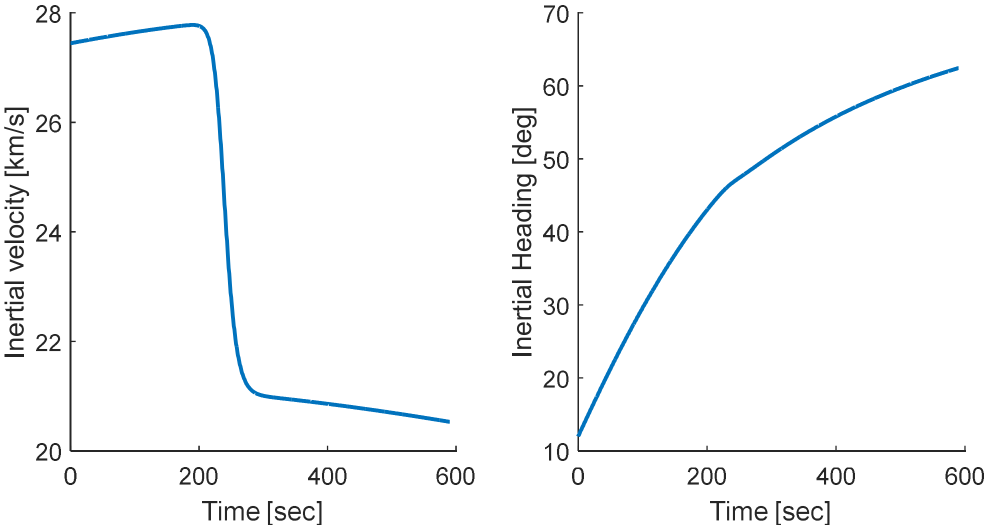

Figure 5.2: Inertial velocity and heading profiles for Uranus aerocapture.

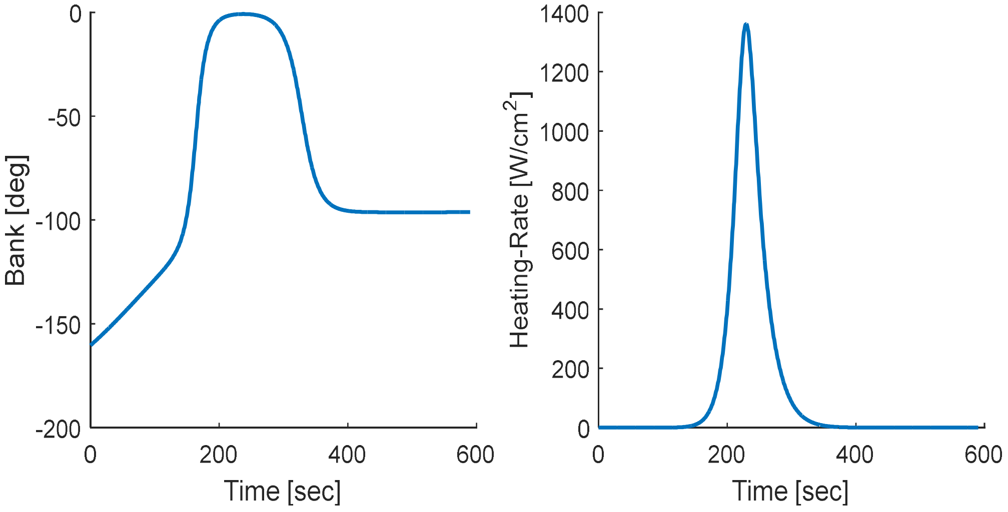

Figure 5.3: Bank angle and heating-rate profiles for Uranus aerocapture.

Figure 5.2 — Figure 5.3 give the altitude, inertial flight-path angle, inertial velocity, inertial heading, bank angle, and heating-rate profiles. The vehicle enters with an inertial flight-path angle of –16.44 degrees and descends steadily until approximately 200 km above the 1 bar atmospheric pressure radius. The velocity bleeds off heavily when the vehicle is at its lowest, while the heat-rate spikes to approximately 1400 W/cm^2.

The inertial heading starts at 12 degrees, approximately due east, and approaches the north ending at ~65 degrees. The bank angle starts out with the lift vector almost upside-down at an angle of –160 degrees. The vehicle then rolls over to a lift-upward position of approximately zero degrees when the vehicle is around the lowest point in the trajectory. Upon ascension out of the atmosphere, the vehicle rolls back over to an angle of –96 degrees where it stays until it exits. The total heat load accrued over the trajectory is 74.05 kJ/cm^2 with a peak heat-rate of 1361 W/cm^2. The majority of the control effort occurs during the descent and ascent of the vehicle. During these times the atmospheric density is almost negligible, meaning most of the aerodynamic effects occur at the lowest point, between the interval of 200 and 300 seconds into the atmosphere.

5.5 Suboptimal Aerocapture Result

Since the lift vector is pointing mostly upwards at this time, it makes sense that a suboptimal solution to the minimal heat load case would be a trajectory with the bank angle equal to zero the whole time. In fact, when the atmosphere's rotation is not modeled in the dynamics, the zero bank angle solution is the minimum heat load solution, which was verified by setting $\Omega = 0$ in the equations of motion and solving the associated TPBVP. The plots of the states with no rotation look very similar to the figures above, and would look almost identical when plotted against each other. A main difference however is that the total heat load with no atmospheric rotation is 83.75 kJ/cm^2 with a peak heating-rate of 1564 W/cm^2. Thus when entering the atmosphere in a prograde orbit, the atmospheric rotation helps to decrease the total heat load, whereas a retrograde orbit would increase it.

The suboptimal solution with a bank angle of zero, including atmospheric rotation, is solved via a targeting problem. The free-variables associated with the targeting problem are:

$$\boldsymbol{X} = \begin{bmatrix} V_0 & \gamma_0 & \psi_0 & \phi_f & V_f & \gamma_f & \psi_f & t_f \end{bmatrix}^T \tag{5.15}$$

with the following constraint vector on the states:

$$\boldsymbol{F}\left(\boldsymbol{X}\right) = \begin{bmatrix} r(0) - r_0 \\ \theta(0) - \theta_0 \\ \phi(0) - \phi_0 \\ Q(0) - 0 \\ \sqrt{V_0^2 + r_0^2 \Omega^2 \cos^2 \phi_0 + 2 r_0 \Omega V_0 \cos\phi_0 \cos\psi_0 \cos\gamma_0} - V_{0,i} \\ \dfrac{V_0 \cos\gamma_0 \sin\psi_0}{\sqrt{V_{0i}^2 - V_0^2 \sin^2 \gamma_0}} - \sin\psi_{0i} \\ r(t_f) - r_f \\ \sqrt{V_f^2 + r_f^2 \Omega^2 \cos^2 \phi_f + 2 r_f \Omega V_f \cos\phi_f \cos\psi_f \cos\gamma_f} - V_{f,i} \end{bmatrix} \tag{5.16}$$

where Q is the variable for the heat load, and the inertial initial velocity and heading, and inertial final velocity ($V_{0,i}$, $\psi_{0,i}$, and $V_{f,i}$) are known. The Jacobian matrix is:

$$D\boldsymbol{F}\left(\boldsymbol{X}\right) = \begin{bmatrix} \Phi\left(t_f, t_0\right) & -\mathbf{I} & \dfrac{\partial \boldsymbol{x}}{\partial t_f} \\ \dfrac{\partial \boldsymbol{F},}{\partial \boldsymbol{x}_0} & 0 & 0 \\ 0 & \dfrac{\partial \boldsymbol{F}}{\partial \boldsymbol{x}_f} & 0 \end{bmatrix} \tag{5.17}$$

The targeting problem is solved via multiple shooting using the solution of the optimal control problem as the initial guess for the states. When comparing the optimal and suboptimal solutions, the only state that is noticeably different is the inertial heading angle in Figure 5.4. The optimal (blue) and suboptimal (red) are not noticeably different during the descent into the atmosphere, but diverge slightly upon ascent. The total heat load for the suboptimal solution is 74.06 kJ/cm^2 with a peak heat-rate of 1360 W/cm^2; there is only 0.01 kJ/cm^2 and 1 W/cm^2 difference between the two solutions. The reason for such close proximity of the solutions is that the majority of the heating occurs when the altitude is at its lowest and the bank angle for the two solutions are both zero (or close

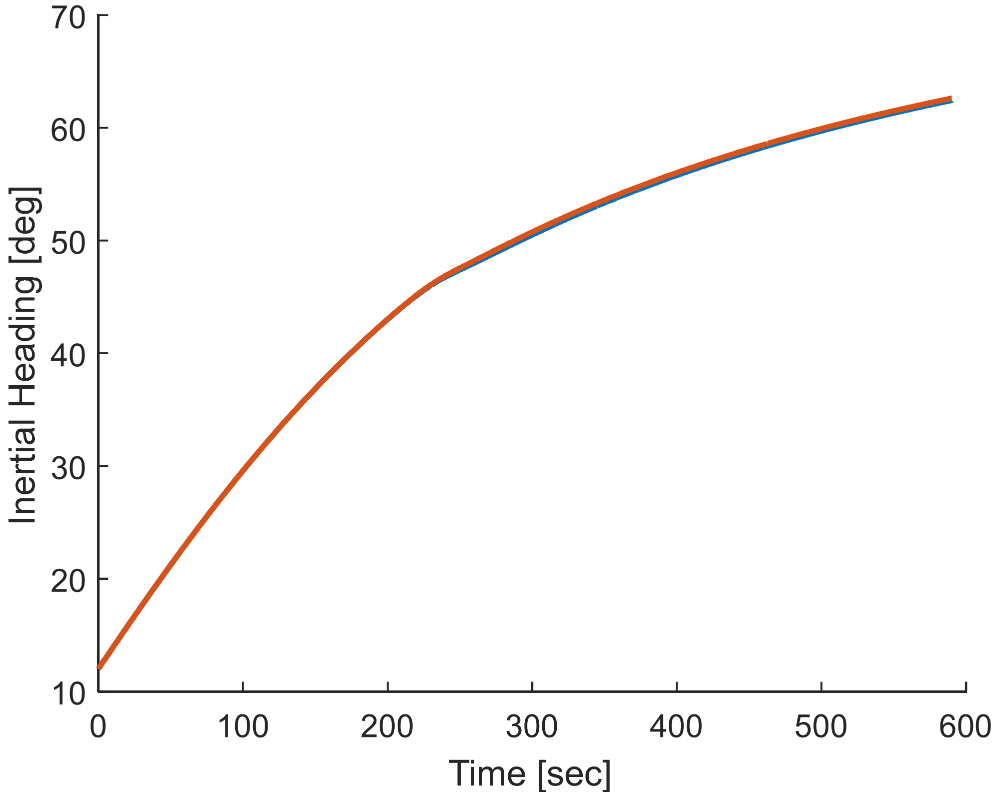

Figure 5.4: Inertial heading angles for optimal and suboptimal aerocapture solutions.

to zero); where the bank angle widely varies in the optimal solution is where the density, and therefore the influence of the control on the dynamics, is almost negligible.

The two solutions presented yielded practically the same results in terms of total heat load and peak heating rates. In a practical sense, the suboptimal solution would most likely be the one to be implemented on an actual mission due to the added complexity of satisfying the necessary conditions of optimality. A bank of zero degrees would be the easiest situation around which to construct a guidance scheme, as the model will invariably be subjected to dispersions in atmospheric density, aerodynamics, and initial conditions.

CHAPTER 6. INSPIRATION MARS 2018 OPPORTUNITY

Mars has been a destination of interest for human space-flight for over half a century [46–60]. Due to the orbital positions of Earth and Mars, it is found that a launch date set in early 2018 is the best opportunity for a human free-return mission to Mars this century. The 2018 trajectory, found by Patel et al. [55], became a main source of motivation for Inspiration Mars, a proposed human free-return mission to Mars made by Dennis Tito et al. [58]. Tito and his colleagues selected one of the trajectories on January 5, 2018, and performed a successful high-fidelity numerical integration to confirm its existence. This trajectory was selected due to its ‘fast’ time of flight (TOF), low Earth launch energy and low Earth re-entry speed.

The question then arises as to how often these types of trajectories exist, and whether or not another desirable opportunity like the 2018 trajectory exists sometime nearby in case the 2018 one cannot be launched. The metrics used in evaluating a desirable opportunity is the Earth launch energy and re-entry speed such that the mission can be flow using current technology. It turns out that the TOF, which is usually of concern to human missions, remains around 500 days for all the candidates of this type of mission, so it is not given any weight in the decision process. Opportunities similar to 2018 occurs approximately every 15 or 17 years, however the 2018 trajectory demonstrates to be superior overall.

The Satellite Tour Design Program (STOUR), capable of designing interplanetary missions using patched conics, was designed by engineers at JPL [34]. STOUR was then made fully automated by Williams [35], finding every interplanetary trajectory with only a few user inputs written on a scripted file. The STOUR program can find rapid Mars free-return trajectories using by stepping through the user-specified launch dates and launch energies. The results are then consolidated, and the desirable trajectories are selected with low launch energies and low re-entry speeds.

After compiling all of the trajectories found using STOUR, the results are filtered based on the launch energy (C_3) and arrival speed (V_{Arr}). Using the 2018 opportunity as the baseline, the desirable trajectories are ones that possess a similar C_3 and V_{Arr}.

Radial distance plots of Earth, Mars, and the spacecraft's positions exhibit trends to provide low Earth launch and re-entry energies. The good trajectories tend to depart Earth at its perihelion, and intercept Mars at its perihelion. The departure from Earth and swing-by of Mars at their closest approaches to the Sun makes sense, as the most energy is transferred to a spacecraft with respect to the Sun when the body is travelling its fastest. Each synodic period of Earth and Mars is approximately two and one-seventh years; the synodic period varies due to the relative inclinations and nonzero eccentricities of the two planets. When these variations are small compared to the 2018 opportunity, a similar desirable trajectory exists.

To gain further insight to when a desirable Mars free-return trajectory exists, a time-free ephemeris model is constructed to see exactly which relative Earth-Mars positions are ideal. The time-free ephemeris model is an ephemeris built under the pretense that the positions of Earth and Mars can be at any position at any given time along their heliocentric paths. A further assumption imposed, is that the heliocentric paths of Earth and Mars remained fixed, and their orbital elements do not change due to perturbations from other planets. The aforementioned radial distance plots give insight where to search for desirable trajectories along Earth's and Mars's orbital paths.

The trajectories found using the TFE have C_3 and V_{Arr} that are as good, or are better than the 2018 opportunity. It is then possible to see the necessary relative geometry that Earth and Mars must have for these "best-case" free-return trajectories.

6.1.1 Best Case Mars Free-Returns Found this Century

The STOUR program was used to find launch dates for Mars free-return trajectories over this century, logging all candidates that had launch energies below 43 km^2/s^2, Mars fly-by altitudes greater than 200 km, and Earth re-entry speeds less than 14.5 km/s, based at 100 km altitude (these numbers are denoted as Inspiration Mars, or IM constraints from now on). Figure 6.1 shows the output from STOUR with a search ranging from January 1, 2000 to December 31, 2099. The step size in Earth launch V_∞ ranged from 6 km/s to 7 km/s with a step size of 0.1 km/s, however only results set by the above constraints are shown on the plot.

It turns out that the types of trajectories satisfying the IM constraints appear every 15, and sometimes 17 years, with the best appearing in late 2017/early 2018. Since the synodic period of Earth and Mars is roughly two and one-seventh years, the inertial geometry repeats every seven synodic periods, or 15 years. Due to the nonzero inclinations of Mars and nonzero eccentricities of both Earth and Mars, the "best-case" missions can appear one synodic period later, creating the occasional 17-year time increment.

Out of the 100-year search, the seven trajectories listed in Table 6.1 are the trajectories found this century that closely match the 2018 opportunity, with the second entry representing IM mission. The trajectory closest to the IM mission is the last entry corresponding to a launch in 2097—a date far off, where hopefully humans will not just be performing free-return flybys of Mars. The first entry, the most recent free-return trajectory closest to the IM mission in 2000 portrayed a high C_3 which violated the upper bound of 43 km^2/s^2 set by the IM constraint, as well as a high V_{Arr}. The next best Mars

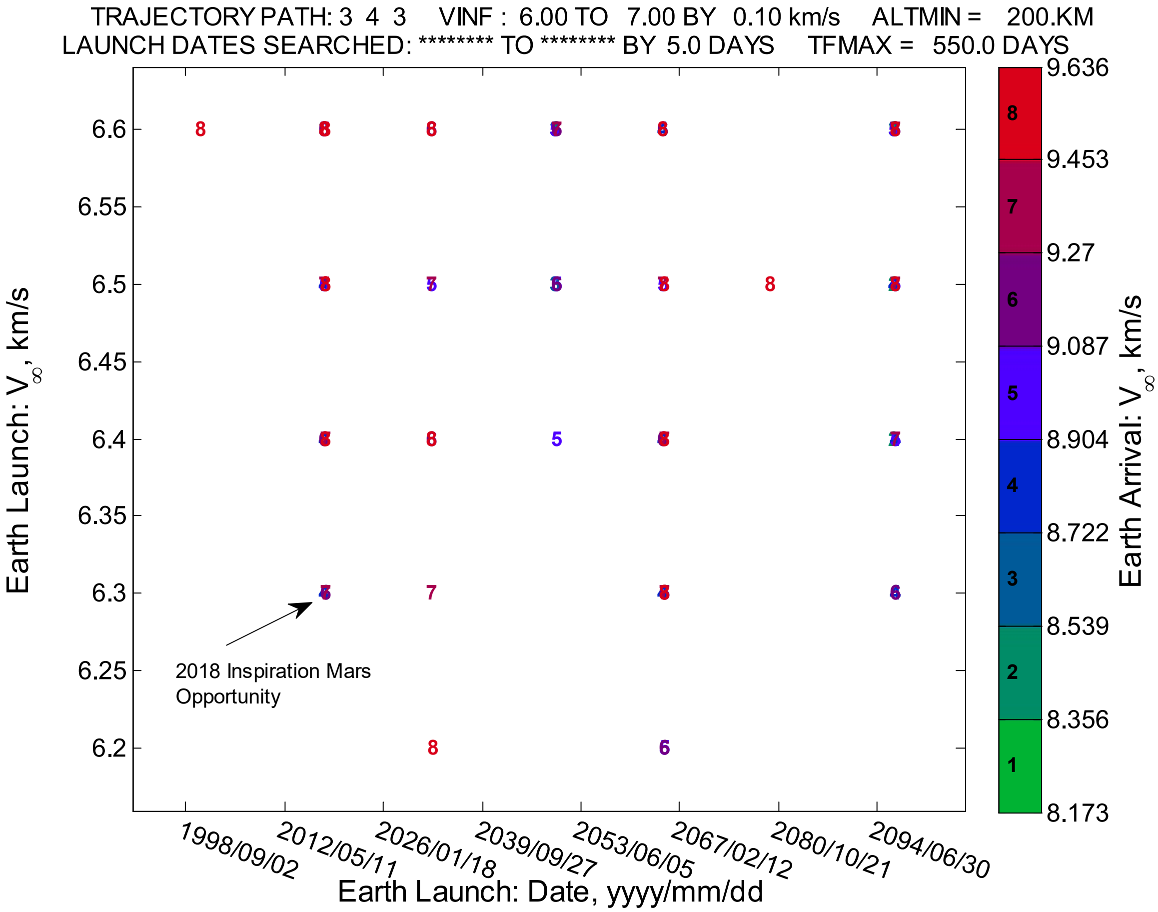

Figure 6.1: Mars free-return trajectories found using STOUR spanned over this century (01/01/2000 – 12/31/2100). Each trajectory displayed satisfies the IM constraints of C_3 less than 43 km^2/s^2, Mars fly-by altitudes greater than 200 km, and Earth re-entry speeds less than 14.5 km/s.

free-return occurs about 15 years later from 2018, in late 2032, with a lower C_3 of 38.4 km^2/s^2, but higher entry speed of 14.4 km/s. It is clear from Table 1 that the IM trajectory in 2018 (represented by the second entry) is the best found this century in terms of its V_{Arr}. In terms of metrics, V_{Arr} is weighted a bit more over C_3 due to limitations in current technology. According to SpaceX, the Falcon Heavy, advertised to be launched sometime in 2014, will be able to propel 13.2 tons to Mars which is sufficient for the estimated payload mass for the Inspiration Mars mission. The entry speed limitation is more of a critical design factor since current technologies can handle entry speeds of about 14.5 km/s or less; thus the lower the entry speed, the more desirable the trajectory.

Table 6.1 Mars free-return trajectories this century that display Earth launch energies and Earth entry speeds comparable to the Inspiration Mars 2018 opportunity[1]

Earth Launch Date (mm/dd/yyyy)	C_3 (km^2/s^2)	V_{Arr} (km/s)
11/11/2000	43.6	14.5
12/25/2017	40.2	14.0
12/08/2032	38.4	14.4
01/23/2050	41.0	14.1
12/20/2064	39.1	14.1
11/17/2079	42.3	14.4
12/22/2096	41.0	14.0

6.1.2 Radial Distance Plots

Radial distance plots are constructed to identify trends in the planets' positions that make the trajectories desirable. Over a specified time period, the radial distance of Earth, Mars and the spacecraft's trajectory with respect to the Sun are plotted allowing a visualization of the where on the planets' orbits the spacecraft is performing the flybys.

---

[1] The entry occurring on 01/01/2018 is the trajectory closest to the trajectory announced by Tito et al. [13].

Figure 6.2 shows the three best free-return opportunities this century. The first plot is an opportunity in late 2017 (within the same launch window as the nominal IM mission) with the lowest launch energy (C_3) and entry speed. The second plot is about 47 years later in late 2064, and the third plot, at the end of the century, in late 2096, are comparable to the nominal IM mission, but all have higher entry speeds.

All of the trajectories in Figure 6.2 possess similar characteristics in regards to where they leave Earth and intercept the orbit of Mars. They all seem to leave Earth at or around Earth's perihelion, and arrive close to, but not directly at Mars's perihelion. The case in late 2064 has the spacecraft arrive a bit before Mars is at its perihelion; while the trajectories in late 2017 and 2096 have the spacecraft arrive closer to Mars's perihelion.

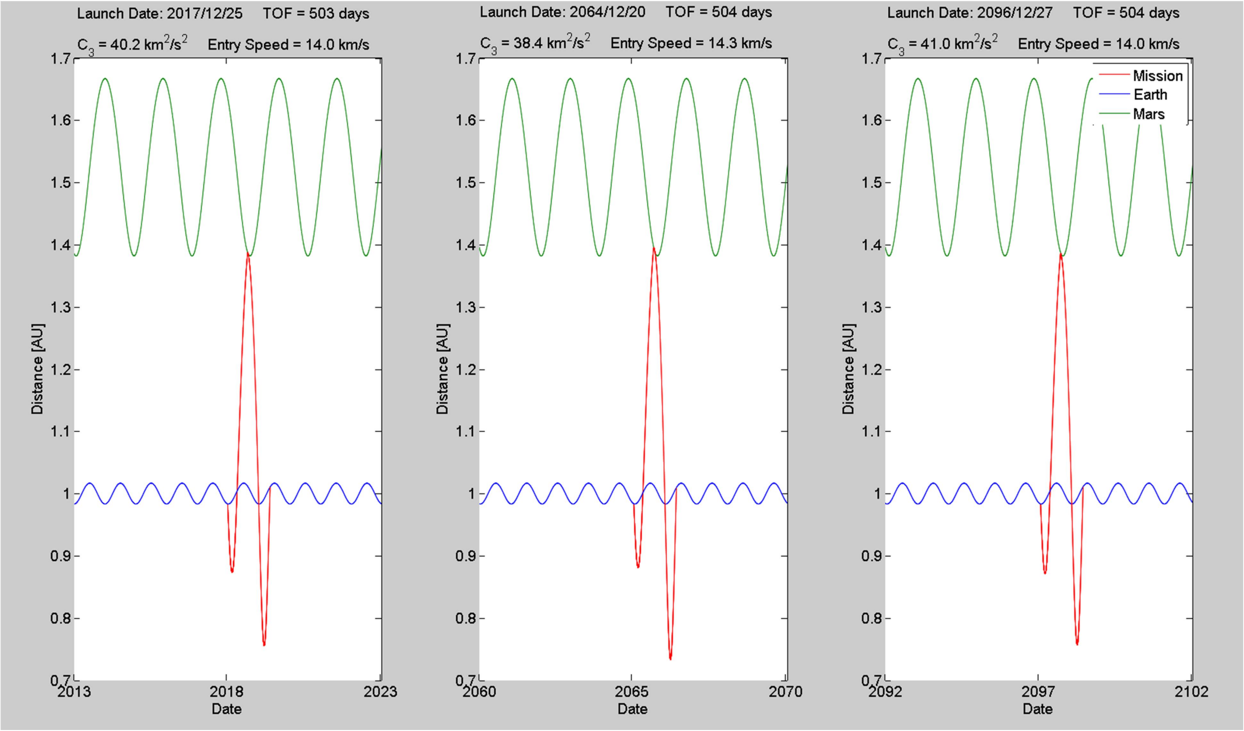

Figure 6.2: Similar desirable free-return opportunities to Mars. The first graph is the 2018 trajectory, and the other two are trajectories with similar characteristics, one occurring in 2064, and the other in 2096.

Due to the relative inclinations and eccentricities of Earth and Mars, it is expected that the spacecraft would not intersect the planets' orbits exactly at their respective perihelia, but rather have other geometries that produce desirable free-return trajectories.

6.1.3 Time-Free Ephemeris (TFE)

Due to the relative nonzero inclinations and eccentricities of Earth and Mars, it is difficult to predict when an optimal alignment will occur for a desirable Mars free-return trajectory. However the use of a time-free ephemeris tells where the planets would need to be for these trajectories. The trends of an Earth departure around its perihelion and a Mars fly-by around its perihelion appear to be common in the radial distance plots of the desirable trajectories, so they are used as the general search regions in the time-free ephemeris model.

The TFE works much the same way that STOUR does, except that the ephemeris used to describe the positions of Earth and Mars is user-defined. The planets' orbital elements are assumed to be constant and frozen on the date that the 2018 trajectory occurs. Lambert arcs are computed between the planets using a V_∞-matching algorithm to compute free-return trajectories. In this way, if the two Lambert arcs computed from Earth to Mars and from Mars to Earth possess the same V_∞ at Mars's arrival and departure, then a free-return trajectory exists. Then, if the trajectory has desirable C_3 and V_{Arr} characteristics, it is logged while others are discarded.

Mars's and Earth's positions around the Sun are user-specified by adjusting the constant found by integration resulting in Kepler's Equation, t_p, or time past periapsis

$$n\left(t-t_p\right)=E-e\sin E \tag{6.1}$$

where *n* is the planet's mean motion, *t* is the current time, *E* is the eccentric anomaly, and *e* is the eccentricity. By adjusting t_p, the planet's position can be computed by iteratively solving equation (6.1) for *E*. With both the planets' positions and a user-input TOF, Lambert arcs between the planets are computed.

The first solution space searched in the TFE included hard constraints on the positions of Earth and Mars where they are both set to lie at their respective perihelia. A constraint was also imposed on the Mars arrival arc where the trajectory ended at the Lambert arc's aphelion, as suggested by the radial distance plots. Since there are three inputs to the Lambert arc algorithm (assuming zero revolutions about the Sun), and three

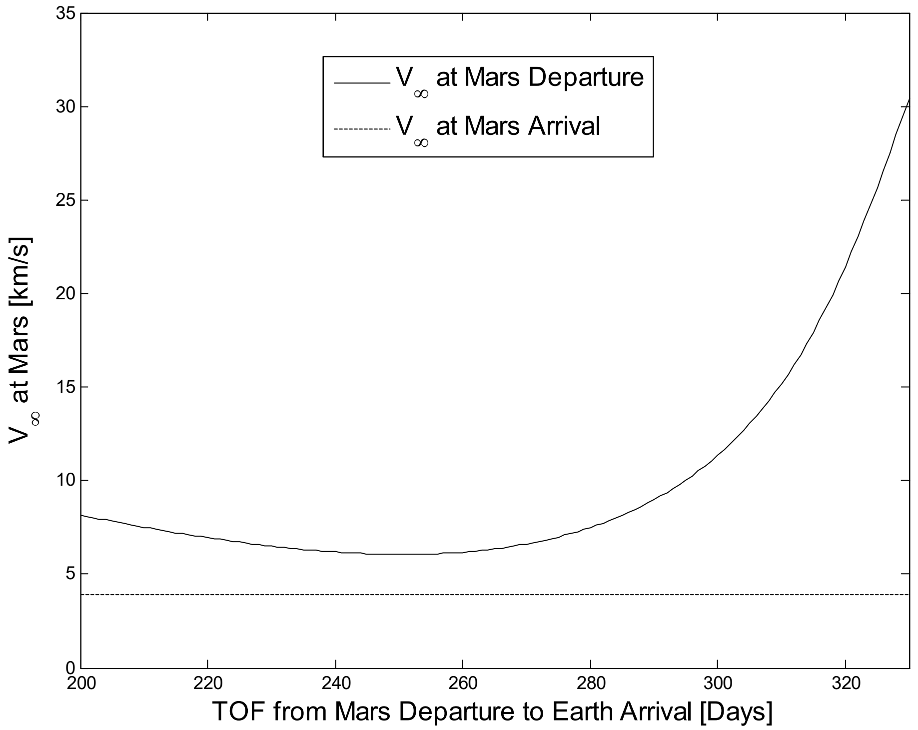

Figure 6.3: A plot showing the possible V_∞'s of departure at Mars versus the V_∞ of arrival when Earth and Mars are located at their respective perihelia. If the solid and dashed lines intersect, then the V_∞ of arrival and V_∞ of departure match, and a free-return trajectory exists.

imposed constraints, only one unique solution for the outbound arc is available. Since Earth was assumed to start at its perihelion, we propagate its trajectory forward in time, computing lambert arcs with corresponding V_∞ of departure from Mars. Unfortunately, no free-return trajectories exist for any TOF input to the lambert algorithm, as illustrated in Figure 6.3.

Figure 6.3 illustrates how the V_∞ (or C_3) matching algorithm works, which is incorporated into STOUR and the TFE. For each V_∞ of arrival at Mars computed from the first Lambert arc from Earth to Mars, the second leg of Lambert arcs are computed with varying TOFs, with their associated V_∞ of departure at Mars. If the dashed line and the solid line intersect at one or more points, then the V_∞ of arrival and V_∞ of departure match, and a free-return trajectory exists, and the corresponding TOF is computed using a root-solving technique. In the TFE, a secant method is used to solve for the roots, since the two guesses required for such a method are each less than a day from the actual solution.

The second solution space searched in the TFE kept the constraints that Earth and Mars remain at their respective perihelia, but no requirements on the Lambert arcs. In this way, the total TOF for the free return trajectory was split between the Earth departure leg and the Earth arrival leg. Since the 2018 opportunity is approximately 500 days, the first Lambert arc was allotted a flight time around half that, that stepped from 200 to 300 days in one-day increments. The second leg's flight-time was varied from the first leg's flight-time, subtracted from a maximum allowed total TOF, set to 530 days. This was the range that all feasible IM-like free-return trajectories would be located. With the one-day steps between flight-times of the first leg, seven free-return trajectories were found and are listed in Table 2, while the Heliocentric plot of the trajectories are presented in Fig. 4, centered in the J2000 reference frame.

Table 6.2 Mars free-return trajectory characteristics from the TFE with Earth and Mars set at their respective perihelia

C_3 (km^2/s^2)	Entry Speed (km/s)	TOF (days)
55.3	14.0	525.1
54.2	14.0	523.5
53.0	13.9	521.8
51.9	14.0	519.9
50.8	13.8	517.5
49.7	13.8	514.5
48.7	13.7	509.8

The trajectories found in the second solution space exhibit the low arrival speeds congruent with the 2018 opportunity, however possess higher launch energies which are not within the bounds of the IM-constraints. These cases are not ideal for human missions due to the need for higher payload masses, meaning more propellant required during launch.

Since no other information could be gathered by leaving Earth and Mars at their respective perihelia, the next step is to move Earth and Mars around their perihelia to find the relative geometry that produces desirable trajectories.

The final solution space of the TFE for desirable Mars free-return trajectories are constructed by moving Earth's and Mars's relative positions. This is done mathematically by adjusting their respective times past perihelion, t_p. Earth at departure is moved around its perihelion by $t_{p,E}$ = ±40 days while Mars at its arrival is moved around its perihelion by $t_{p,M}$ = ±50 days, and all free-return trajectories are found using the aforementioned V_∞-matching technique, with one-day increments in the transfer time between Earth launch and Mars arrival. Those free-return trajectories possessing IM-like characteristics or better are retained, while all others are discarded.

Figure 6.5 shows all Mars free-return trajectories found using the TFE. The blue stars, red stars and green stars correspond to Earth launch, Mars fly-by and Earth arrival respectively. The yellow trajectory shows where the IM trajectory lies within the solution space of the TFE. These trajectories illustrate what kind of geometry Earth and Mars must have in order for an IM-like mission to exist. Of course, in reality, Earth and Mars cannot be moved around arbitrarily, and one must wait until the planets are in the proper

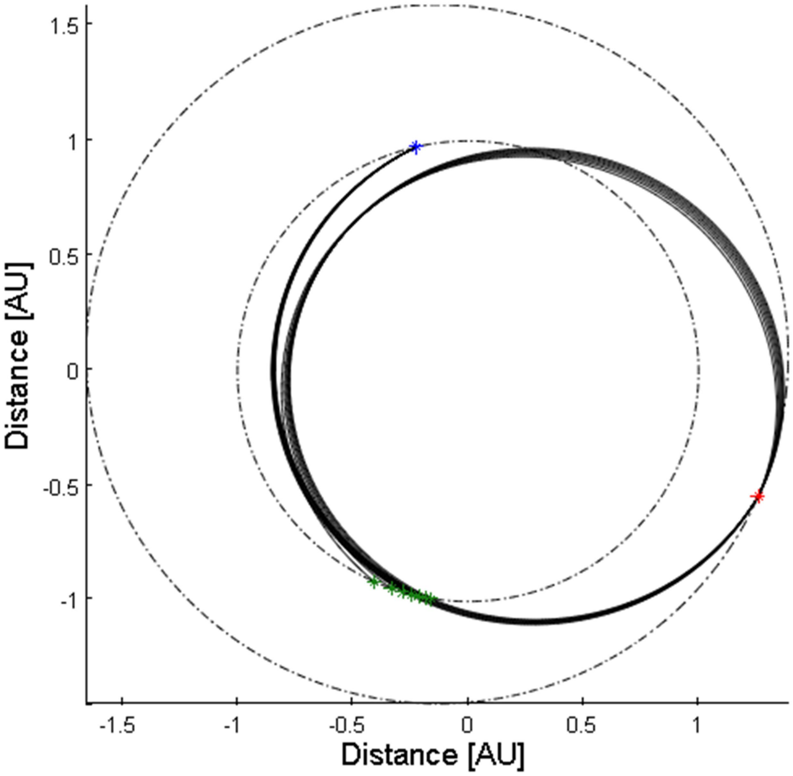

Figure 6.4: Mars free-return trajectories where Earth and Mars are fixed at their respective perihelia, and no constraints are imposed on the transfer arcs. The blue star indicates Earth launch, the red star indicates the Mars fly-by and the green stars are the possible Earth arrivals.

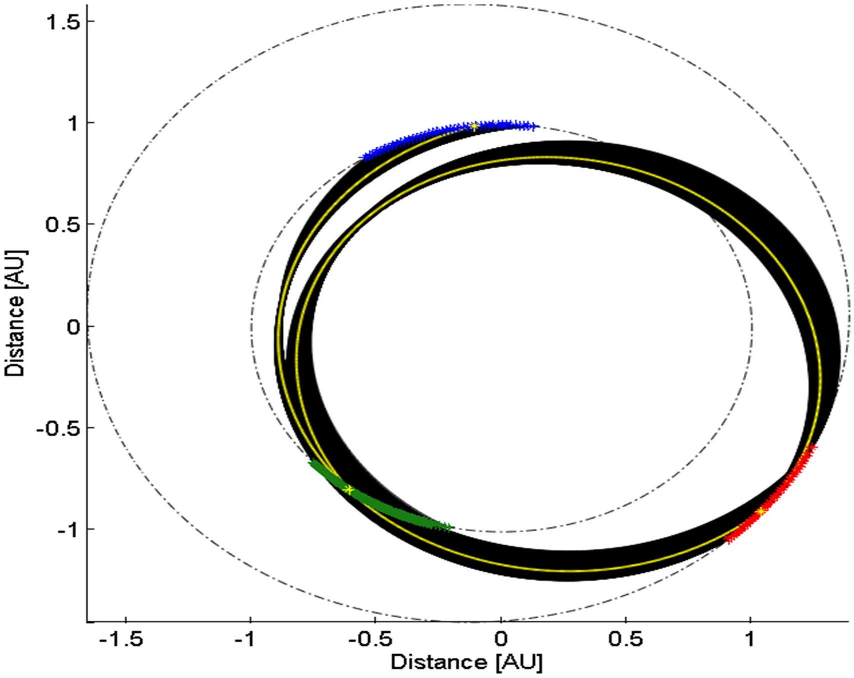

Figure 6.5: Mars free-return trajectories where Earth departure and Mars arrival are allowed to move in an arcs around their respective perihelia. The blue star indicates Earth launch, the red star indicates the Mars fly-by and the green stars are the possible Earth arrivals. The yellow trajectory corresponds to the 2018 IM opportunity.

alignment.

6.1.4 Launch Window for 2018 Opportunity

The STOUR search results, radial distance plots, and TFE analysis all clearly show that the best-case opportunities are highly sensitive to planetary geometry (and therefore launch date). In fact, simulations in STOUR about the 2018 opportunity (with launch date steps of 1 day and launch V_∞ of 0.1 km/s) show that the 2018 launch opportunity is only available from about 12/19/2017 to 1/3/2018. The results of the STOUR simulation are shown in Figure 6.6 with TOF, launch date, and launch V_∞ shown on the vertical axis, horizontal axis, and color bar, respectively. All results in the plot have Earth arrival V_∞ no larger than 9 km/s (entry speed of 12.29 km/s). The plot shows that to achieve this launch window, the launch V_∞ ranges from 6.3 km/s and 6.5 km/s (C3 from 39.7 km^2/s^2 to 42.3 km^2/s^2), and TOF from 502 days to 510 days. To restrict the launch V_∞ to 6.3 km/s and maintain a TOF near 503 days, the launch window is restricted to the lower group of opportunities (shown with index of 1 in the figure), which lasts about one week, from 12/28/2017 to 1/3/2018.

6.1.5 Deterministic Maneuvers

Part of the desirability of the 2018 opportunity for Inspiration Mars is that it is a *free* return, and therefore does not require any deterministic maneuvers to return the crew to Earth. Nevertheless, maneuvers are briefly investigated to determine if significant reductions in TOF, launch C3, and/or entry speed can be achieved, for a moderately sized impulsive ΔV. Only powered flybys at Mars are considered for this investigation, and are implemented in STOUR using a subroutine that places the maneuver 3 days after the Mars encounter—effectively increasing the energy change obtained from the Mars gravity assist. A full discussion of how this maneuver is implemented in STOUR is given in detail by Patel [61]. All maneuvers in this investigation are assumed impulsive and allowed a maximum ΔV size of 1 km/s.

Only near-term opportunities around the 2018 launch date are considered in the STOUR trajectory search using steps of 1 launch day and 0.25 km/s launch V_∞. The results show that the maneuver has little to no effect on TOF, as the trajectories found have TOF ranging from 497 days to 510 days—about the same as those found for the ballistic case (with no maneuver implemented). Specifically, to achieve a TOF of 497 days (only a few days shorter than the ballistic case) requires a maneuver size of 0.40 km/s ΔV, and launch V_∞ of 6 km/s.

The launch window was found to expand to as early as 12/14/2017 to as late as 2/5/2018, however many of these opportunities (near the extremes of these dates) require larger maneuver sizes of about 1 km/s. For more moderately sized maneuvers below 0.5 km/s, the launch window was found to be 12/18/2017 to 1/14/2018— still a few weeks longer than the available launch dates for the ballistic case.

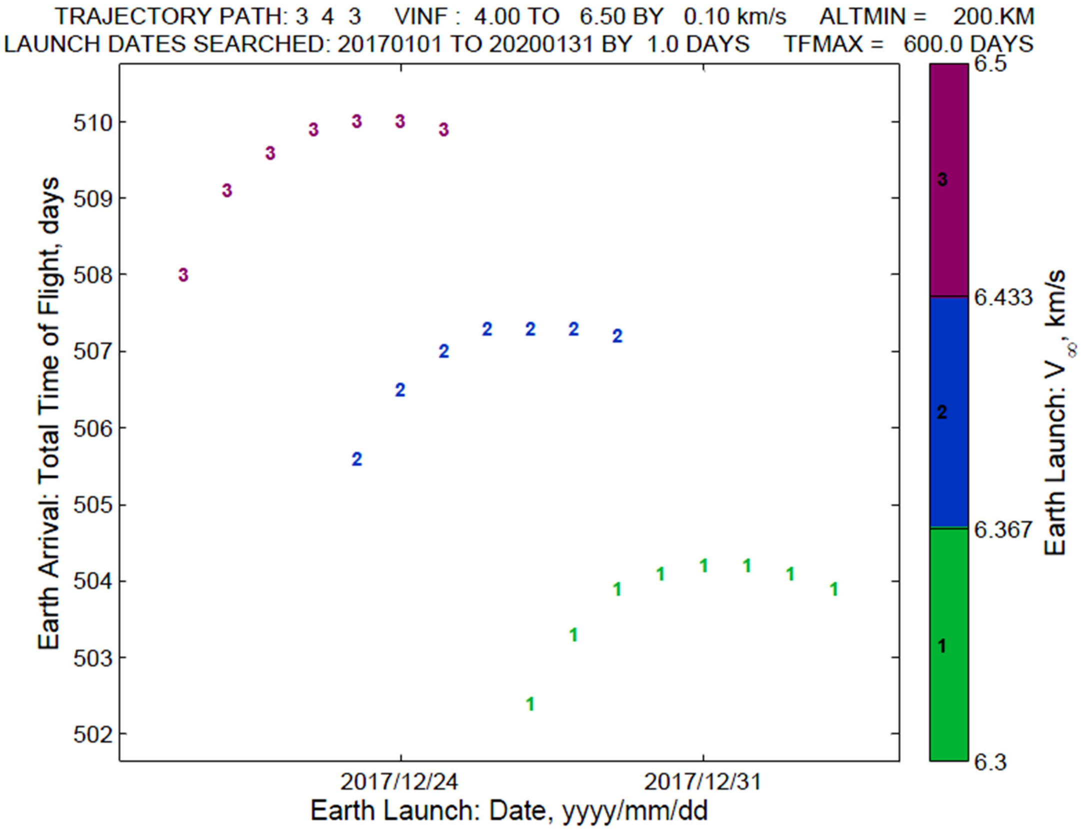

Figure 6.6: STOUR results showing available launch window for the 2018 opportunity, with TOF, launch date, and launch V_∞ shown on the vertical axis, horizontal axis, and color bar, respectively. Within the resolution of the STOUR search (one-day step in launch date and 0.1 km/s-step in launch V_∞), the earliest launch date occurs on 12/19/2017 with launch V_∞ of 6.5 km/s and the latest launch date occurs on 1/3/2018 with launch V_∞ of 6.3.

The impact of a maneuver on available launch and arrival V_∞ (or launch C3 and arrival entry speed) is shown in Figure 6.7. The figure shows the STOUR results with maneuver ΔV, arrival V_∞, and launch $V_{\infty,}$ shown on the vertical axis, horizontal axis, and color bar, respectively. For more moderately sized maneuvers with ΔV below 0.5 km/s, the figure shows that an arrival V_∞ of 8.29 km/s (entry speed of 13.8 km/s) is achievable for a small 65 m/s maneuver, with launch V_∞ of 6.5 km/s (C3 of 42.3 km^2/s^2). Overall, this is not much of a decrease from the ballistic trajectory with 14.0 km/s entry speed

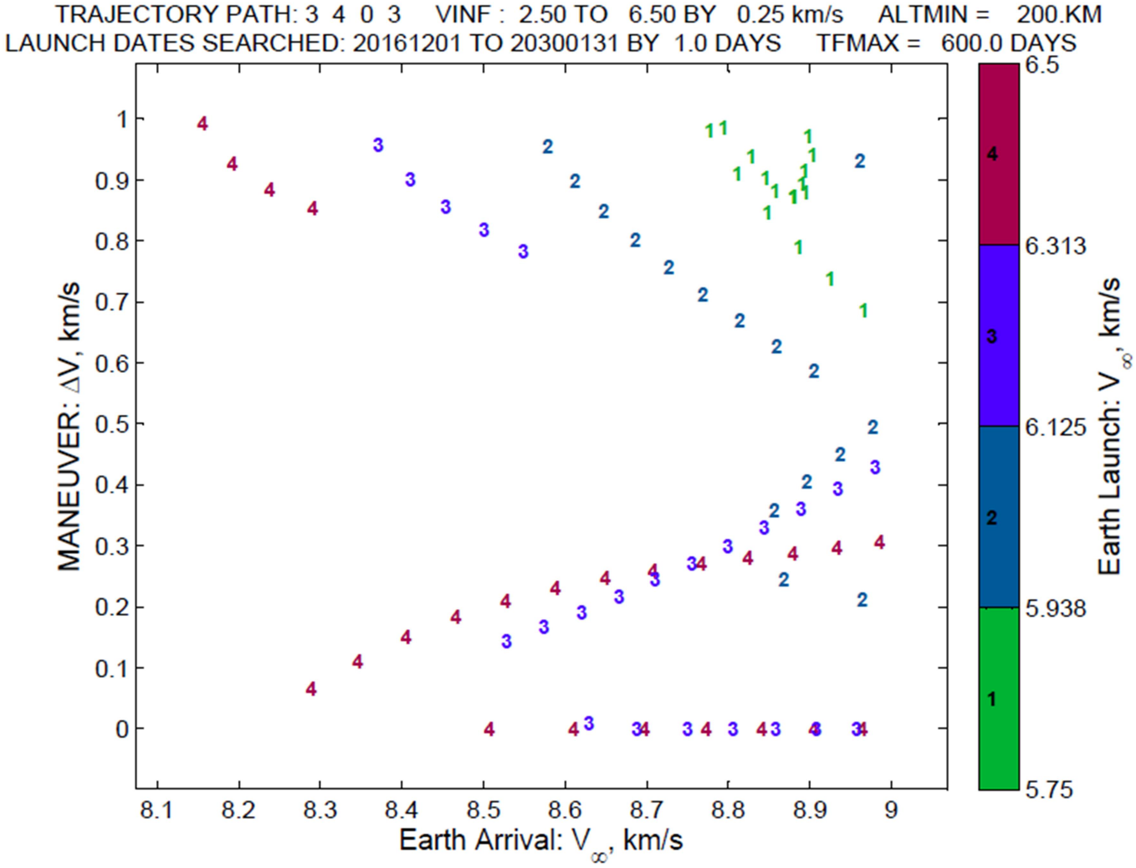

Figure 6.7: STOUR results showing available opportunities in late 2017/early 2018 with a powered flyby implemented at Mars. The Maneuver ΔV, arrival V_∞, and launch V_∞ are shown on the vertical axis, horizontal axis, and color bar, respectively. The maximum allowed maneuver size for the STOUR search is 1 km/s, with steps in launch date of 1 day, and steps in launch V_∞ of 0.25 km/s.

(shown in Table 6.1 with launch date on 12/25/2017), which only requires a C3 of 40.2 km^2/s^2.

With regard to reducing launch V_∞, Figure 6.7 shows that maneuvers of at least 0.69 km/s are required to obtain a launch V_∞ of 5.75 km/s (C3 of 33.1 km^2/s^2). Although this is a significant reduction in C3, it comes at the cost of a relatively large maneuver size, and may not provide any reduction in propellant cost. Additionally, the arrival V_∞ that results from such opportunities approach 9 km/s (entry speeds of 14.3 km/s), which (of the trajectories considered in this study) is relatively large. To achieve a launch V_∞ of 6 km/s (C3 of 36 km^2/s^2), maneuvers that are at least 0.21 km/s are required, and result in entry speeds near 14.2 km/s, providing very little to no benefit over the purely ballistic best cases.

Overall, this preliminary investigation of impulsive maneuvers suggests that the use of a powered flyby does not provide any significant benefit (if any at all) over the purely ballistic 2018 Mars free-return opportunity.

CHAPTER 7. CONCLUSION

The background required to set up and solve optimal control problems via optimal control theory is presented with a focus on applications to aero-assisted trajectories. The necessary conditions for local optimality with state-variable inequality constraints (SVIC) are outlined, and two methods for solving the associated boundary value problems are explained. The first method is Lobatto collocation, which uses *p*-th order polynomials in an implicit Runge-Kutta integration scheme to integrate a set of differential equations and satisfy the boundary conditions. In doing so, the differential equations are transcribed into a system of nonlinear equations to be solved simultaneously using a root-solving algorithm. The second method is a multiple shooting method which breaks up the sensitivity of explicit integration of N nodes and the initial conditions for each segment are found such that the flow is continuous, and the boundary conditions are satisfied.

Necessary conditions for local optimality for aerogravity assist trajectories are posed and solved with various cost functionals and constraints. The first cost functional is to maximize the velocity at atmospheric exit which minimizes the total energy lost due to drag. The boundary conditions are then adjusted so the vehicle departs the central body on a desired final V_∞^+ vector. This minimization of energy loss coupled with targeting the exit conditions produces the minimum required E^* to complete the AGA maneuver. An example trajectory at Mars is solved and the minimum E^* was 2.994.

The goal of the second AGA optimal control problem is the same as the first, but now a stagnation-point convective heating-rate constraint is imposed on the trajectory via a SVIC. The process calculates the minimum E^* required to complete the AGA maneuver with the convective heating-rate below a certain prescribed maximum value. An example trajectory is computed at Venus, with a minimum E^* of 3.06 when no heat constraint is enforced, but increases to 5.23 in the presence of the constraint.

The last optimal control problem minimized the total integrated heat load the vehicle accrues during the flythrough while simultaneously targeting the outbound V_∞^+ vector directly in the boundary conditions. Numerical difficulties prevented the direct targeting of the V_∞^+ vector in the first two methods, but was overcome by the time the last optimal control problem was formulated and solved. This last method allows for more flexibility in choosing vehicle parameters, as E^* can now be chosen to see if it can satisfy the mission requirements. An example trajectory at Mars is solved with an E^* of 3.5 and nose radius of 1 m, giving a heat load of 29.4 kJ/cm^2 with associated maximum heat-rate of 95.9 W/cm^2. It is shown that current thermal protection system (TPS) materials are capable of handling these heating characteristics with only 18.3% of the vehicle mass required to be dedicated to the TPS.

Optimal aerocapture trajectories at the Ice Giants including rotational atmospheric effects are formulated and solved with optimal control theory to minimize the total heat load. Using bank angle as the sole control mechanism, it was found that a sub-optimal control of using purely lift-up (bank of zero) while targeting a desired capture orbit gives roughly the same result in terms of total heat load. The reason for the similarity in the results is due to the high speeds of approach and the limited control authority present during the trajectory. The lift influences the motion of the trajectory in the limited time the vehicle is deepest in the atmosphere, where the density is highest. At these lower altitudes, the optimal result is to point the lift vector to be nearly lift-up, mitigating the higher heating that comes from flying at lower altitudes.

A study was conducted to find all the desirable candidate trajectories this century for a Mars free-return mission that are possible using current technology. It was discovered that the one proposed for Inspiration Mars in early 2018 is the best chance we have in this century. Since the next opportunity does not occur for another 15 years in 2032, it emphasizes the urgency for a human mission to Mars in 2018. The time-free ephemeris (TFE) shows the relative geometries that Earth and Mars need to possess for an Inspiration Mars-like mission to occur, and similar geometries only occur every 15 or 17 years – a considerable waiting period. Unless a back-up trajectory is found using other gravity-assist sequences, or new propulsive technology is developed to open up other trajectory design spaces, it would mean another long waiting period until another human mission to Mars could be flown.

CHAPTER 8. FUTURE WORK

8.1 Optimal AGA Trajectories

An additional idea for AGA trajectory optimization is including a heliocentric plane-change during the AGA to minimize the potential cost for a required deep-space maneuver to get into a target heliocentric inclination. For example, to get to Ceres with an inclination of 16°, an AGA could be performed at Mars to get the required V_∞^+ vector that includes the large plane-change maneuver.

8.2 AGA Guidance

There is much room for improvement to the presented AGA guidance algorithm. Thus far there has only been one conference paper on AGA guidance subject to dispersions [32], and only the bank angle was used as the control mechanism. The aerodynamic and IMU uncertainties were not included in the analysis in chapter 4, and the effects these dispersions have on the clean-up maneuver need to be investigated. Chapter 4 indirectly uses angle-of-attack as the control, however there may be benefits to using a combination of both angle-of-attack and bank angle. Since the lift and drag coefficients are directly affected by angle-of-attack there are uncertainties associated with them that may be avoided by using bank angle.

The predictor-corrector has a problem with convergence if the AGA vehicle loses too much energy during the entry phase. For example, if during the entry phase, the vehicle overshoots the reference radius as depicted in Figure 4.5, it is that there is not enough energy to reach the desired exit conditions. If this is the case, the built-in targeting algorithm will fail to converge and the algorithm breaks down. A possible solution to resolve the failed overshoot cases is to employ optimization techniques that attempt to minimize both the magnitude and direction of the V_∞^+ vector upon atmospheric exit. The best way to set up the optimization method is with nonlinear programming (NLP) software using a multi-objective optimization method, since both direction and magnitude are under consideration. Including these cases would increase the radius of convergence of the predictor-corrector.

Another issue that could be addressed for AGA guidance during the cruise phase could be to have the vehicle track an updated radius reference profile that has a constant nonzero, negative flight-path angle. It has been shown in Lohar et al. [27] that flying at such an angle for a majority of the AGA maneuver restricts the maximum heat-rate.

8.3 STOUR-AGA

While using STOUR-AGA for finding possible tours employing AGA, it was noticed that perhaps not all of the solutions using the E^* matching algorithm were being logged. The potential problem was noticed when running STOUR-AGA with a small difference in user-defined E^* of 0.05 – the results were drastically different. Since the algorithm finding the solutions uses a root-solving technique and the equations solved are nonlinear there could be possible solutions that are not being logged. An investigation into the algorithm using the root-solver could be performed to see if all of the possible solutions are being found.

REFERENCES

REFERENCES

[1] Topputo, F and Zhang, C., “Survey of Direct Transcription for Low-Thrust Space Trajectory Optimization with Applications,” *Abstract and Applied Analysis*, Vol. 2014, Article ID 851720.

[2] Conway, B. A., “A survey of methods available for the numerical optimization of continuous dynamic systems,” *Journal of Optimization Theory and Applications*, 152(2):271–306, 2012.

[3] Bryson, A. E. Jr. and Ho, Y. C., *Applied Optimal Control*, Hemisphere Publishing, Washington, D.C., 1975.

[4] Citron, S. J., *Elements of Optimal Control*, Holt, Rinehart, and Winston, New York, 1969.

[5] Longuski, J. M., Guzmán, J. J., and Prussing, J. E., *Optimal Control with Aerospace Applications*, Springer, New York, 2014.

[6] Pesch, H. J., “A Practical Guide to the Solution of Real-Life Optimal Control Problems,” *Mathematisches Institut, Technische Universität München*, 1994.

[7] Jacobsen, D. H., Lele, M. M., and Speyer, J. L., “New Necessary Conditions of Optimality for Control Problems with State Variable Inequality Constraints,” *Journal of Mathematical Analysis and Application*, Vol. 35, pp. 255–284.

[8] Penrose, R., “On best approximate solution of linear matrix equations,” *Proceedings of the Cambridge Philosophical Society*, Vol. 52, pp. 17–19.

[9] Jay, L. O., “Lobatto Methods,” Department of Mathematics, The University of Iowa, Iowa City, IA.

[10] Grebow, D. J. and Pavlak, T. A., “Ammos report on collocation methods,” Technical report, *Jet Propulsion Laboratory*, *California Institute of Technology*, Pasadena, California, 2015.

[11] Kierzenka, J. and Shampine, L. F., “A BVP Solver Based on Residual Control and the MATLAB PSE,” *ACM Transactions on Mathematical Software*, Vol. 27, No. 3, September, 2001, pp. 299–316.

[12] de Boor, C. W., "Good Approximate by Splines with Variable Knots II," *Conference on the Numerical Solution of Differential Equaitons*, Vol. 363, 1973, pp. 12–20.

[13] Mease, K.D., and Vinh, N.X., "Minimum-Fuel Aeroassisted Coplanar Orbit Transfer Using Lift- Modulation," Journal of Guidance, Control, and Dynamics, Vol. 8, No. 1, Jan.-Feb. 1985.

[14] Longuski, J.M., "Can Aerogravity-Assist Through the Venusian Atmosphere Permit a Near Radial Trajectory into the Sun?," Jet Propulsion Laboratory, EM 312/82-133, California Institute of Technology, Pasadena, CA, Dec. 1982.

[15] Vinh, N.X., Busemann, A., and Culp, R.D., Hypersonic and Planetary Entry Flight Mechanics, The University of Michigan Press, Ann Arbor, MI, 1980.

[16] Walberg, G.D., "A Survey of Aeroassisted Orbit Transfers," *Journal of Spacecraft and Rockets*, Vol. 22, No.1, Jan.-Feb. 1985.

[17] Anderson, J.D., Ferguson, F., and Lewis, M.J., "Hypersonic Waveriders for High Altitude Applications," AIAA 91-0530 paper, Jan. 1991.

[18] Anderson, J.D., Lewis, M.J., Kothari, A.P., and Corda, S., "Hypersonic Waveriders for Planetary Atmospheres," *Journal of Spacecraft and Rockets*, Vol. 28, No. 4, July-Aug. 1991.

[19] Lewis, M.J., and McRonald, A.D., "Design of Hypersonic Waveriders for Aeroassisted Interplanetary Trajectories," *Journal of Spacecraft and Rockets*, Vol. 29, No. 5, Sept.-Oct. 1992.

[20] Randolph, J.E., and McRonald, A.D., "Solar System 'Fast Mission' Trajectories Using Aerogravity Assist", *Journal of Spacecraft and Rockets*, Vol. 29, No. 2, March-April 1992.

[21] Bonfiglio, E.P., Longuski, J.M., and Vinh, N.X., "Automated Design of Gravity-Assist and Aerogravity-Assist Trajectories," *Journal of Spacecraft and Rockets*, Vol. 37, No. 6, Nov.-Dec. 2000.

[22] Sims, J. A., "Delta-V Gravity-Assist Trajectory Design: Theory and Practice," Ph.D. Thesis, School of Aeronautics and Astronautics, Purdue University, West Lafayette, IN, 1996.

[23] Sims, J.A., Longuski, J.M., and Patel, M.R., "Aerogravity-Assist Trajectories to the Outer Planets and the Effect of Drag," *Journal of Spacecraft and Rockets*, Vol. 37, No. 1, Jan-Feb 2000.

[24] Johnson, W.R., and Longuski, J.M., "Design of Aerogravity-Assist Trajectories," *Journal of Spacecraft and Rockets*, Vol. 39, No. 1, Jan-Feb 2002.

[25] Johnson, W.R., "Analysis and Design of Aeroassissted Interplanetary Missions," Ph.D. Thesis, School of Aeronautics and Astronautics, Purdue University, West Lafayette, IN, 2002.

[26] Vinh, N.X., *Optimal Trajectories in Atmospheric Flight*, Elsevier Scientific Publishing, New York, 1981.

[27] Lohar, F., Mateescu, D., and Misra, A., "Optimal Atmospheric Trajectory for Aerogravity Assist," *Acta Astronautica*, Vol. 32, No. 2, Feb. 1994.

[28] Trask, A.J., and Coverstone, V.L., "Optimal Low-Thrust Trajectories Combined with and Aeroassist Maneuver," *Journal of Spacecraft and Rockets*, Vol. 41, No. 4, Jul.-Aug. 2004.

[29] Lohar, F., Misra, A., and Mateescu, D., "Optimal Atmospheric Trajectory for Aerogravity Assist with Heat Constraint," *Journal of Guidance, Control, and Dynamics*, Vol. 18, No. 4, Jul.-Aug. 1995.

[30] Lyons, D. T., Sklyanskiy, E., Casoliva,J., and Wolf, A. A., "Parametric Optimization and Guidance for an Aerogravity Assisted Atmospheric Sample Return from Mars and Venus", AIAA Paper 08-7353, AIAA/AAS Astrodynamics Conference, Honolulu, Hawaii, Aug. 18-21, 2008.

[31] Henning, G. A., Edelman, P. J., and Longuski, J. M., "Design and Optimization of Interplanetary Aerogravity-Assist Tours," *Journal of Spacecraft and Rockets*, Vol. 51, No. 6, November, 2014.

[32] Casoliva, J., Lyons, D. T., Wolf, A. A., and Mease, K. D., "Robust Guidance via a Predictor-Corrector Algorithm with Drag Tracking for Aero-Gravity Assist Maneuvers," *AIAA/AAS Astrodynamics Specialist Conference*, AIAA Paper 2008-7353, Honolulu, Hawaii, Aug. 2008.

[33] McRonald, A.D., and Randolph, J.E., "Hypersonic Maneuvering for Augmenting Planetary Gravity Assist," Journal of Spacecraft and Rockets, Vol. 29, No. 2, March-April 1992.

[34] Rinderle, E. A., "Galileo User's Guide, Mission Design System, Satellite Tour Analysis and Design Subsystem," Jet Propulsion Lab., Rept. JPL D-263, California Inst. of Technology, Pasadena, CA, July 1986.

[35] Williams, Steven, "Automated Design of Multiple Encounter Gravity-Assist Trajectories," MS Thesis, School of Aeronautics and Astronautics, Purdue University, West Lafayette, IN, August 1990.

[36] Nonweiler, T.R.F., "Aerodynamic Problems of Manned Space Vehicles," *Journal of the Royal Aeronautics Society*, Vol. 63, Sept. 1959, pp. 521-528.

[37] Smith, T., and Longuski, J.M., "Optimal Atmospheric Trajectories for Aerogravity Assist Interplanetary Missions," School of Aeronautics and Astronautics, Purdue University, West Lafayette, IN, Apr. 2006.

[38] Anderson, J. D., *Hypersonic and High Temperature Gas Dynamics*, McGraw-Hill, New York, 1989.

[39] Sutton, K., and Graves, R. A., Jr., "A General Stagnation Point Convective Heating Equation for Arbitrary Gas Mixtures," NASA TR-R376, Nov. 1971.

[40] Tauber, M., and Sutton, K., "Stagnation-Point Radiative Heating Relations for Earth and Mars Entries," *Journal of Spacecraft and Rockets*, Vol. 28, No. 1, 1991, pp. 40–42.

[41] Brandis, A. M., and Johnston, C. O., "Characterization of Stagnation-Point Heat Flux for Earth Entry," *45th AIAA Plasmadynamics and Lasers Conference*, Atlanta, GA, June, 2014.

[42] Hughes, K. M., Edelman, P. J., Saikia, S. J., Longuski, J. M., Loucks, M. E., Carrico, J. P., and Tito, D. A., "Fast Free Returns to Mars and Venus with Applications to Inspiration Mars," *Journal of Spacecraft and Rockets*, Vol. 52, No. 6, 2015, pp. 1712–1735.

[43] Kolawa, E., Balint, T. S., Birur, G., Brandon, E., Del Castillo, L., Hall, J., Johnson, M., Kirschman, R., Manvi, R., Mojarradi, M., Moussessian, A., Patel, J., Pauken, M., Peterson, C., Whitacre, J., Martinez, E., Venkatapathy, E., Newdeck, P., and Okojie, R., "Extreme Environment Technologies for Future Space Science Missions," NASA Technical Report, JPL D-32832, Pasadena, CA, Sept. 19, 2007.

[44] Mazzaracchio, A., "Flight-Path Angle Guidance for Aerogravity-Assist Maneuvers on Hyperbolic Trajectories," *Journal of Guidance, Control, and Dynamics*, Vol. 38, No. 2, February, 2015.

[45] Green, J., *Planetary Science Division Status Report*, Presentation at OPAG, http://www.lpi.usra.edu/icegiants/mission_study/IceGiantCall.pdf [retrieved 10 August 2016].

[46] Hollister, W. M., "Mars Transfer via Venus," AIAA/ION Astrodynamics Guidance and Control Conference, Los Angeles, CA, Aug. 24–26, 1964, AIAA 64-647.

[47] Sohn, R.L., "Manned Mars Trips Using Venus Flyby Modes," *Journal of Spacecraft and Rockets*, Vol. 3, No. 2, 1966, pp.161 – 169.

[48] Wilson, S., "Fast Round Trip Mars Trajectories," AIAA/AAS Astrodynamics Conference, Portland, OR, Aug. 20 – 22, 1990, AIAA 90-2934.

[49] Wolf, A. A., "Free Return Trajectories for Mars Missions," AAS/AIAA Annual Spaceight Mechanics Meeting, Houston, TX, Feb. 11 – 13, 1991.

[50] Walberg, G., "How Shall We Go to Mars? A Review of Mission Scenarios," *Journal of Spacecraft and Rockets*, Vol. 30, No. 3, March – April 1993.

[51] Hoffman, S.J. and Kaplan, D.I. (eds.), "Human Exploration of Mars: The Reference Mission of the NASA Mars Exploration Study Team," NASA SP 6107, March 1997.

[52] Drake, B.G. (ed.), "Reference Mission Version 3.0 Addendum to the Human Exploration of Mars: The Reference Mission of the NASA Mars Exploration Study Team," NASA Rept. EX-98-036, June 1998.

[53] Casalino, L., Colasurdo, G., and Patrone, D., "Mission Opportunities for Human Exploration of Mars," *Planetary and Space Science*, Vol. 46, No. 11/12, pp. 1613 – 1622, 1998.

[54] Lyne, J. E., and Townsend, L. W., "Critical Need for a Swingby Return Option for Early Manned Mars Missions," *Journal of Spacecraft and Rockets*, Vol. 35, No. 6, 1998, pp. 855, 856.

[55] Patel M.R., Longuski, J.M., and Sims, J.A., "Mars Free Return Trajectories," *Journal of Spacecraft and Rockets*, Vol. 35, No. 3, May – June 1998.

[56] Okutsu, M. and Longuski, J.M., "Mars Free Returns via Gravity Assist from Venus," *Journal of Spacecraft and Rockets*, Vol. 39, No. 1, Jan. – Feb. 2002.

[57] Foster, C. and Daniels, M., "Mission Opportunities for Human Exploration of Nearby Planetary Bodies," AIAA SPACE Conference and Exposition, Anaheim, CA, Aug. – Sep. 2010.

[58] Tito, D.A., Anderson, G., Carrico, J.P., Clark, J., Finger, B., Lantz, G.A., Loucks, M.E., MacCallum, T., Poynter, J., Squire, T.H., and Worden, S.P., "Feasibility Analysis for a Manned Mars Free-Return Mission in 2018," *IEEE* Aerospace Conference, Big Sky, MT, March 2013.

[59] Bailey, L., Folta, D., Barbee, B., Vaughn, F., Kirchman, F., Englander, J., Campbell, B., Thronson, H., and Lin, T.Y., “A Lean, Fast Mars Round-Trip Mission Architecture: Using Current Technologies for a Human Mission in the 2030s” AIAA SPACE Conference and Exposition, San Diego, CA, Sep. 10 – AIAA 2013-5507.

[60] Folta, D., Barbee, B. W., Englander, J., Vaughn, F., and Lin, T.Y., “Optim Trip Trajectories for Short Duration Mars Missions,” AAS/AIAA Astrodynamics Specialist Conference, Hilton Head, SC, Aug. 11 –15, 2013, AAS 13-808.

[61] Patel, M.R., “Automated Design of Delta-V Gravity-Assist Trajectories for Solar System Exploration,” M.S. Thesis, School of Aeronautics and Astronautics, Purdue University, West Lafayette, IN, Aug. 1990.

APPENDIX

APPENDIX

QUESTIONS, NOTES, AND FEEDBACK DURING DEFENSE

1. *Why minimize the heat-load for AGA compared to other cost functionals?*

One of the main technology requirements to make AGA realizable is to have a TPS material able to withstand the heating rates and heat loads associated with the atmospheric flythrough. One way to address the heating issue is to fly the trajectory which minimizes the heat load in an attempt to make it feasible for current or near-future TPS technologies. Formulating the problem to minimize the heat load also allows for a straightforward implementation in classical optimal control theory.

2. *Could the radiative heat rate be curve-fit and added to the cost functional?*

The radiative heating can be curve fit to the tabulated data in the equation, and added to the cost functional. Since the tabulated data is only a function of velocity, it should be straightforward to apply the necessary conditions for local optimality.

3. *Has a sensitivity analysis or analysis of variance been performed for AGA?*

A sensitivity analysis has not been done, but it is important to see what varying the arrival conditions to the flyby planet does to the optimal path. There is an admissible set of initial conditions that will allow for convergence of the optimal trajectory, but seeing how sensitive the edges of this admissible set is an interesting issue that should be investigated in future work.

4. *What are the most important factors for heating?*

According to the models used for convective and radiative heating, they are functions of nose radius, atmospheric density, and velocity. Flying higher may lead to reduced heating as the atmospheric density is lower, however the vehicle may not dissipate enough energy to depart on the desired V_∞ vector. Arriving to the flyby body slower would also lower the heating, but this could prevent a substantial amount of turning around the planet, meaning the benefits of using AGA would not be as apparent compared with a traditional propulsive burn.

5. *How does the spacecraft know where it is located?*

An issue that hasn't been addressed in the AGA problem is navigation. There will have to be an autonomous observer to get estimates of the states, as there will likely be no measurements that could be made from Earth. Navigation is a problem that will need to be investigated in future work to make the AGA concept more achievable.

6. *Where did the uniform distribution for the initial conditions come from?*

The uniform distribution for the initial conditions was used to simulate random dispersions in the initial conditions without known statistics on the mean or variance. The ranges used in the uniform distribution are the current ranges that the predictor-corrector can handle and still converge. One way to possibly widen the range of acceptable values is to reformulate the predictor-corrector as a multi-objective direct optimal control problem to minimize the error (taking into account both direction and magnitude) between the actual and desired V_∞ vectors.

7. *Where did bounds on $\alpha, \dot{\alpha}, \ddot{\alpha}$ come from?*

The bounds on the angle-of-attack and its rates were taken from Casoliva et al. [32], that used these same rates for their bank angle guidance formulation. The rates were claimed to be similar to that of the space shuttle. Since the angle-of-attack is changed in a different manner than the bank angle, future work should investigate whether the bounds on angle-of-attack used are realistic.

8. Are control surfaces used to change the angle-of-attack?

The angle-of-attack, and thus the lift coefficient, is adjusted by control surfaces on the vehicle. The bounds for the angle-of-attack for the waverider in the present work are bounded between $-10 \leq \alpha \leq 25$ and for all trajectories presented the vehicle stays within the bounds. However investigations into whether or not control surfaces can achieve these values without a significant drag penalty is required in future work.

9. What is the inclination for the Uranus aerocapture maneuver?

The inclination has a value of 74.4 degrees.

10. Do you want to maximize L/D, or Drag during aerocapture?

Since the goal of aerocapture is to deplete the orbital energy to a desired capture orbit, the drag should be considered the parameter of interest. Flying at maximum *L*/*D* the whole maneuver may not necessarily give the best results. An study should be conducted to see if the *L*/*D* should vary to give higher or lower values of drag, giving a better minimum for the total heat load. Adding the *L*/*D* as an additional control and solving the optimization problem would be one way to investigate this issue.

11. Is heating maximum at the stagnation point?

The heating is not necessarily a maximum at the stagnation point. If there are points where turbulent flow can impact the vehicle, especially when there are long running lengths in any direction, the peak heating can increase. A rule-of-thumb to approximate this value is multiplying the peak heating rate at the stagnation point by three.

12. *For the guidance, what if atmospheric density fluctuates heavily over terrestrial surface?*

If the atmospheric density varies with latitude and longitude, there would need to be something in the guidance algorithm to address this. One way would be to re-compute the reference density at every guidance cycle. However the problem with this approach is that too much or not enough energy may be dissipated to reach the exit conditions. If the vehicle can't reach the exit conditions (according to the predictor-corrector), then the predictor-corrector would need to be modified to minimize the error in the exit conditions using a direct optimization scheme, as described in the future work section.

VITA

VITA

Peter Joseph Edelman was born February 6, 1988, in Agoura Hills, California. His mother, Andrea Perejda, has a PhD in cell biology. His father, Alan Edelman M.D., is a neurological surgeon. Peter was raised in Arroyo Grande, California, on the Central Coast. He has played piano since the age of four, was a winner in a state-wide youth piano competition, and has participated in two Piano Performance Master Classes with Dr. Terrance Spiller and Dr. Kirill Gliadkovsky in 2005 and 2006 respectively. In his teen years, Peter took up the sport of surfing and taught himself guitar, and was on the tennis team in high school.

Peter graduated from Arroyo Grande High School in June, 2006. He took all the advanced mathematics classes offered at his high school. He was inspired to pursue aeronautical engineering by Dr. Ed Avila who offered an introductory class to topics in various engineering fields. Peter also participated in youth activities at the NASA facility in Huntsville, Alabama and locally at Vandenberg Air Force Base.

Peter received a Bachelor’s of Science in Aeronautical and Astronautical Engineering from Purdue University in May of 2010, and a Master’s of Science in Aeronautics and Astronautics from Purdue University in December of 2011. He has worked as a Teaching Assistant at Purdue, as well as tutoring students individually in engineering mathematics and physics courses. The courses he was a teaching assistant for include sophomore and senior spacecraft design courses, advanced dynamics, and trajectory optimization. Peter has worked with Dr. Buzz Aldrin and Purdue's undergraduate senior design class to conduct feasibility studies for Buzz's "Pathways to Mars," under his "Unified Space Vision," in both 2014 and 2015.

Peter's research interests include space mission design (both high-level feasibility studies as well as high-fidelity design), and interplanetary/atmospheric trajectory optimization. He is a member of the American Honor Society in Aerospace Engineering (Sigma Gamma Tau) and was the vice president of Purdue's chapter for the 2009-2010 academic years.

PUBLICATIONS

PUBLICATIONS

Peer-Reviewed Journal Articles

1. Henning, G. A., Edelman, P. J., and Longuski, J. M., “Design and Optimization of Interplanetary Aerogravity-Assist Tours,” *Journal of Spacecraft and Rockets*, Vol. 51, No. 6, November, 2014.

2. Hughes, K. M., Edelman, P. J., Saikia, S. J., Longuski, J. M., Loucks, M. E., Carrico, J. P., and Tito, D. A., “Fast Free Returns to Mars and Venus with Applications to Inspiration Mars,” *Journal of Spacecraft and Rockets*, Vol. 52, No. 6, 2015, pp. 1712–1735.

3. Edelman, P. J. and Longuski, J. M., “Optimal Aerogravity-Assist Trajectories Minimizing Total Heat Load,” Submitted to: *Journal of Guidance, Dynamics, and Control*, September, 2016.

Conference Papers

1. Edelman, P.J., Hughes, K.M., Longuski, J.M., Carrico, J.P., Loucks, M.E., and Tito, D.A., “Inspiration Mars 2018 Free-Return Opportunity,” AIAA/AAS Astrodynamics Specialist Conference, San Diego, CA, August 4–7, 2014, AIAA 2014-4128.

2. Hughes, K.M., Edelman, P.J., Longuski, J.M., Loucks, M.E., Carrico, J.P., and Tito, D.A., “Fast Mars Free-Returns via Venus Gravity Assist,” AIAA/AAS Astrodynamics Specialist Conference, San Diego, CA, August 4–7, 2014, AIAA 2014-4109.

Poster Session

1. Edelman, P. J., Shibata, E., Saikia, S. J., and Longuski, J. M., “Rapid Exploration of the Solar System Using Aerogravity-Assist,” *Thirteenth Annual International Planetary Probe Workshop*, Johns Hopkins Applied Physics Laboratory, Laurel, MD, July, 2016.